Forced Response of a Centrifugal Compressor Stage Due to the Impeller-Diffuser Interaction

by

Edward James Walton

B.S., Boston University (2008)

Submitted to the Department of Aeronautics and Astronautics
in partial fulfillment of the requirements for the degree of

Master of Science

at the

MASSACHUSETTS INSTITUTE OF TECHNOLOGY

February 2014

Author .....
Department of Aeronautics and Astronautics
January 30, 2014

Certified by.....
Choon S. Tan
Senior Research Engineer, Gas Turbine Laboratory
Thesis Supervisor

Accepted by.....
Paulo C. Lozano
Associate Professor of Aeronautics and Astronautics
Chair, Graduate Program Committee

Forced Response of a Centrifugal Compressor Stage Due to the Impeller-Diffuser Interaction

by

Edward James Walton

Submitted to the Department of Aeronautics and Astronautics
on January 30, 2014, in partial fulfillment of the
requirements for the degree of
Master of Science

Abstract

The unsteady pressure field experienced by a centrifugal compressor stage can be dominated by of the impeller-diffuser interaction. The energy of the unsteady field, under certain aerodynamic and structural conditions, is capable of forcing the rotating impeller blades to vibrate excessively to the point of failure, better known as a high cycle fatigue (HCF) failure. This thesis seeks to identify the physical mechanisms that set the forced response amplitude of an impeller due to the impeller-diffuser interaction. The centrifugal stage researched is comprised of a stationary discrete passage diffuser and an unshrouded rotating impeller with both main and splitter blades. The forced response of two splitter blade modes are computed for a variety of structural boundary conditions and unsteady loadings to elicit the driving physical mechanisms. The findings indicate that the forced response is enhanced when the excitation frequency matches a component's natural frequency, the characteristic wavelength of the unsteady loading matches that of the structural vibration mode, the resonance occurs at high speed, and when modal displacement exists at the impeller blade's trailing edge. The findings also suggest that modal coupling of blade and disk dominant modes leads to high sensitivity of the forced response to small variations in airfoil and disk backwall thickness. Identification of blade-disk couplings are described using a simplified SAFE (Singh's Advanced Frequency Evaluation) diagram. The forced response of taut strings, Bernoulli-Euler beams, and a two mass-spring system are also utilized to elicit how the physical mechanisms act on the impeller's forced response. The Bernoulli-Euler beam model suggests that a mismatch of the forcing wavelength to the structural wavelength by 50% will reduce the forced response amplitude by at least 75%. Finally, a decision tree is proposed to assess the relative resonant risk of impeller modes to the diffuser excitation by identifying which of the physical mechanisms may be the dominant driver of the forced response.

Thesis Supervisor: Choon S. Tan
Title: Senior Research Engineer, Gas Turbine Laboratory

Acknowledgments

This research has been performed in conjunction with the GUIde 4 consortium of government, university, and industry partners in the field of turbomachinery aeromechanics. Funding was provided by the consortium under award number 10-AFRL-1022 and through the Air Force Research Lab under Prime Contract FA8650-08-D2806. Guidance from the consortium's partners has been invaluable over the past two years.

I would like to thank my adviser, Professor Choon S. Tan of MIT's Gas Turbine Lab, for his patience, understanding, and guidance over the past two years. It was through his style of mentoring my research that I was able to develop a strong understanding of the topic. Dr. Tan kept me focused on the larger goal as I developed new hypotheses, tested my ideas, and deliberated the results.

Additional appreciation goes to current and former MIT Gas Turbine Lab students, namely Chris Lusardi and Caitlin Smythe, for sharing their knowledge and experience in this field. Special thanks is extended to fellow MIT student and good friend James Schulmeister for his loyal help and insight.

I'd like to thank the management of my employer for allowing me to pursue my master's degree part-time. I would like to thank Mark Pearson, Tom Martyn, and Dan Barber for their patience and flexibility as I pursued this degree. Also, I would like to thank the technical guidance I received over the past few years, namely from Bob Kursmark, Bruce Dickman, Ken Gould, Jeff Nussbaum, Meredith Wulff, Sergio Filippi, Ray MacKay, Bob Walter, Mike Macrorie, Rajiv Sampath, and Kishore Ramakrishnan.

And finally, special thanks goes out to my parents, Linus and Kathy; my siblings, Zandra, Linus Jr., Beatrice, and Caroline; my girlfriend Jill; and all my friends who kept me motivated and made it fun every day.

Contents

List of Figures

List of Tables

Nomenclature

Subscripts

1	Inducer conditions or fundamental mode number
corr	Corrected conditions
d	Diffuser
max	Maximum
min	Minimum
n	Mode number index
phy	Physical (operating) conditions
PS	Pressure side
SS	Suction side
t	Total properties

Symbols

a_o	Local speed of sound
A	Cross sectional area
C or c	General constant
$\mathbf{C}$	Damping matrix
C_f	Phase speed of forcing
C_p	Phase speed of vibration
C_r	Rod-wave velocity
d	Harmonic index
E	Young's modulus
$\vec{F}$	Force vector
F_{modal}	Modal force
h	Backwall thickness
I	Moment of inertia

$IBPA_d$	Inter blade phase angle of diffuser excitation
k	Wavenumber of structure
k_n	Natural wavenumber of structure
K	Wavenumber of forcing function
$\mathbf{K}$	Stiffness matrix
L	Length
$\dot{m}$	Mass flow rate
M	Number of elements in FEM model
$\mathbf{M}$	Mass matrix
M_{rel}	Relative Mach number
n	Number of nodes in FEM model
$\vec{n}$	Surface normal vector
N	Number of modeled sectors in full wheel
N_d	Number of diffuser passages
P	Static pressure
P_f	Static pressure fluctuation
P_r	Unsteady pressure resolved into magnitude and phase at frequency of interest
q	Exducer dynamic head pressure
Q	Quality factor of damping
r	Ratio of forcing frequency to fundamental structural frequency
R	Exducer radius
t	Blade tip thickness
T	Tension
U	Tip speed
w	Deflection

Greek

α	Sector wedge angle
β_n	Boundary condition specific constant for BE beams

δ	Ratio of total pressure to STP pressure
Δ	Change in a quantity
ΔL	Loading fluctuation
ΔP_s	Blade loading normalized by exducer dynamic head
ζ	Damping ratio
Θ	Ratio of total temperature to STP temperature
κ	Ratio of forcing wavenumber to fundamental structural wavenumber
λ	Wavelength
Λ	Eigenvalue
ν	Poisson's ratio
ρ	Mass density
τ	Characteristic time period
ϕ	Mode shape
ϕ_h	Homogeneous solution
ϕ_p	Particular solution
Φ	Mode shape phase angle
ω	Frequency of structure
Ω	Frequency of forcing function
Ω_o	Rotational speed

Abbreviations

3D	Three Dimensional
BC	Boundary Condition
BE	Bernoulli-Euler
BT	Backward Traveling
CFD	Computational Fluid Dynamics
corr.	Corrected conditions
DOF	Degrees of Freedom
EO	Engine Order

FEM	Finite Element Method
FFT	Fast Fourier Transform
FT	Forward Traveling
HCF	High Cycle Fatigue
IBPA	Inter Blade Phase Angle
LCF	Low Cycle Fatigue
LE	Leading Edge
ND	Nodal Diameter
PS	Pressure Side
SAFE	Singh's Advanced Frequency Evaluation
SDOF	Single Degree of Freedom
SS	Suction Side
SST	Shear Stress Transport
STP	Standard Temperature and Pressure
TE	Trailing Edge

Expressions

chord	Splitter chord normalized to a length of 1
crossing	Point on a Campbell diagram where an excitation and a natural frequency intersect
midspan	50% airfoil span
$/rev$	per revolution
tip	95% airfoil span
veering	Point on a simplified SAFE diagram where airfoil and disk modes intersect

Chapter 1

Introduction

1.1 Motivation

Centrifugal compressor stages are used in a variety of turbomachinery applications including power generation, rocket engine turbopumps, oil and natural gas pumps, CO_2 sequestration pumps, and aircraft engines. Centrifugal compressor stages add energy to the working fluid by raising the stagnation enthalpy. In an aircraft engine centrifugal compressor stages may be used alone, in series, or in combination with a supercharging axial compressor stage. A single centrifugal compressor stage is comprised of a rotating impeller and downstream stationary diffuser. Like all turbomachinery, centrifugal compressor stages are susceptible to vibratory excitation which can cause excessive stress and potential failure.

Current industry methods focus on minimizing the excitation strength by avoiding resonant conditions which may occur when the frequency of the forcing stimuli matches with natural frequencies of the structural components. Structures operating at resonance are at risk of failure due to high cycle fatigue (HCF) if the induced vibratory stress becomes excessive or prolonged. Avoiding all resonances in the operating range for an impeller is nearly impossible and might not be necessary as not all natural frequencies of the structural components may be excited by known excitations in the engine. Elucidating the conditions under which a centrifugal compressor stage may experience a strong resonant response is the subject of this thesis. Knowledge

of these conditions earlier in the design process will help to avoid costly redesign and repeated testing if aeromechanical issues are only discovered later.

This thesis seeks to identify the attributes of the unsteady loading and structural vibration modes that set the amplitude of the impeller's forced response. The physical mechanisms identified will help rank the relative risk of vibration modes in the operating range to a forced response induced by the impeller-diffuser interaction.

1.2 Technical Background

A centrifugal compressor stage generates a pressure rise by increasing the velocity of the working fluid as the flowpath turns away from centerline, increasing the flowpath radius. The diffusing section of the stage, or the "diffuser," slows the high speed flow exiting the impeller to generate a net increase in static pressure by reducing the Mach number and tangential component of the velocity. The discrete passage type diffuser is considered for this research but can take on many other forms (e.g. scroll, vane, pipe, etc.). The inlet of the diffuser and exit of the impeller are generally spaced closely in the radial direction for performance reasons. The impeller-diffuser gap is often referred to as the "vaneless" space and is among several features of a centrifugal stage known to affect the vibratory response of the impeller. The interaction between the impeller and diffuser has been referred to as the "impeller-diffuser interaction" and is responsible for generating an unsteady pressure field on the impeller blades.

1.2.1 Centrifugal Compressor Design

Centrifugal compressor stages have an impeller with an inlet called the inducer, an exit called the exducer, blades, a disk bore, and backwall. Figure 1-1 highlights these locations on a representative stage. Figure 1-2 shows a view of the research centrifugal stage. Note the discrete passages of the diffuser and the radial proximity of the diffuser vane leading edges to the impeller trailing edge.

The centrifugal compressor stage mechanical design is a compromise between various competing requirements. Competing requirements may include the low cycle

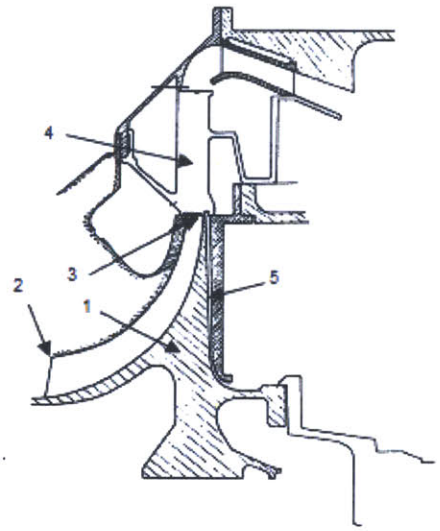

Figure 1-1: Schematic of a representative centrifugal compressor stage. 1 = impeller, 2 = inducer, 3 = exducer, 4 = diffuser, 5 = impeller backwall, adopted from [9].

Figure 1-2: View of the research centrifugal compressor stage showing the impeller and discrete passage diffuser, adopted from [9].

fatigue life (LCF) of the bore, creep life of high temperature and stress locations, crack growth, exducer tip deflection in both the axial and radial directions, HCF life of the blades and backwall, and many more. To "tune" the natural frequencies of the impeller, it may be necessary to add stiffness and mass to either the blades or backwall by making thickness changes. These changes do not come without penalty

as the added weight of thicker blades or a thicker backwall must be supported by the bore of the impeller disk, which is especially taxing if material must be added at the exducer radius. The added burden on the impeller disk may cause the fatigue life of the bore to be negatively affected. Knowing which modes in the operating range may have a high vibratory response before the design is tested would be of high value to a design engineer. With this knowledge during the design phase, necessary steps to tune at-risk modes to appropriate speeds could be coupled with the overall optimization of impeller mechanical design.

1.2.2 Flow Field Description

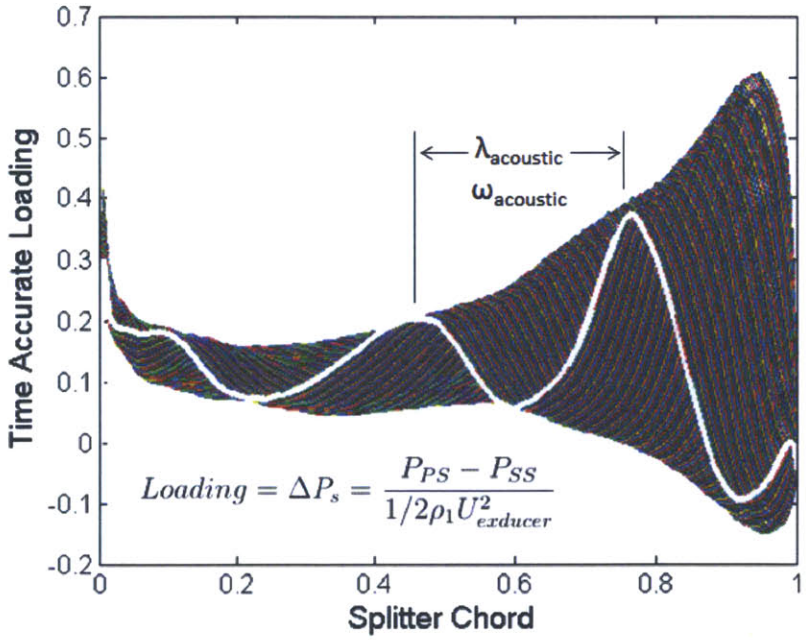

Figure 1-3: Time-accurate loading on the splitter blade tip normalized by the exducer dynamic head as result of an acoustic wave generated by the impeller-diffuser interaction propagating upstream. The leading edge is at a chord location of zero and and the trailing edge at one.

The forcing function is the result of the impeller-diffuser interaction. It has been shown by K. Gould [9], C. Lusardi [14], among others, to manifest itself as a traveling acoustic wave which propagates against the flow direction upstream along the impeller

blades, decaying as it does so. Figure 1-3 shows time-accurate traces of the splitter blade tip loading over two characteristic periods of the blade passing frequency. The loading has been normalized by the exducer dynamic head which is the dynamic pressure calculated using the inlet density and exducer tip speed. The last time point trace is shown as a solid white line. Note the envelope of the unsteadiness decreases toward the leading edge with the maximum loading occurring around 95% chord at a value of 0.6. The splitter chord, in all figures, is the normalized chord length with zero equal to the leading edge station and one equal to the trailing edge station.

The unsteady loading propagates as an acoustic wave for which the wavelength can be approximated as,

$$\lambda = \frac{a_o \left(1 - M_{rel}\right)}{\Omega_o N_d} \tag{1.1}$$

and can be shown to remain constant provided the corrected conditions remain consistent between operating points. a_o is the local speed of sound, M_{rel} is the relative Mach number, Ω_o is the rotational speed in Hertz and N_d is the integer count of the number of diffuser vanes or passages.

1.2.3 Aeromechanical Challenges with Impellers

Centrifugal compressor stages can suffer from a variety of aeromechanical vibration problems. Failure due to vibratory excitation is referred to as HCF. A component's fatigue capability is related to the material's fatigue strength and its stress state. Generally, the highly stressed impeller has the lower vibratory capability of the stage and failure may manifest itself as a crack in an impeller blade. The driving force of the vibratory response can be attributed to various time-varying loads acting on the impeller blades. The unsteady loading may be the result of an unsteady pressure field generated by the wakes from upstream stators, the interaction with the downstream diffuser, cavity resonances, or self-induced non-synchronous vibration such as flutter. Whether a response is synchronous or non-synchronous refers to whether the excitation frequency of the unsteady loading is "in sync" with the rotational speed; that is,

it varies with a fixed integer of the engine speed in revolutions per second sometimes referred to as the engine order (EO). If the natural frequency of a structural component and the forcing frequency match, the structure is said to be in resonance and the potential for the component to vibrate at high amplitude and stress exists.

To minimize the risk of HCF resonant failure in turbomachinery stages, industry has relied on either avoiding resonant crossings in the operating range or past experience. A resonant crossing refers to the engine speed at which an excitation stimuli matches a natural frequency of the structural components. Past experience risk assessment focuses on whether a particular excitation has been known to excite a particular family of structural modes. The former method of resonance avoidance seeks to avoid the resonance in the temporal domain by avoiding the conditions which match the forcing frequency with known natural frequencies of the structural components. The later method of resonance avoidance captures the effect of the spatial correlation between the forcing function and structural mode. Generally, the temporal matching is much easier to quantify than the spatial matching which relies on knowledge of the forcing function which might only be available using unsteady computational fluid dynamics (CFD) or measurements. In some instances, designing the resonant crossings out of the operating range may not be a feasible option and the design may proceed to testing with the expectation that the resonant response of the impeller will be measured. Often problematic resonant crossings are not found until the centrifugal stage is built and tested which may require significant resources to redesign. In these situations, having an understanding of the mechanisms that control the excitation of the impeller blades earlier in the design process may lead to designs which can better tolerate resonant crossings in the operating range.

1.2.4 Survey of Art: Assessing the Likelihood of Aeromechanical Difficulties

Methods traditionally employed in aeromechanical design of rotating impellers, include the use of Campbell diagrams, frequency versus nodal diameter plots (some-

times referred to as Singh's Advanced Frequency Evaluation, or SAFE, diagrams), and Goodman diagrams. These diagrams highlight the current methods to identify and correct potential HCF issues during the design process. The limitations of current methods is in the prediction of the actual response, in terms of physical displacement or stress versus the material's capability. Unless measurements have been made with strain gauges or lightprobes, the aforementioned diagrams only help to highlight engines speeds at which potential HCF issues may manifest themselves and not the actual response expected.

The Campbell diagram shows frequency versus engine speed. The natural frequencies of structural modes and known engine order excitation frequencies are shown across the operating range. The intersection of these curves represents a potential resonance where the natural structural frequency and forcing frequency match. The excitation order of upstream and downstream stages are generally shown as these may be the dominant sources of unsteady loading on the airfoil. Figure 1-4 shows the Campbell diagram for two splitter blade natural frequencies and the speed at which these modes may experience resonance with the diffuser engine order excitation.

The SAFE diagram shows frequency versus nodal diameter and was originally developed by Murari Singh [6]. Similar to the Campbell diagram, natural frequencies of the structural modes are shown but now against possible nodal diameters of the full wheel. This plot highlights how the excitation acting circumferentially around the rotor spatially correlates with the nodal diameter of vibration. If the frequency of excitation and the structural mode are matched, in addition to matching the engine order excitation and nodal diameter of the mode shape, a potentially strong resonance may occur since vibratory energy acting on each airfoil of the rotor will be in phase with the vibration of the structure. This diagram also helps identify nodal diameters at which mode shape families, such as those with blade or backwall dominant motion, intersect. The crossings on the SAFE diagram are referred to as "veering" points. Modes close to veering points may exhibit modal displacements which are a combination of the two families of modes but at a different frequency [19]. Figure 1-5 shows a simplified SAFE diagram for the research impeller. Liberty is taken to connect modes

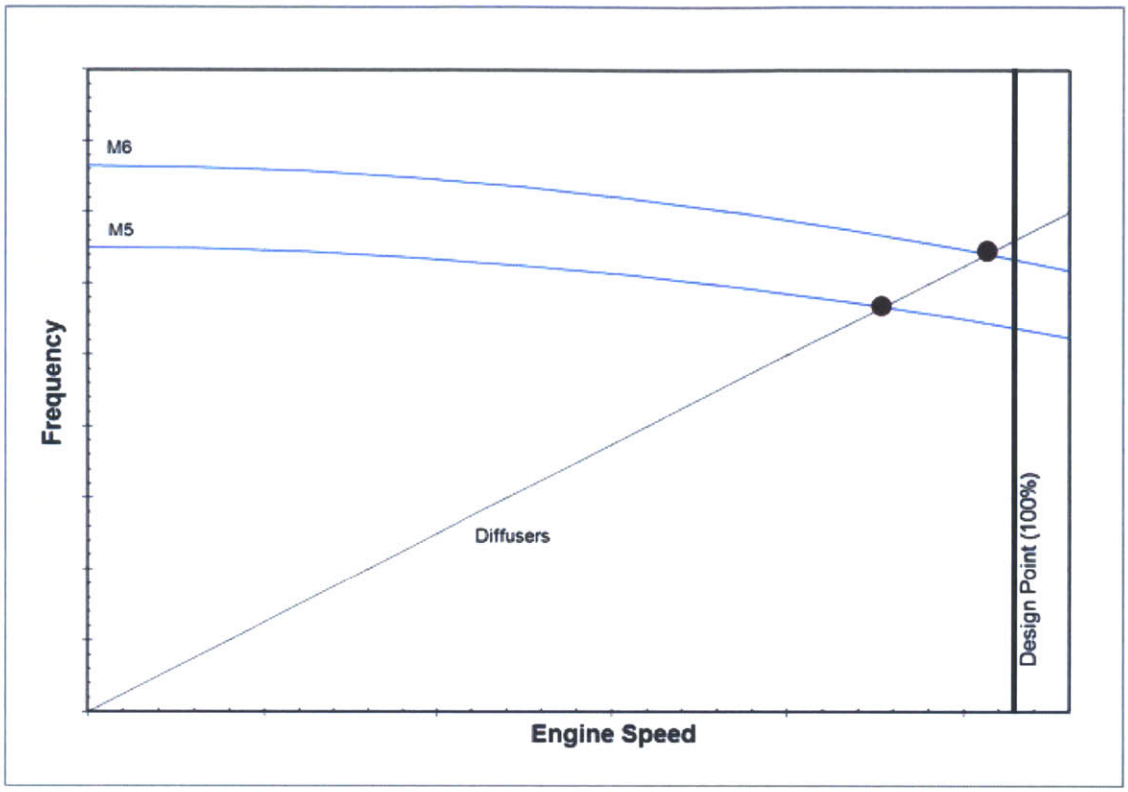

Figure 1-4: Splitter blade Campbell diagram showing edgewise modes 5 and 6.

with blade dominant and disk dominant motion with a solid line to highlight families of modes, therefore, the true veering behavior is not explicitly shown. Modes near the intersection of these mode families may exhibit "modal coupling" of both the blade and backwall mode shapes. The utility and construction of the SAFE diagram will be revisited in Chapter 3.

The Goodman diagram relates the stress state of the component under vibration to the material capability. It shows alternating stress versus mean stress and a curve representing the material's HCF capability at a particular temperature for a given number of vibratory cycles. The diagram is useful when the stress state has been measured by strain gauge or inferred using lightprobes, as it can be directly related to the material's capability. Without physical measurements of a particular vibratory mode of interest, this diagram can be used with the finite element method (FEM) derived steady state stress and scaled modal stresses to find the location which may fail first through HCF during prolonged vibration. The Goodman diagram, like the

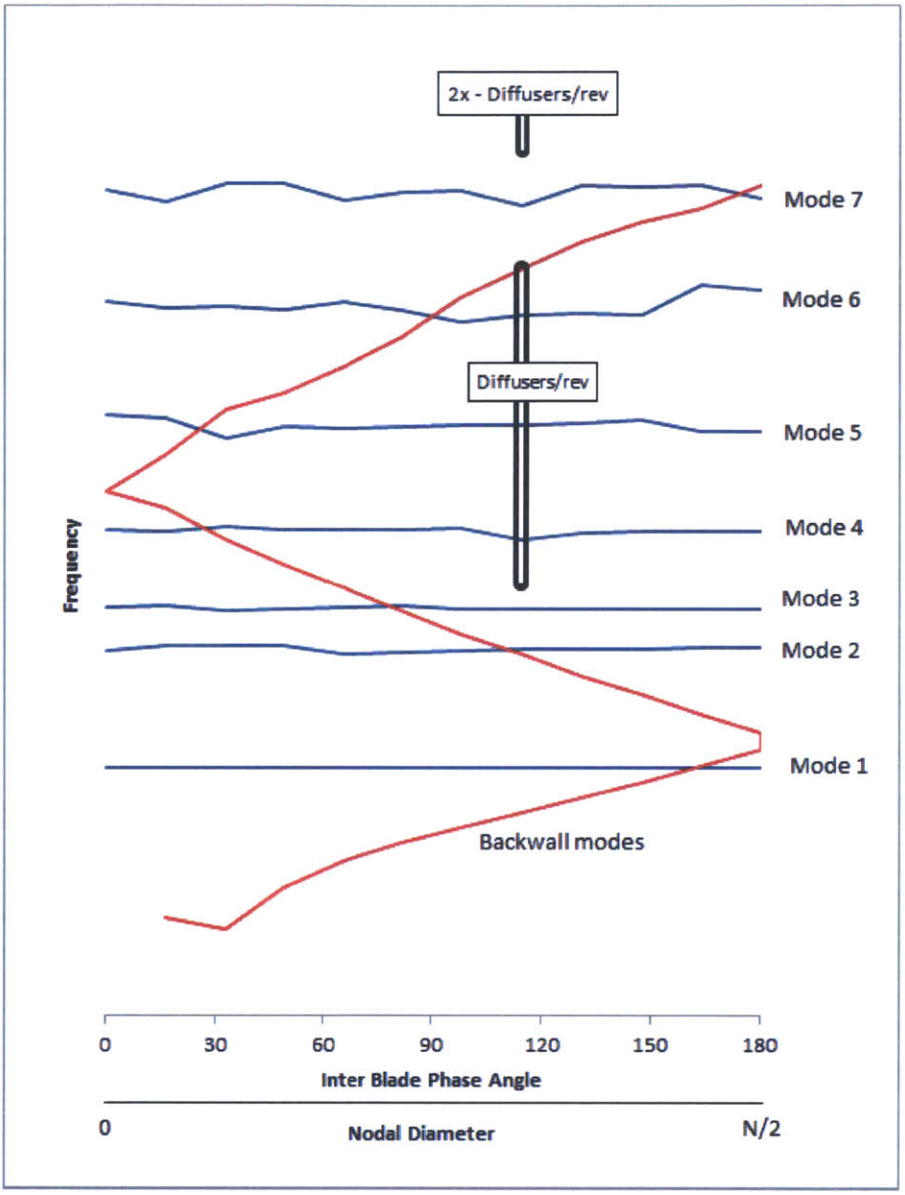

Figure 1-5: Simplified SAFE diagram of the splitter blade (blue) and backwall modes (red).

Campbell and SAFE diagrams, does not predict the level of response as it only helps to identify where a potential failure may occur for a particular vibration mode.

1.3 Previous Work

The forcing function imposed on the centrifugal impeller is not unique to the impeller design studied in this thesis and has been shown to be generic on several other centrifugal compressor stages as a result of the impeller-diffuser interaction. Through experimental results, Ziegler et al. [7] identified the diffuser vanes as the source of the unsteadiness seen by the impeller blades. They found that by reducing the vaneless space, the velocity fluctuations at the exducer could be significantly enhanced while the performance of the stage could be increased due to a reduction in the separated region exiting the impeller. Smythe [18] built upon these results by hypothesizing that the time averaged incidence at the diffuser leading edge sets the unsteady pressure distribution at the impeller trailing edge. She studied two centrifugal stages which differed only in the size of the vaneless space with the shorter vaneless space stage having a notable HCF concern. As a result of the increased incidence angle, she found that the stage with the reduced vaneless space had a stronger unsteady pressure distribution at the impeller trailing edge. Among other stages, Villanueva [20] also studied the two centrifugal stages researched by Smythe. He showed that the difference in the static pressure from the pressure surface to the suction surface at the diffuser vane leading edge sets the level of unsteady loading experienced by the impeller blades. This difference in pressure at the diffuser leading edge is a result of the change in incidence angle onto the diffuser vane as the vaneless space is reduced.

Gould [9] studied the same research impeller which is the subject of this thesis and found that the unsteady loading acting on the impeller blade is set by three key parameters: 1) the magnitude of the unsteadiness is set by the radial gap between the impeller and diffuser; 2) the attenuation of the unsteadiness is set by the DeHaller number, or the relative frame diffusion; and 3) the chordwise distribution of the unsteady loading is set by the relative Mach number of the through flow.

More recently, Lusardi [14] compared three centrifugal stages designed by different manufacturers and found three physical mechanisms shared between the designs that set the level of unsteadiness: 1) unsteady flow into the diffuser inlet creates a

fluctuation in pressure at the diffuser leading edge which is the source of the pressure wave that propagates upstream along impeller blade surface; 2) pressure side and suction side waves propagating upstream can be out of phase which can amplify the unsteady loading; and 3) as the impeller blade sweeps through the non-uniform static pressure field of the diffuser inlet it experiences high pressure when in close proximity to the diffuser vane and low pressure between vanes.

Methods to combine FEM and CFD codes to assess the forced response of an impeller stage have been employed previously. Mansour and Kruse, as described by Smythe [18], used numerical simulations to assess the forced response in a centrifugal stage. Their results showed that forced response assessments using FEM and CFD can agree reasonably well with measured strain gauge data. A similar method of assessing the impeller's HCF response is used in this thesis.

It is the aeromechanical response of the impeller blades to unsteady loading generated by the impeller-diffuser interaction that is the subject of this thesis. The goal is to understand the physical mechanisms which facilitate the most efficient energy transfer from the unsteady flow field to the vibrating structure, and thus, a strong forced response.

1.4 Aeromechanical Attributes of the Research Stage

The research centrifugal compressor stage assessed here is representative of a modern high-performance design. It is comprised of an unshrouded rotating impeller with both main and splitter blades, with the splitter blades having a shorter chord than the main blades. Effort is placed on the response of the splitter blade, particularly, the response of modes 5 and 6, to the excitation generated at the high speed crossing with the number of diffuser passages. Figure 1-6 shows the mode shapes of the two splitter blade modes of interest. Lightprobe data from previous engine tests showed a markedly higher response from mode 6 than mode 5. Indications of HCF found on the splitter blade are thought to be a result of the forced response of mode 6 to the diffuser engine order excitation.

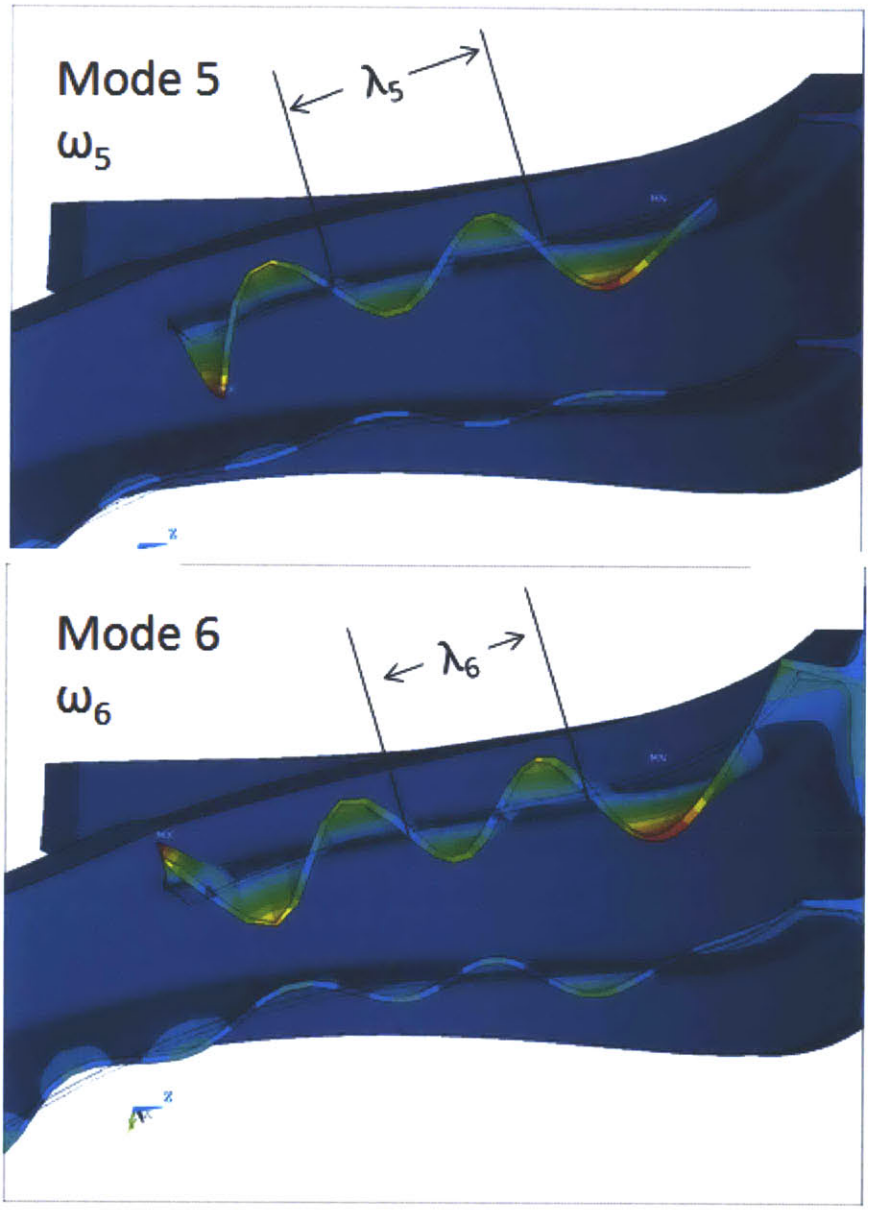

Figure 1-6: Splitter blade mode shapes 5 and 6 for fixed displacement boundary conditions on the sector model cut surfaces.

The diffuser is closely coupled to the impeller through flow in the vaneless space, having a radial gap to exducer radius around 0.039. The peak unsteady loading (amplitude of the net unsteady pressure difference across the splitter blade normalized to the exducer dynamic head) at the aerodynamic design point is known to be about 0.6 [9]. Additionally, the impeller studied here has backwall (disk) modes within the

operating range in proximity to the splitter blade modes and the diffuser excitation.

In summary, for purposes of studying the forced response of a centrifugal compressor stage, the aeromechanical attributes of this stage include the following:

1. blade modes in the operating range which are known to have responded to the diffuser excitation;

2. unsteady loading generated by the impeller-diffuser interaction acting on the impeller blades; and

3. backwall modes close in frequency to blade modes at the diffuser engine order excitation.

1.5 Technical Objective

The overall goal of this thesis is to determine and quantify the physical mechanisms that influence the forced response of a centrifugal compressor stage impeller at resonance due to the unsteady loading generated by the impeller-diffuser interaction. These mechanisms will be elicited through various computational models of the forced response using unsteady loading computed with CFD and structural mode shapes computed through FEM analysis.

The research questions include:

1. Why do some resonances determined from the Campbell diagram exhibit a higher response than others during operation?

2. How can the physical mechanisms which lead to resonance be used to assess design risk?

3. What physical mechanisms influence the forced response in the proximity of blade-disk mode coupling?

1.6 Research Contributions

The findings of this research highlight the conditions and the associated physical mechanisms that set the forced response of a centrifugal compressor stage impeller at resonance due to the impeller-diffuser interaction. These findings include,

1. Forcing frequency versus natural structural frequency:
   (a) facilitates narrow frequency band energy transfer when the forcing frequency and natural frequency are nearly equal, and
   (b) diminishes response when the forcing frequency is not equal to a natural frequency of the structure.
2. Forcing wavelength versus natural structural wavelength:
   (a) facilitates energy transfer where the spatial distribution of the unsteady loading and mode shape are well correlated, and
   (b) enhances response when the ratio of the forcing wavelength to the structural wavelength is between 0.5 and 1.5.
3. Physical speed of the crossing:
   (a) scales the loading fluctuation with exducer dynamic head for similar corrected conditions, and
   (b) increases the forced response risk of high speed crossings as the modal force scales with the magnitude of the loading fluctuation.
4. Modal displacement at the trailing edge:
   (a) enhances vibratory energy transferred to the structure as the unsteady loading is highest in the vicinity of the trailing edge, and
   (b) indicates potential blade-backwall mode coupling which alters the calculated modal work and forced response amplitude.
5. Blade-backwall mode placement:

(a) reduces the impact general structural stiffening may have on mitigating the forced response if blade and backwall dominant modes begin to couple, and

(b) increases sensitivity of the forced response to variations in geometry if blade and backwall dominant modes couple at a known excitation frequency.

The utility of the findings is in assessing the risk of blade mode resonance as a result of the diffuser excitation. In addition, three methods used to elicit the findings are also important technical contributions.

1. A model of a two mass-spring system representing the mass and stiffness of the disk and blades shows good agreement with the forced response behavior of the impeller in the vicinity of a veering point. This model represents a simple tool for verifying the forced response sensitivity of a system with modal coupling.

2. The dependence of the forced response on the spatial correlation of unsteady loading and mode shape is revealed through a simple Bernoulli-Euler beam model. This model assesses the forced response of a beam to a spatially distributed traveling load. The strength of the forced response is quantified as a function of the forcing wavenumber to structural mode shape wavenumber ratio.

3. The method of using a simplified SAFE diagram offers an efficient means to group airfoil and backwall dominant modes and identify regions of modal coupling in the vicinity of an excitation.

These three methods, together with the enumerated conditions and physical mechanisms identified above, provide insight into the forced response of a centrifugal impeller due to the impeller-diffuser interaction.

1.7 Thesis Outline

This thesis is organized as follows:

Chapter 1

Chapter One describes the background of centrifugal compressor stage HCF issues and motivation for the current study. Chapter 1 also delivers the technical objective: identify the physical mechanisms which set the forced response strength of the impeller.

Chapter 2

Chapter Two investigates how continuous systems, like taut strings and Bernoulli-Euler beams, experience a forced response due to unsteady spatially distributed traveling loading. The behavior of these systems is used to interpret the forced response of a centrifugal compressor stage which is a far more complex system.

Chapter 3

Chapter Three describes the structural modes of and forcing function acting on the research centrifugal compressor stage impeller. The method used to calculate the forced response of the impeller is described and an outline of the computational models analyzed is presented.

Chapter 4

Chapter Four presents the results of the computational models assessed and how each model helps to elucidate the underlying mechanisms driving the forced response of the centrifugal impeller.

Chapter 5

Chapter Five presents a risk assessment decision tree to assess the relative risk of a resonant response due to the impeller-diffuser interaction using the physical mechanisms identified in this thesis.

Chapter 6

Chapter Six summarizes the findings and puts forward recommendations for future

research that builds upon the results presented.

Chapter 2

Forced Response

2.1 Simplification of the Impeller Blade Forced Response Problem

The unsteady loading and vibratory mode shape for the centrifugal impeller have characteristic wavelengths. The wavelength of the forcing function is attributed to the acoustic wave found traversing the surface of the impeller blade as shown in Section 1.2.2. The chordwise distribution of the loading clearly has the appearance of a traveling wave with measurable wavelength as shown in Figure 1-3. The wavelength of the structure also has a measurable wavelength due to the vibratory mode shape of the splitter blade, seen in Figure 1-6. From this observation it is hypothesized that the correlation of these two characteristic wavelengths is a necessary condition that sets the forced response of a centrifugal impeller. To explore this idea on a fundamental level, a study of how continuous systems, such as taut strings and beams, resonantly respond to spatially distributed traveling forces is investigated. The two systems are used to elucidate the temporal and spatial relationship between the forcing function and structure conducive to a high response.

2.2 Forced Response of Classical Continuous Systems to Traveling Wave Loading

Two classical undamped continuous systems, taut strings and Bernoulli-Euler (BE) beams, are considered to elicit the attributes of the structure and a spatially distributed loading that enhance the vibratory response. Despite the lack of dispersion in taut strings in comparison to beams, both systems are presented to reveal the effect dispersion has on the forced response of the centrifugal impeller. The separation of variables procedure performed here is an extension of the method presented by A. W. Leissa [13].

2.2.1 Taut Strings

The first system considered is a taut string. The transverse vertical vibration of a taut string, shown schematically in Figure 2-1, with tension, T, is governed by the differential equation,

$$\rho A \frac{\partial^2 w}{\partial t^2} - T \frac{\partial^2 w}{\partial x^2} = P(x,t) \tag{2.1}$$

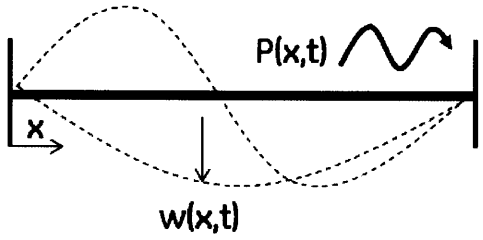

Figure 2-1: General schematic of taut string with spatially distributed traveling loading.

where ρ is the mass density, A is the cross sectional area and $P(x,t)$ is a spatially distributed applied load per unit length. For a traveling wave $P(x,t) = P_o e^{-iKx} e^{i\Omega t}$, P_o is the amplitude of the forcing function, Ω is the forcing frequency and K is the wavenumber representing the spatial distribution of the forcing function. The taut

string has a length of L and the boundary conditions are fixed at both ends such that the displacement is zero, $w((x = 0, L), t) = 0$. The general solution for the system is of the form, $w(x, t) = \phi(x)e^{i\Omega t}$ such that,

$$T\frac{\partial^2\phi}{\partial x^2} + \rho A\Omega^2\phi = P_o e^{-iKx} \tag{2.2}$$

The wavenumber, k, of the taut string's vibratory response is given by,

$$k^2 = \frac{\rho A}{T}\Omega^2 \tag{2.3}$$

The general solution is the product of $e^{i\Omega t}$ with the sum of the homogeneous, ϕ_h, and particular solution, ϕ_p. The homogeneous solution is assumed to be of the form

$$\phi_h(x) = C_1 sin(kx) + C_2 cos(kx) \tag{2.4}$$

where C_1 and C_2 are constants to be determined from the imposed boundary conditions. The form of the particular solution is taken to be $\phi_p = C_5 e^{-iKx}$, where C_5 is a constant determined to satisfy Equation 2.2 to yield the particular solution as

$$\phi_p(x) = -\frac{\frac{P_o}{T}}{k^2 - K^2}e^{-iKx} \tag{2.5}$$

The full general solution is then

$$w(x, t) = \left(C_1 sin(kx) + C_2 cos(kx) - \frac{\frac{P_o}{T}}{k^2 - K^2}e^{-iKx}\right)e^{i\Omega t} \tag{2.6}$$

where the constants are solved for using the boundary conditions. For the two unknown constants there exist two boundary conditions which can be written as a set of coupled equations in the form

$$\begin{bmatrix} w(x=0,t) \\ w(x=L,t) \end{bmatrix} =$$

$$= \left(\begin{bmatrix} 0 & 1 \\ sin(kL) & cos(kL) \end{bmatrix} \times \begin{bmatrix} C_1 \\ C_2 \end{bmatrix} - \frac{\frac{P_o}{T}}{k^2 - K^2} \begin{bmatrix} 1 \\ e^{-iKL} \end{bmatrix} \right) e^{i\Omega t} = \begin{bmatrix} 0 \\ 0 \end{bmatrix} \quad (2.7)$$

The n^{th} natural frequency of the taut string with fixed ends is found by solving the eigenvalue problem of the homogeneous or unforced solution in Equation 2.4 which yields [16]

$$\omega_n = \frac{n\pi}{L}\sqrt{\frac{T}{\rho A}} \quad (2.8)$$

and the corresponding wavenumbers, or wavelengths λ_n, are given by

$$k_n = \frac{2\pi}{\lambda_n} = \frac{n\pi}{L} \quad (2.9)$$

The phase speed for the taut string is a constant which indicates that taut strings are non-dispersive such that vibrations of all frequencies or wavelengths propagate at the same speed given by

$$c_p = \frac{\Omega}{k} = \sqrt{\frac{T}{\rho A}} \quad (2.10)$$

2.2.2 Bernoulli-Euler Beams

The second system considered is the Bernoulli-Euler beam, shown schematically in Figure 2-2, which is more representative of the vibration of the impeller splitter blade. Similar to the general steps outlined for the taut string, the transverse vertical vibration of the BE beam is governed by the differential equation,

$$\rho A \frac{\partial^2 w}{\partial t^2} + EI \frac{\partial^4 w}{\partial x^4} = P(x,t) \quad (2.11)$$

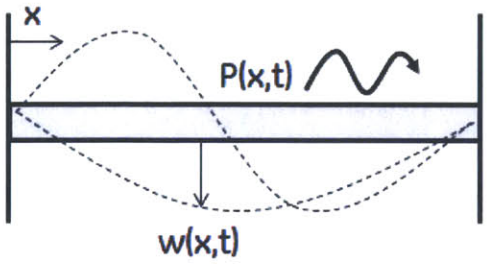

Figure 2-2: General schematic of Bernoulli-Euler beam with spatially distributed traveling loading and clamped boundary conditions.

where ρ is also the mass density, A is the cross sectional area and $P(x,t)$ is a spatially distributed applied load per unit length. For a traveling wave $P(x,t) = P_o e^{-iKx} e^{i\Omega t}$, P_o is the amplitude of the forcing function, Ω is the forcing frequency, and K is the wavenumber representing the spatial distribution of the forcing function. E is Young's modulus of elasticity and I is the moment of inertia of the cross section. The BE beam has a length of L and the boundary conditions are clamped at both ends such that both the displacement and slope are zero, $w((x = 0, L), t) = \dot{w}((x = 0, L), t) = 0$. The general solution for the system is assumed to be of the form, $w(x,t) = \phi(x) sin(\Omega t)$ such that,

$$EI\frac{\partial^4 \phi}{\partial x^4} - \rho A \Omega^2 \phi = P_o e^{-iKx} \tag{2.12}$$

The wavenumber, k, of the BE beam's vibratory response is given by,

$$k^4 = \frac{\rho A}{EI}\Omega^2 \tag{2.13}$$

The general solution is the product of the sum of the homogeneous, ϕ_h, and particular solution, ϕ_p, with $e^{i\Omega t}$. The homogeneous solution can be of the form

$$\phi_h(x) = C_1 sin(kx) + C_2 cos(kx) + C_3 sinh(kx) + C_4 cosh(kx) \tag{2.14}$$

where C_1, C_2, C_3, and C_4 are constants determined by the imposed boundary conditions. The form of the particular solution is taken to be $\phi_p = C_5 e^{-iKx}$, where

C_5 satisfies Equation 2.12 to yield the particular solution

$$\phi_p(x) = -\frac{\frac{P_o}{EI}}{k^4 - K^4} e^{-iKx} \tag{2.15}$$

The full general solution is then

$$w(x,t) = \left(C_1 sin(kx) + C_2 cos(kx) + C_3 sinh(kx) + C_4 cosh(kx) - \frac{\frac{P_o}{EI}}{k^4 - K^4} e^{-iKx} \right) e^{i\Omega t} \tag{2.16}$$

where the constants are solved for using the boundary conditions. For the four unknown constants there exist four boundary conditions which can be written as a set of coupled equations in the form

$$\begin{bmatrix} w(x=0,t) \\ \dot{w}(x=0,t) \\ w(x=L,t) \\ \dot{w}(x=L,t) \end{bmatrix} =$$

$$= \left(\begin{bmatrix} 0 & 1 & 0 & 1 \\ k & 0 & k & 0 \\ sin(kL) & cos(kL) & sinh(kL) & cosh(kL) \\ kcos(kL) & -ksin(kL) & kcosh(kL) & ksinh(kL) \end{bmatrix} \times \begin{bmatrix} C_1 \\ C_2 \\ C_3 \\ C_4 \end{bmatrix} + \right.$$

$$\left. + \frac{\frac{-P_o}{EI}}{k^4 - K^4} \begin{bmatrix} 1 \\ -iK \\ e^{-iKL} \\ -iKe^{-iKL} \end{bmatrix} \right) e^{i\Omega t} = \begin{bmatrix} 0 \\ 0 \\ 0 \\ 0 \end{bmatrix} \tag{2.17}$$

The n^{th} natural frequency of the BE beam with clamped ends is found by solving

the eigenvalue problem of the homogeneous or unforced solution in Equation 2.14 which yields [12]

$$\omega_n = \frac{\beta_n^2}{L^2}\sqrt{\frac{EI}{\rho A}} \tag{2.18}$$

and the corresponding wavenumbers, or wavelengths λ_n, are given by

$$k_n = \frac{2\pi}{\lambda_n} = \frac{\beta_n}{L} \tag{2.19}$$

where β is a function of the boundary conditions. For a BE beam clamped at both ends β is $(n + 1/2)\pi$ [4]. Additionally, the BE beam model is only valid for phase speed less than the rod-wave velocity C_r defined as

$$C_r = \sqrt{\frac{E}{\rho}} \tag{2.20}$$

as this is the largest speed with which physical waves can propagate under the plane stress condition assumed. The phase speed for the BE beam is a function of the wavenumber which indicates that BE beams are dispersive unlike taut strings. The dispersion in BE beams allows vibrations at higher frequencies to outrun vibrations at lower frequencies with the physical limit of the phase speed being the rod-wave velocity [12].

$$c_p = \frac{\Omega}{k} = k\sqrt{\frac{EI}{\rho A}} \tag{2.21}$$

The BE beam model also neglects rotational inertia, shear deformations and the effects of Poisson's ratio [12]. Higher fidelity models, such as the Rayleigh or Timoshenko beam models which include some of these effects, are not considered here for purposes of simplicity.

2.3 Resonance Conditions and Implications

As shown in the full general solutions given in Equations 2.6 and 2.16, both the taut string and BE beam steady-state response equations are functions of the forcing frequency, Ω, and forcing wavenumber, K. The equations for the general solutions along with Equations 2.7 and 2.17, which relate the system constants, can be numerically evaluated for a range of forcing frequencies and wavenumbers such that the amplitude of the response of either system is simply expressed as

$$|w(x,t)| = f\left(\frac{\Omega}{\omega_1}, \frac{K}{k_1}\right) = f(r,\kappa) \tag{2.22}$$

where r is the ratio of forcing frequency to the system's fundamental frequency, $\frac{\Omega}{\omega_1}$, and κ is the ratio of the forcing wavenumber to the system's fundamental wavenumber, $\frac{K}{k_1}$. Fundamental refers to the lowest valued eigenvalue of the respective system, where $n = 1$ in Equations 2.8 and 2.9 for the taut string and 2.18 and 2.19 for the beam.

2.3.1 Map of Resonance Spectrum

Figures 2-3 and 2-4 show the forced response spectrum for the taut string and the BE beam as described by Equation 2.22. On both figures a solid red line is shown to highlight the locus of highest responses. Note that for the taut string the red curve is a straight line defined by $\kappa = r$, whereas for the BE beam it takes on the form $\kappa = \sqrt{r}$. The slope of the red curve is the reciprocal of the phase speed which is constant for a taut string but for a beam is a function of the vibration wavenumber (or frequency). In each system, the equation defining the red curve is found by inspection of the coupled set of equations, namely Equations 2.7 and 2.17. In each system's coupled set of equations an apparent singularity exists in the spatial domain when the system responds with a wavenumber equal to the forcing wavenumber. For the string the singularity condition is:

$$k^2 - K^2 = 0 \tag{2.23}$$

Substituting in for k Equation 2.3 yields

$$\frac{\rho A}{T}\Omega^2 = K^2 \tag{2.24}$$

The physical constants can be normalized by relating the parameters back to the fundamental frequency and wavenumber for mode 1 using Equations 2.8 and 2.9 respectively to yield

$$\frac{{k_1}^2}{{\omega_1}^2}\Omega^2 = K^2 \tag{2.25}$$

which can be further simplified to the expression noted earlier:

$$\kappa = \frac{K}{k_1} = \frac{\Omega}{\omega_1} = r \tag{2.26}$$

Similarly, for a BE beam the resonant condition is

$$k^4 - K^4 = 0 \tag{2.27}$$

Substituting in for k Equation 2.13 yields

$$\frac{\rho A}{EI}\Omega^2 = K^4 \tag{2.28}$$

Again, the physical constants can be normalized by relating the parameters back to the fundamental frequency and wavenumber for mode 1 using Equations 2.18 and 2.19, respectively, to yield

$$\frac{{k_1}^4}{{\omega_1}^2}\Omega^2 = K^4 \tag{2.29}$$

which can be further simplified to the expression noted earlier:

$$\kappa = \frac{K}{k_1} = \sqrt{\frac{\Omega}{\omega_1}} = \sqrt{r} \tag{2.30}$$

Both Equations 2.26 and 2.30 describing the conditions under which an apparent resonance occurs in the spatial domain reveal a fundamental relationship between

the phase speed of the structural vibration and the phase speed of the traveling load during a forced response. Substitution of the structural phase speed, Equation 2.10 or 2.21, into $k^2 - K^2 = 0$ for the string or $k^4 - K^4 = 0$ for the beam respectively, indicates that the resonance is maximized when the phase speed of the structure matches the phase speed of the forcing function

$$c_p = \frac{\Omega}{K} = c_f \tag{2.31}$$

The red curve in both spectrum plots shows Equations 2.26 or 2.30 for the taut string or BE beam respectively. The red curve represents the condition when the phase speed of the forcing function is equal to the respective phase speed of the vibration mode for the taut string or the BE beam. Figures 2-3 and 2-4 represent the full spatial and temporal forced response domain for the given system as a result of a spatially distributed traveling load.

2.3.2 Temporal Response

The horizontal axis of the forced response spectrum plots of Figure 2-3 and 2-4 clearly shows the natural frequencies of the respective system response. From Equation 2.8 for the taut string's natural frequencies, the modes are expected to occur temporally when $\frac{\Omega}{\omega_1} = 1, 2, 3, 4....$ Similarly for the BE beam natural frequencies from Equation 2.18, the modes are expected to occur temporally when $\frac{\Omega}{\omega_1} = 1, 2.778, 5.444, 9....$ In both response spectrum plots these natural frequencies show up as clear bands with the highest response occurring at some value of $\frac{K}{k_1}$. Away from the expected natural frequencies, the response drops off steeply with little response from both systems when the forcing frequency is different from the natural frequency. Figure 2-5 indicates that the beam's amplitude response, at $\frac{K}{k_1} = 3$, has little response away from $\frac{\Omega}{\omega_1} = 1, 2, 3, 4...$, the expected natural frequencies. As there is no damping in this BE beam model, the response at resonance is infinite but limited, of course, to the grid resolution of the simulation.

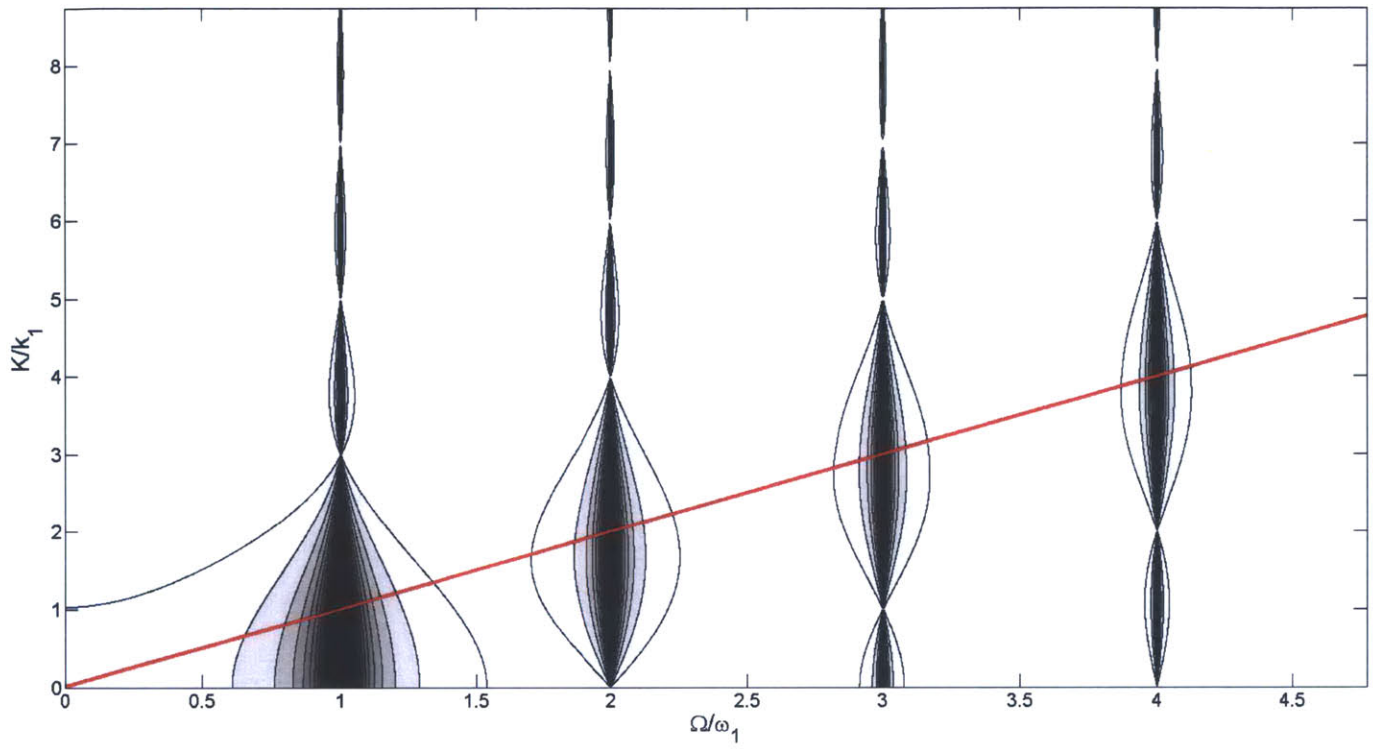

Figure 2-3: Amplitude response spectrum for a taut string fixed at both ends forced by a spatially distributed traveling load.

2.3.3 Spatial Response

The vertical axis of the forced response spectrum plots, Figures 2-3 and 2-4 for the taut string and BE beam respectively, indicates the correlation between the forcing wavenumber and mode shape wavenumber, $\frac{K}{k_1}$. Both systems indicate that the forced response is maximized over a narrow range of $\frac{K}{k_1}$. From the Equation for a taut string's natural wavenumbers, Equation 2.9, a matching between the loading's spatial distribution and the natural modes shapes occurs when $\frac{K}{k_1} = 1, 2, 3, ...$ For the BE beam with natural wavenumbers described by Equation 2.19, the wavenumber matching relative to the fundamental wavenumber occurs when $\frac{K}{k_1} = 1, 1.667, 2.333, 3, ...$ Since the strongest response of either system occurs when these wavenumber ratios are met, the implication is that the strongest response occurs when the forcing function wavenumber K matches the general structural mode shape k, or $\frac{K}{k} = 1$. Outside

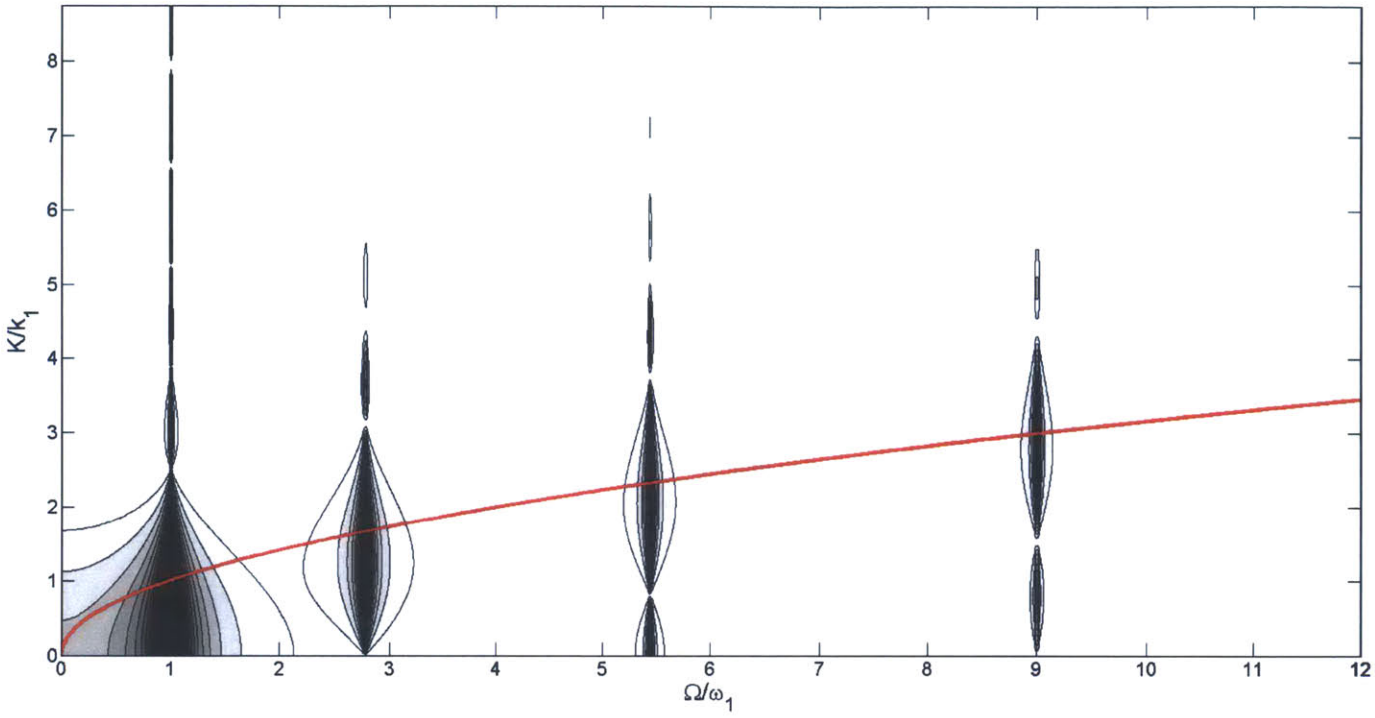

Figure 2-4: Amplitude response spectrum for a Bernoulli-Euler beam clamped at both ends forced by a spatially distributed traveling load.

of this condition, the response falls off steeply such that by $\frac{K}{k} = 1.5$ the response has been reduced to nearly 25% of the matched wavenumber response. Figure 2-6 shows the spatial matching influence on the response for the 4^{th} transverse mode of vibration. The response amplitude has been normalized to a peak value of one with the maximum response occurring at $\frac{K}{k_1} = 3$. This spatial response amplitude shows a series of peaks and zeros with the peak responses falling away toward zero from $\frac{K}{k_1} = 3$.

The maximum forced response in the spatial domain, $\frac{K}{k_1}$, appears more broad band than the response in the temporal domain, $\frac{\Omega}{\omega_1}$, as the maximized response occurs over a larger range. If the wavenumbers are mismatched the amplitude of the response attenuates at a lower rate than the same mismatch in frequencies. The narrow band aspect of the forced response in the temporal domain only permits a forced response of the system when the forcing frequency is closely matched to a natural frequency,

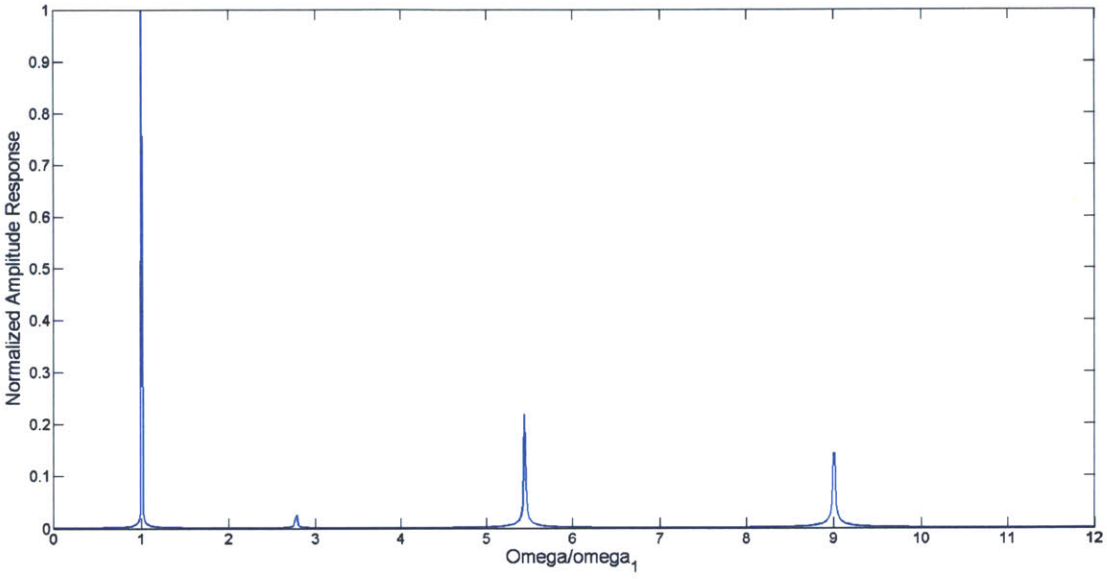

Figure 2-5: Normalized amplitude response of a Bernoulli-Euler beam as a function of the ratio: forcing frequency to mode 1 natural frequency at $\frac{K}{k_1} = 3$.

regardless of the spatial matching between the forcing function and mode shapes.

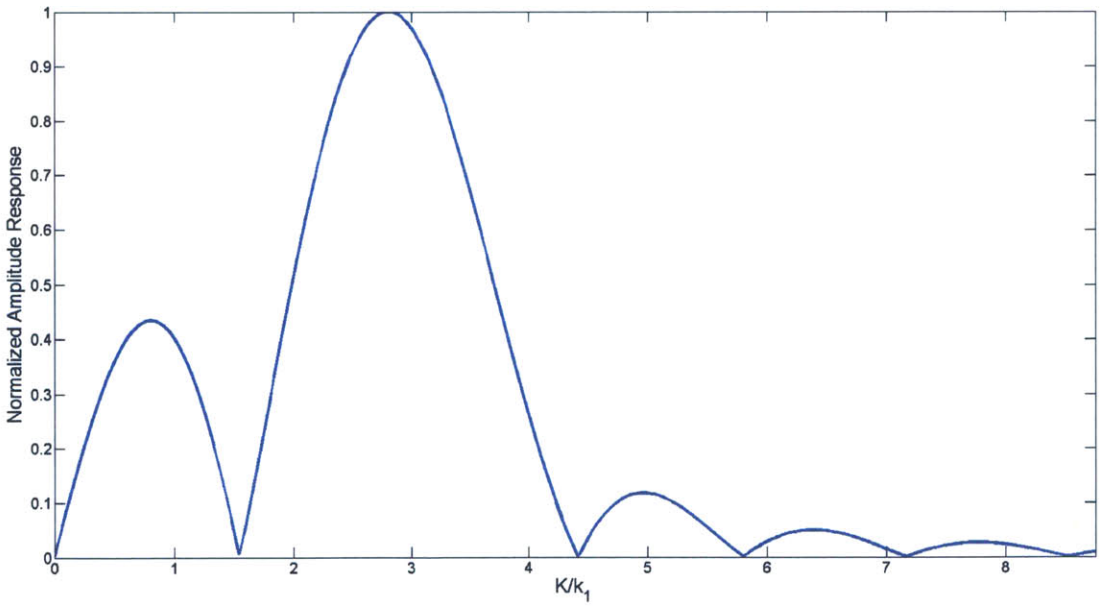

Figure 2-6: Normalized amplitude response of a Bernoulli-Euler beam as a function of the ratio: forcing wavenumber to mode 1 natural wavenumber at $\frac{\Omega}{\omega_1} = 9$.

2.3.4 FEM Modeling in the Time Domain

To further explore the concept of wavenumber matching on the forced response of a beam, a 3D FEM model of a beam with clamped end conditions and a traveling spatially distributed surface pressure described by $P(x,t) = P_o sin(\Omega t - Kx)$ is constructed. The forcing frequency is chosen to match a natural frequency of the system and the forcing wavenumber is varied in separate models while the final steady state amplitude is recorded. The FEM model is run as unsteady in the time domain. Material damping is applied using a Raleigh damping model such that the equivalent damping ratio is 2% for the natural frequency chosen to be excited. The mode of interest is shown in Figure 2-7 which is the 6^{th} natural mode of the system, or 4^{th} vertical transverse mode, as torsional, vertical transverse, and horizontal transverse modes exist. Table 2.1 shows the first six modes of the beam found from an FEM modal analysis. Modes 1, 2, 4 and 6 are vertical transverse modes. The beam is modeled as a steel beam with a height/length of 0.02, width/length of 0.10, and a normalized length of 1, where the normalizing value is 50 inches. For the aspect ratio of this beam, the modes match well with BE beam theory despite the fact that the Bernoulli-Euler approximation of a beam's response does not incorporate shear stress, rotational inertia and the effect of Poisson's ratio as in the FEM model. Additionally, the wavenumber given by BE beam theory is less than approximately 0.5% different than that found from the FEM model.

FEM Mode #	FEM Frequency (Hz)	BE Theory Frequency (Hz)	% Difference	Description
1	82.323	81.10	1.49%	1st vertical transverse mode
2	226.13	225.27	0.38%	2nd vertical transverse mode
3	384.86			1st horizontal transverse mode
4	441.46	441.52	-0.01%	3rd vertical transverse mode
5	473.19			1st torsional mode
6	726.13	729.86	-0.51%	4th vertical transverse mode

Table 2.1: FEM-found modes of the beam model with comparison to Bernoulli-Euler beam theory for the vertical transverse modes

Figure 2-8 shows the normalized amplitude response from BE beam theory and the ANSYS 3D FEM results. The blue curve represents the response found from

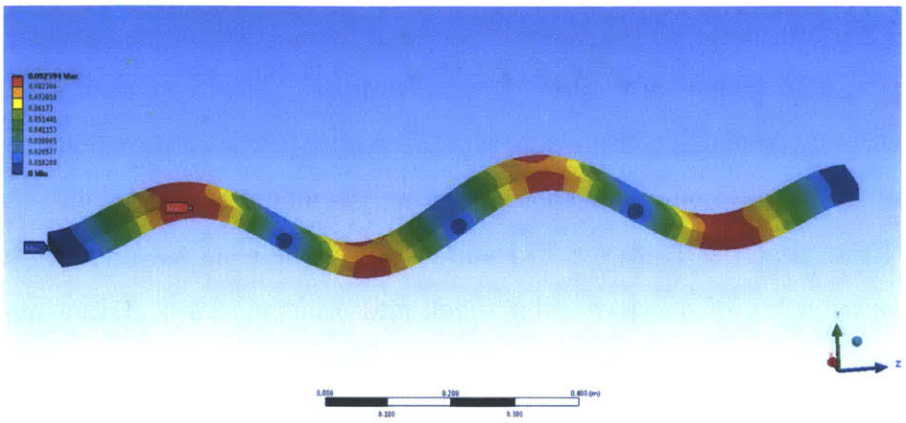

Figure 2-7: Mode shape of FEM beam model to be excited by traveling pressure load spatially distributed on top surface.

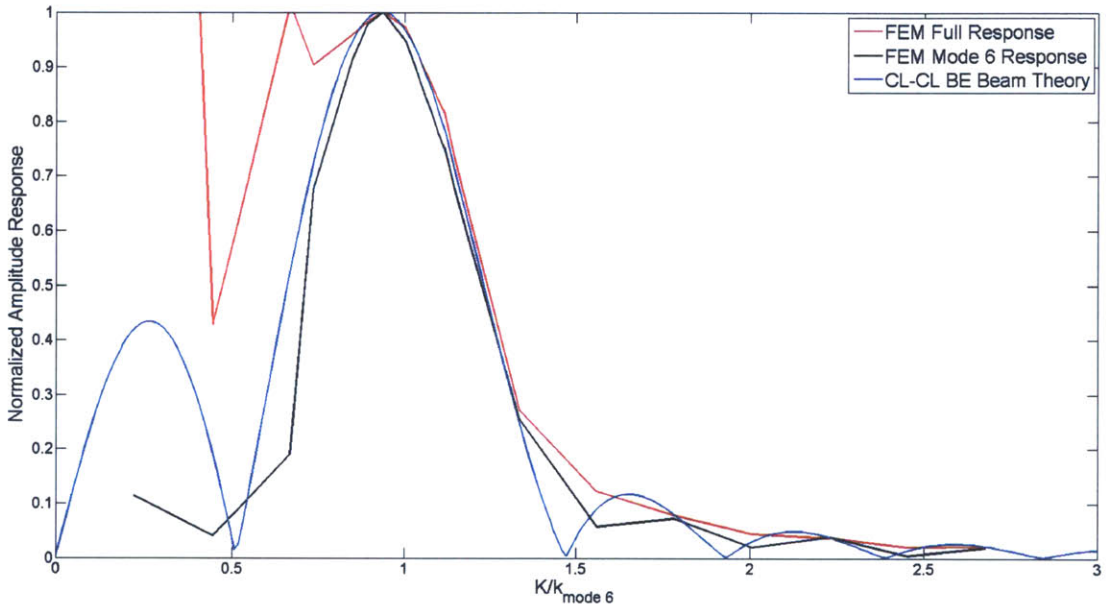

Figure 2-8: Comparison of FEM model and Bernoulli-Euler beam theory response.

Bernoulli-Euler beam theory for the 4^{th} vertical transverse mode. The black curve represents the FEM beam's response for the same transverse mode (system mode 6) found from an FFT of the beam's response. The red curve is the full response of the beam which includes the vibratory response of all modes in the system. The displacement of the beam is recorded at $5/8L$, where L is the beam's length. This location is near a point of maximum modal displacement for mode 6. The mismatch between

the FEM full response and BE beam theory is a result of the chosen general solution in Equation 2.16 which only allowed the system to respond at a single frequency and shape to a particular forcing function. In reality, the forced response of a beam should be closer to a linear superposition of all the modal responses, like that found through FEM analysis. However, in some instances the response may be dominated by the contribution of one particular mode and other modal contributions may be neglected. Figure 2-8 shows good agreement between the full response and BE theory when $\frac{K}{k_{mode6}} > 0.75$ indicating that the vibratory energy is primarily confined to mode 6. As $\frac{K}{k_{mode6}}$ approaches zero, the forcing wavelength goes to infinity which results in a uniform loading distribution. A uniform loading distribution is better suited at exciting lower order modes, as low order modes have longer structural wavelengths that correlate more closely to the forcing function than higher order modes. Figure 2-9 shows the magnitude response of modes 1 through 6 from an FFT of the full response. As $\frac{K}{k_{mode6}}$ decreases the response of lower order modes begins to increase. Together, the results of the FEM modeling and BE beam theory are consistent in that they indicate that the forced response of a structure is maximized when the forcing wavenumber equals the structural mode wavenumber.

2.3.5 Physical Mechanisms Leading to a Resonant Response

The mechanisms that drive a strong forced response in a continuous system like a taut string or a BE beam due to a spatially distributed traveling load are: 1) matching of the forcing frequency and the structural frequency; and 2) matching of the forcing wavenumber and the structural wavenumber. The correlation in both the temporal and spatial domains determines the response of the system.

2.3.6 Suggested Design Methods to Avoid Resonance

As shown in the response spectrum plots, resonance is set firstly by matching in the temporal domain. Identifying when forcing frequencies match with natural structural modes should be the first step in any analysis to avoid resonance of a mechanical

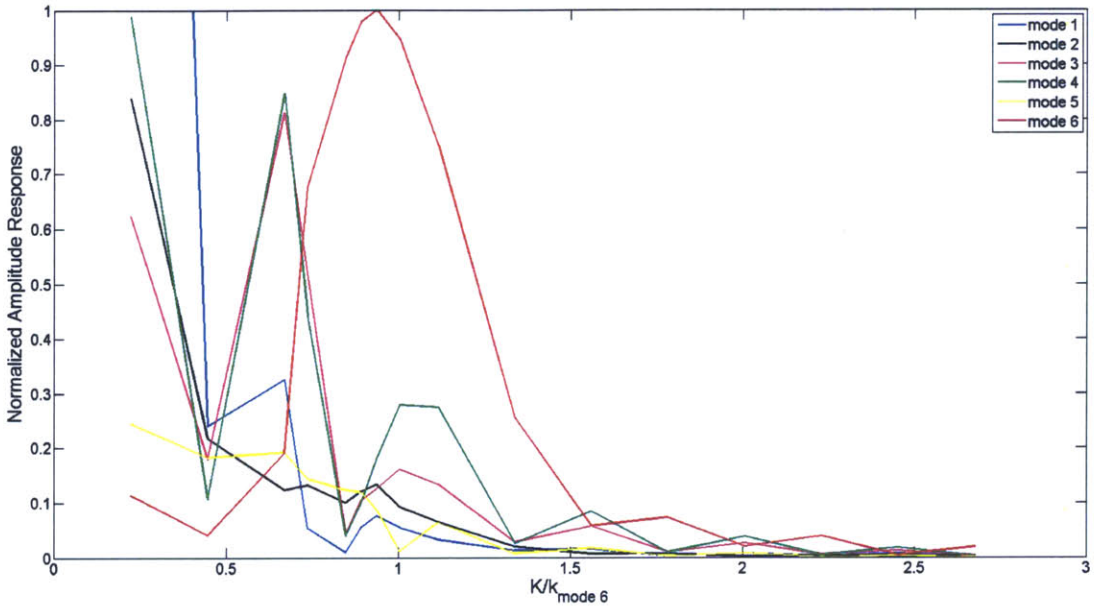

Figure 2-9: FEM model modal response of modes 1 through 6 at $\frac{\Omega}{\omega_1} = 9$ showing the proclivity of lower order mode excitation for $\frac{K}{k_1} < 1$.

system. The Campbell diagram discussed in Chapter 1 does just this as it identifies the speed at which the frequency of a known excitation in the engine matches with natural frequencies. The response spectrum plots, Figures 2-3 and 2-4, go on to suggest that there is a functional dependence of the forced response on the ratio of the forcing wavenumber to the structural wavenumber. As the wavenumber ratio approaches unity, a maximum response is likely. At conditions where the ratio is not between 0.5 and 1.5 the energy associated with the unsteady loading is less capable of amplifying the response. The concept of wavenumber matching will be explored and assessed against the impeller's forced response in Chapter 4 to determine if this is an adequate screening criteria for resonant risk.

2.4 Summary

The response spectrum plots for a taut string and Bernoulli-Euler beam show that the strongest response for either system occurs when both the forcing frequency and

wavenumber match those of the structural mode. If this condition is met the response is maximized; consequently, if the frequencies of the forcing function and structure match but the wavenumber ratio is outside of 0.5 to 1.5, then the level or response can be significantly diminished (by 75% or more). The matching of the forcing wavenumber and structural wavenumber physically implies that the phase speed of the forcing function matches the phase speed of the vibration. The correlation of wavenumbers will be quantified in Chapter 4 for the impeller to assess its effect on setting the strength of the forced response.

Chapter 3

Technical Approach

The research centrifugal compressor stage consists of a closely coupled rotating impeller and stationary discrete passage diffuser which interact to generate a spatially distributed traveling load on the splitter blade. With the unsteady loading and the known modes of vibration for the splitter blade identified on the Campbell diagram, the forced response of the impeller can be estimated by modeling the response as a single degree of freedom (SDOF) problem. The methods used to compute the structural mode shapes, unsteady loading, and maximum amplitude at resonance are discussed in this chapter. The modal force calculation is employed as a tool to quantify the strength of a resonant response and elicit the driving physical mechanisms.

3.1 Modal force calculation

The forcing function and natural mode shapes of the two systems assessed in Chapter 2, taut strings and BE beams, both have sinusoidal waveforms. However, more complex mechanical structures, like the impeller, may not possess the symmetry required to produce mode shapes that can be so easily compared against an unsteady load. The general SDOF model relates the physical displacement to the mode shape by equation [10],

$$w = \frac{F_{modal} Q}{\Omega^2} \phi \tag{3.1}$$

where F_{modal} is the modal force, Ω is the forcing frequency, ϕ is the mass normalized mode shape and Q is the "quality factor" and is related to the damping ratio ζ by

$$Q = \frac{1}{2\zeta} = 250 \tag{3.2}$$

For all computations of the forced response, the total damping is assumed to be dominated by the aerodynamic component and not by the material or mechanical damping [11]. A Q of 250 is assumed as this value is consistent with the average quality factor determined from lightprobe data; however, significant blade-to-blade variation does exist in the available data. Modal strain and stress can also be related by the same scaling as that of the modal displacement. The modal force acting on the structure is calculated as

$$F_{modal} = -\int\int_S \vec{\phi} \cdot (P_r \vec{n})\, dA \tag{3.3}$$

where P_r is the unsteady pressure at the vane passing frequency, n is surface normal, ϕ is the mode shape of interest onto which the unsteady pressure is projected, and the integration is performed over both the suction and pressure sides of the airfoil. Both the spatially varying unsteady pressure and mode shape can be conveniently represented as complex numbers with intrinsic magnitude and phase.

Equations 3.1 and 3.3 are applied to the centrifugal compressor to calculate the modal force and physical displacement of the splitter blades at resonance. The procedure is repeated for variations in boundary conditions, geometry and loadings in different computational models for eliciting the physical mechanism that set the amplitude of the splitter blade forced response. As stated in Section 1.4, the focus of this thesis is on the splitter blade response reflected in lightprobe data; however, the procedure and findings should be applicable to both the main and splitter blade.

3.2 Structural Model: FEM Mode Shape Identification

Like all structural components, the centrifugal impeller has natural modes of vibration. The frequency and shape of the modes are defined by the eigenfrequencies and eigenvectors of the undamped homogeneous solution to the governing equation. The finite element method is used to obtain the natural modes of vibration by modeling the continuous system as a coupled system of m discrete elements with a total of $3*n$ degrees of freedom (DOF). Both the number of nodes, n, and the number of elements are reflected in the structural mesh. The governing differential equation for the response of this system of discrete elemental masses is then,

$$\boldsymbol{M}\ddot{\vec{w}} + \boldsymbol{C}\dot{\vec{w}} + \boldsymbol{K}\vec{w} = \vec{F} \tag{3.4}$$

where $\vec{w}$ is the displacement vector in the spatial coordinates (x, y, z) and time, t. $\mathbf{M}$ is the n-by-n mass matrix, $\mathbf{C}$ is the n-by-n damping matrix, $\mathbf{K}$ is the n-by-n stiffness matrix and $\vec{F}$ is the load vector which represents the total sum of the component forces in x, y, and z acting on the impeller blade, both steady and unsteady in time. For the purposes of finding steady-state loads and vibration modes, the damping matrix contains only zeros. The loads acting on the structure include pressure loads, thermal loads due to temperature variations and the thermal expansion of the material, centrifugal acceleration due to the rotational speed, and clamp loads tying the impeller to the rest of the compressor assembly.

3.2.1 Description of Model

The mode shape is the eigenvector found using an FEM solver. For this study, ANSYS 14 is the FEM solver used. The FEM model is a sector of a full disk with various boundary conditions applied to the nodes of the sector's cut surfaces. The two cut surfaces of the sector model are named the high side (pressure side) and low side (suction side) and are shown schematically in Figure 3-1. Figure 3-2 shows the FEM

mesh of the sector model with a single splitter blade and main blade. Two types of boundary conditions are applied to the sector model: "fixed" boundary conditions and phase lag boundary conditions. Fixed boundary conditions restrain all degrees of freedom of nodes on the cut surfaces while phase lag boundary conditions couple the displacement between the nodes on the cut surfaces with a phase lag in the circumferential direction. The phase lag between the cut surfaces allows the mode shapes of a full wheel, such as those with circumferential wavelengths larger than the sector's wedge angle, to be captured by the sector model alone. By using a sector model instead of a full wheel model, significant computational time can be saved without compromising the accuracy of the result [17].

Modal Analysis

To capture the natural frequencies of the structure at operating conditions, the modal analysis is performed using the strain state induced by the steady-state rotational speed, thermal loads, pressure, and clamp loads. The steady-state condition implies that all time derivatives are zero and the governing equation is reduced to $\boldsymbol{K}\vec{w} = \vec{F}$. The modal FEM analysis solves for the eigenvalues and eigenvectors of the pre-stressed impeller after the steady-state solution has been found.

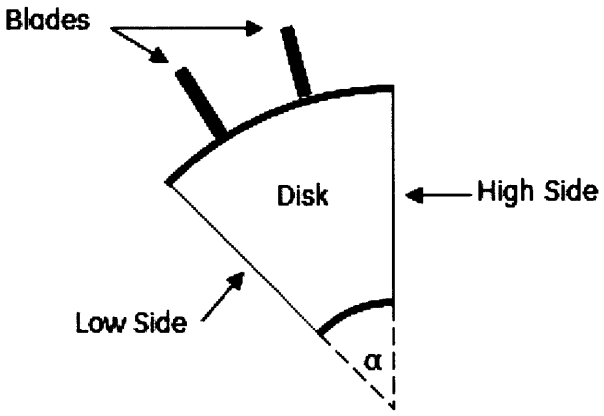

Figure 3-1: Schematic of FEM model with cyclic symmetry boundary conditions coupling nodal displacements between the high and low side cut surfaces.

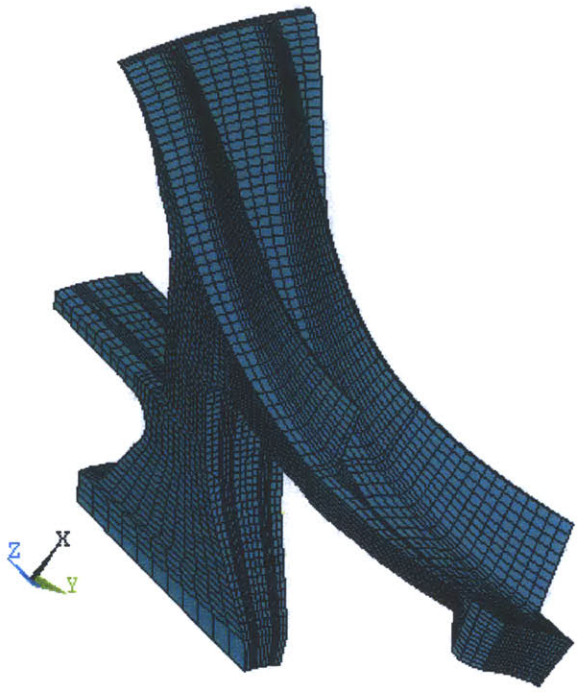

Figure 3-2: FEM mesh of the centrifugal impeller.

For modal analysis using the first set of boundary conditions, the nodes on the cut surface of the sector model are fixed in space after the strain of the steady-state solution has been applied. The fixed boundary condition effectively stiffens the disk which, for airfoil modes of interest in the operating range, nearly removes the contribution of backwall motion from the airfoil mode shapes. This method ensures the airfoil mode is a purely standing wave with uniform phase across the airfoil. Figure 3-3 shows the modal displacement of the splitter blade tip for splitter blade modes 1 through 7 from leading edge to trailing edge with fixed boundary conditions. These modal displacements are similar to the displacement of a Bernoulli-Euler beam with boundary conditions consistent with clamped-free end conditions. The higher order modes have mode shapes with an apparent decreasing spatial wavelength of the structure. By removing the disk's influence on the mode shape with fixed boundary conditions, characteristics of the airfoil structural wavelength relative to the forcing

function wavelength can be isolated and assessed.

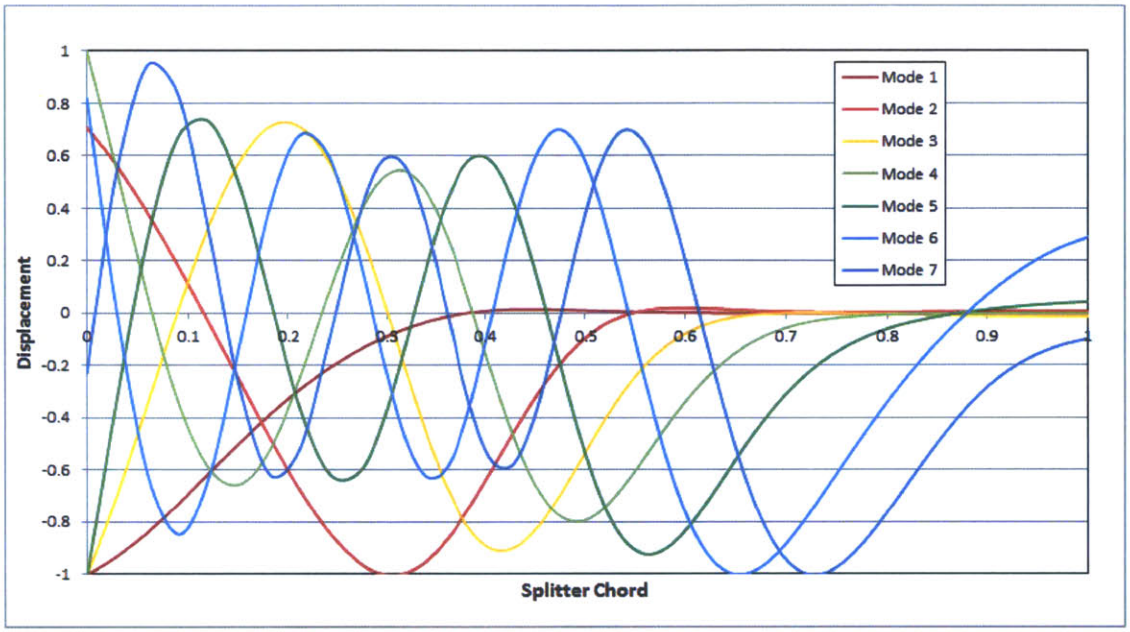

Figure 3-3: Modal displacement of the splitter blade tip for splitter blade modes 1 through 7.

For modal analysis using the second set of boundary conditions, a phase lag or "cyclic symmetry" boundary condition is applied to the cut surfaces. Cyclic symmetry implies that a circumferential phase angle of nodal coupling between 0 and 180 degrees exists across the two cut surfaces depending on the nodal diameter of interest. Since this impeller is a single piece bladed-disk, the impeller disk modes of interest are characterized by a nodal diameter pattern. For a rotating disk, these disk modes may remain stationary relative to the disk or travel forward and backward circumferentially around the disk. Since disk mode shapes are not necessarily fixed to the geometry of the impeller, a convenient way to represent the eigenvectors of these modes is through the use of complex numbers which allow the mode shape to have both spatially varying magnitude and phase.

The relationship between the sector model, phase lag of the cyclic symmetry boundary condition, and nodal diameter begins with the sector of a full disk chosen to be modeled. For a full disk comprised of N sectors, the sector angle, or wedge angle, is simply[17],

$$\alpha = \frac{2\pi}{N} \tag{3.5}$$

The nodal diameters, or harmonic indexes, that this sector model can support with the same number of blades per sector are

$$d = 0, 1, 2, ... \begin{cases} \frac{N}{2}, & \text{if } N \text{ is even} \\ \frac{N-1}{2}, & \text{if } N \text{ is odd} \end{cases} \tag{3.6}$$

The inter blade phase angle ($IBPA$) is then the relative circumferential phase angle between adjacent blades for a particular nodal diameter and is described as,

$$IBPA = d\alpha = \frac{2\pi}{N} d \tag{3.7}$$

To find the IBPA associated with the diffuser/rev excitation, one would choose the harmonic index (nodal diameter) equal to,

$$d_d = min(N_d - cN) \text{ for } c = 0, 1, 2, ... \tag{3.8}$$

making the IBPA associated with the diffuser excitation,

$$IBPA_d = \frac{2\pi}{N} d_d \tag{3.9}$$

Impeller Natural Modes of Vibration

Figure 3-4 shows the modal tip displacement of splitter modes 5 and 6 normalized to a maximum value of one for the two boundary conditions considered: fixed and cyclic symmetry. The cyclic symmetry boundary condition shown has an $IBPA$ of $IBPA_d$ radians associated with the diffuser engine order. For both sets of boundary conditions, note the airfoil mode's appearance of a spatial wavelength along the chord of the airfoil. These edgewise modes are like chordwise or stripe modes on blades in axial stages and can be approximated as fundamental rectangular plate modes. Blevins [2] shows that a flat plate fixed on one side with all other edges being free

has natural frequencies described as

$$f_{ij} = \frac{{\lambda_{ij}}^2}{2\pi\sqrt{12(1-\nu^2)}}\sqrt{\frac{E}{\rho}}\frac{t}{L^2} \tag{3.10}$$

where L can be thought of as the span of the blade, ν is Poisson's ratio, ρ is the mass density, t is the blade thickness, E is Young's modulus, and λ_{ij} is a tabulated constant which is a function of the number of half waves in the spanwise direction i, half waves in the chordwise direction j, and aspect ratio. From Equation 3.10 it can be expected that changes to the blade thickness will directly scale the frequency of a particular mode at constant span and chord. Splitter modes 5 and 6 are both considered airfoil edgewise modes which, because they are of the same family, cannot be tuned independently of one another on the Campbell diagram by changes in the airfoil thickness.

The vibratory motion of the backwall can be approximated like a thin annular plate with a clamped annulus. Blevins [2] shows that the natural frequencies of this annular plate are described as

$$f_{ij} = \frac{{\lambda_{ij}}^2}{2\pi\sqrt{12(1-\nu^2)}}\sqrt{\frac{E}{\rho}}\frac{h}{R^2} \tag{3.11}$$

where R can be thought of as the exducer radius of the disk, ν is Poisson's ratio, ρ is the mass density, h is the backwall thickness, E is Young's modulus, and λ_{ij} is a tabulated constant which is a function of the number of nodal diameters i, nodal circles j, and r/R where r is the inner radius where the annular plate is clamped. From Equation 3.11 it can be expected that changes to the backwall thickness will directly scale the frequency of a particular mode at constant exducer radius.

Backwall modes are generally unlike blade modes in that the mode shape nodal lines are not fixed in space and can therefore take on the motion of a traveling wave either in or against the direction of rotation. Figure 3-5 illustrates a simple schematic of the backwall, or disk, mode shape. The disk mode resonance of interest occurs when a structural wave travels against the direction of rotation such that the zones of deflection into and out of the page appear stationary to a stationary

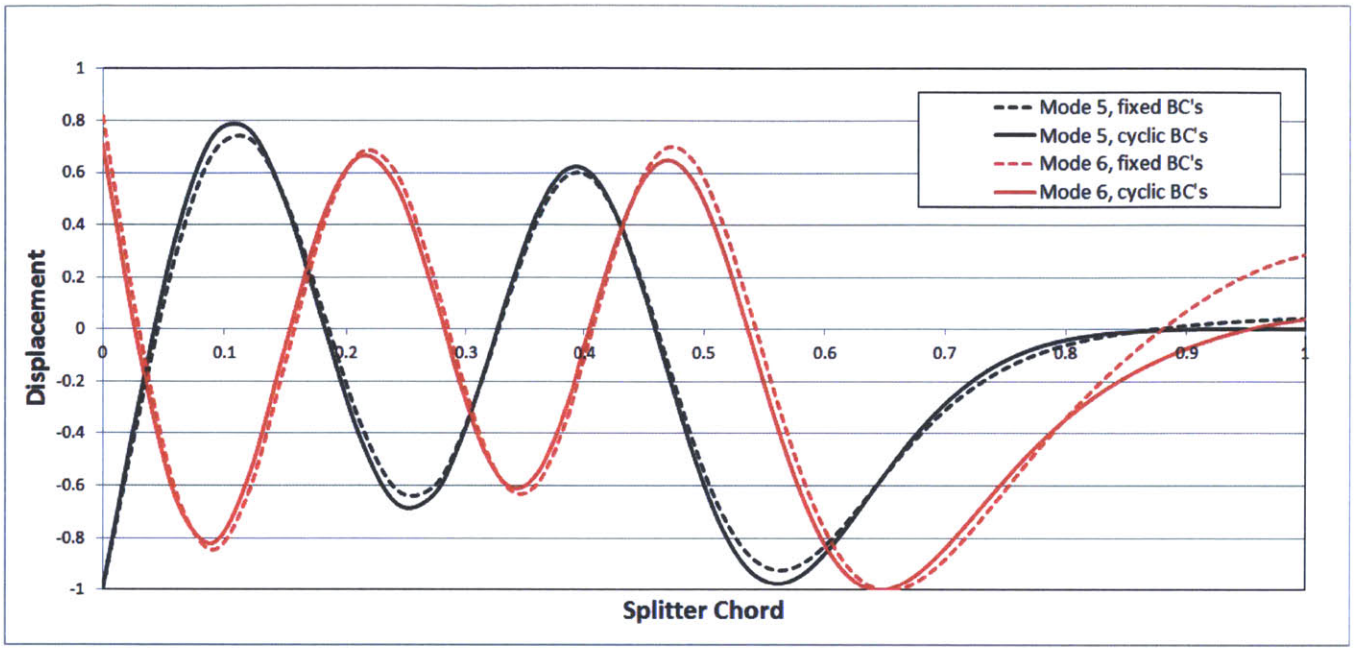

Figure 3-4: Normalized tip displacement using both fixed and cyclic symmetry boundary conditions for splitter mode shapes 5 and 6. Note the variation in the mode shape of splitter mode 6 near the trailing edge for the two sets of boundary conditions.

observer. Figure 3-6 illustrates the condition of an X/rev excitation exciting an X nodal diameter backwall mode, where X is a positive integer. Such a condition implies that the time it takes the rotor to rotate $360/X$ degrees is the same as the period of the backwall mode's frequency. Since the maximum and minimum deflection points remain stationary to the excitation (but not stationary relative to a point on the rotating disk) a form of resonance occurs, commonly referred to as a Campbell major resonance [22].

Modal Coupling

Since the impeller is a bladed-disk design, a single mode shape comprises the entire structure including the blades and backwall. However, for some natural modes the behavior of local regions of the impeller, such as the splitter blade, can exhibit mode shapes and frequencies nearly identical to the frequency and mode shape of a blade alone fixed in space along the hub. These impeller modes are said to be the blade dominant modes as the modal displacement is dominantly from the splitter blade.

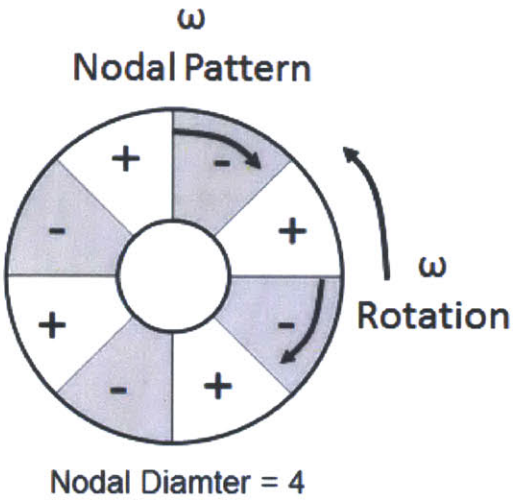

Figure 3-5: Schematic of a 4^{th} nodal diameter disk mode for a disk with a hole in the center showing motion into the page (-) and out of the page (+) in a backward traveling wave excitation.

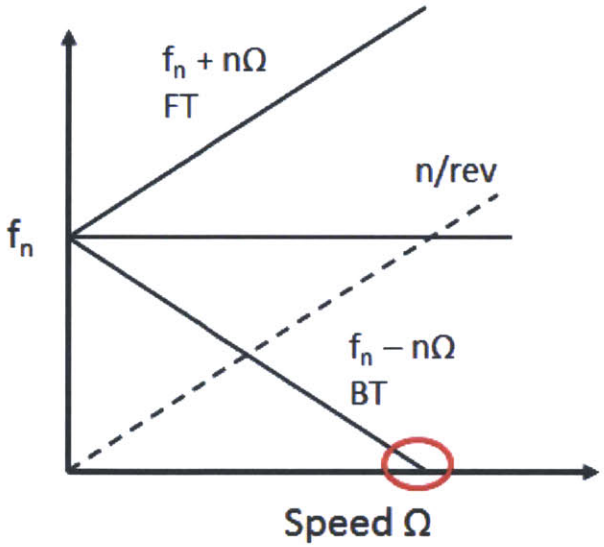

Figure 3-6: Apparent frequency of a backward traveling (BT) and forward traveling (FT) vibratory wave pattern to a stationary observer. The red oval indicates the speed at which a stationary observer sees no vibratory frequency as a result of a BT vibration wave.

Similarly, some modes can exist as disk dominant modes; however, some motion of the airfoils must be expected due to the physical coupling the disk makes with the blades. Figure 3-7 shows side views of three typical impeller mode shapes: blade dominant mode, backwall dominant mode, and blade-backwall mode coupling. For backwall dominant modes, note the modal displacement of the impeller blades at the trailing edge due to the backwall motion but not along the splitter or main blade chords. For blade backwall coupling modes, motion of both the airfoil and disk can be seen. The phenomenon at which blade and disk modes appear to couple is succinctly described in the AGARD Manual on Aeroelasticity [19]:

> Flexible disk natural mode shapes are characterized by lines of zero motion across the diameter called nodal diameters. These may couple with the blade natural modes to produce system modes with elements of motion of each component's natural mode but at a new frequency.

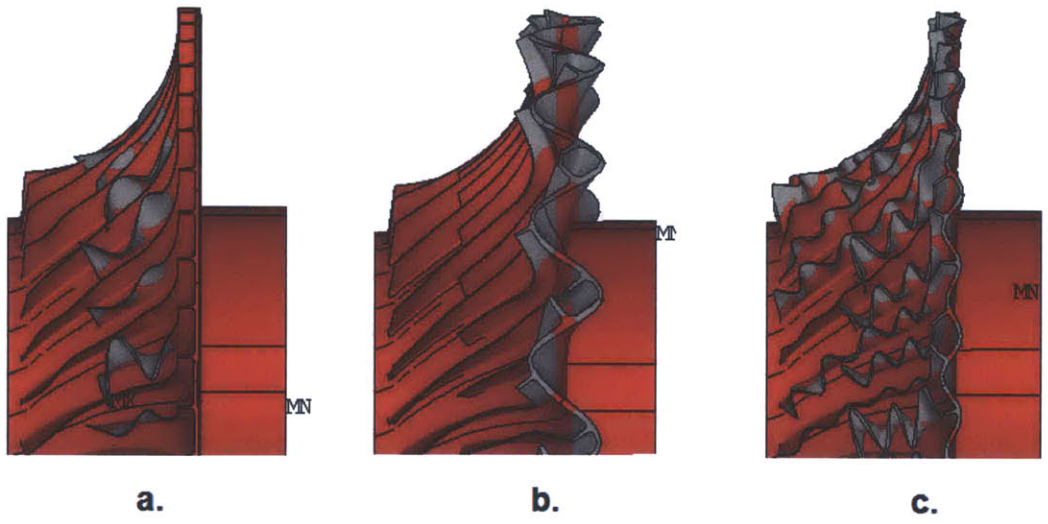

Figure 3-7: Representative impeller mode shapes: a.) splitter blade dominant mode, b.) backwall dominant, c.) splitter blade-backwall coupling in vicinity of a veering point.

The coupling of modes may impact the forced response of the splitter blade by locally changing the mode shape. To identify potential coupling of splitter and backwall

dominant mode families in the operating range, a SAFE diagram is used.

3.2.2 Simplified SAFE Diagram

Figure 3-8 shows the centrifugal impeller's Campbell diagram, repeated here for convenience. The Campbell diagram is an effective tool for identifying the forcing frequency that matches with natural frequencies of the structure. The Campbell diagram, however, does not include any information about the shape of the forcing function relative to the mode shape of vibration. Two key aspects of the mode shape to consider are: 1) a single blade's mode shape relative to the chordwise spatial distribution of the forcing function; and 2) the inter blade phase angle of the mode shape relative to the inter blade phase angle of the excitation. The first consideration highlighted sets the chordwise matching of the forcing function with the mode shape and, to the author's knowledge, no diagram exists to identify this spatial matching condition. The second consideration highlighted sets the matching of the forcing function blade-to-blade circumferentially and is identified through the use of a SAFE diagram.

Figure 3-9 is the SAFE diagram for the impeller showing splitter modes 1 through 7 and the backwall mode frequencies as a function of the inter blade phase angle. Main blade modes and other modes of the impeller have been omitted for clarity. The two inset boxes of Figure 3-9 show closeups of all modes in the vicinity of the blade-backwall veering points for splitter modes 5 and 6. The SAFE diagram plots frequency against nodal diameter or inter blade phase angle with the relationship given in Equation 3.7. The black boxes represent a known excitation on the stage with the bottom and top of the boxes representing the frequency of that excitation at idle and maximum speeds, respectively. Note the close proximity of splitter mode 6, the diffuser/rev excitation and the backwall modes. In addition to highlighting whether a known excitation will excite a mode with a particular nodal diameter, the SAFE diagram also serves to identify where backwall modes may begin to interact with the blade modes. The zigzag appearance of the backwall modes on the SAFE diagram is a result of the engine order excitation greater than N/2.

As stated before, the constructed simplified SAFE diagram in Figure 3-9 does

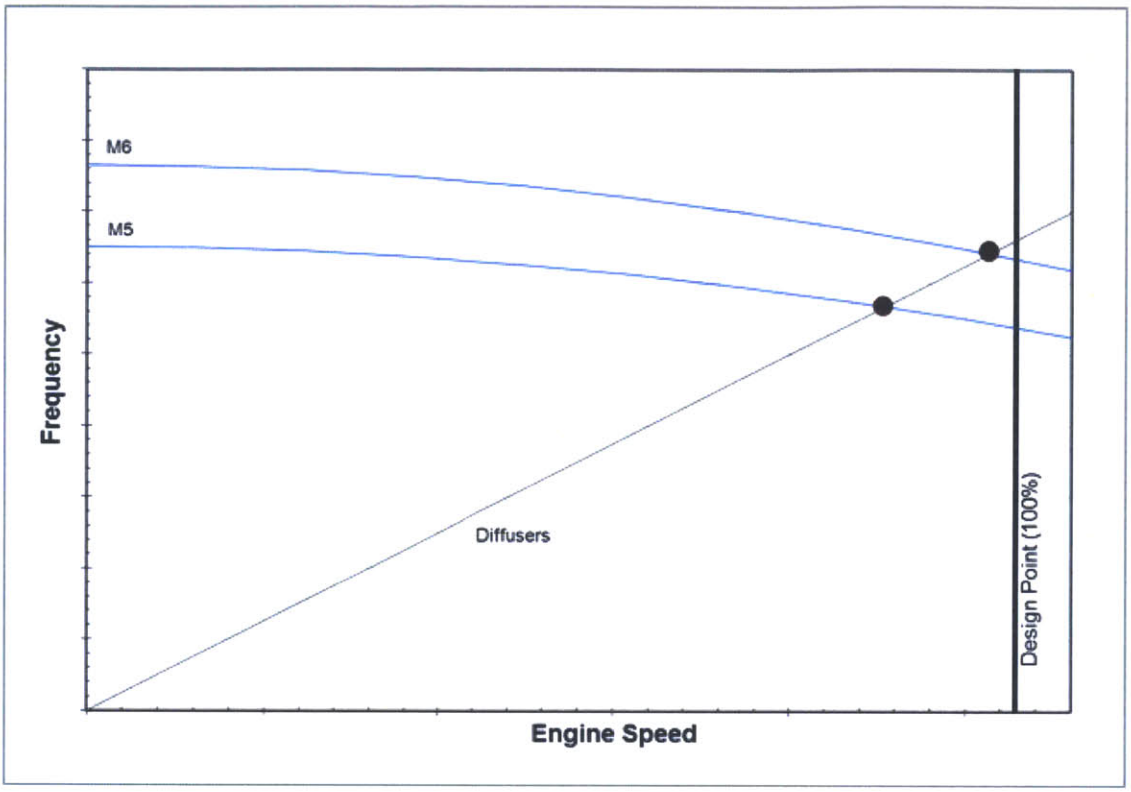

Figure 3-8: Splitter blade Campbell diagram showing edgewise modes 5 and 6.

not contain all modes in the frequency range shown. The modes represented in the simplified SAFE diagram exhibit motion either dominant to the splitter blade or the backwall. The impeller mode shapes are screened visually to determine what family the mode shape belongs to (e.g. splitter, main, backwall). In regions where these modes appear to intersect on the SAFE diagram, and modal displacement is present in both the airfoils and backwall, the location of the maximum modal deflection point is used to categorize the mode as blade or backwall dominant. The frequencies of these chosen modes are then plotted against nodal diameter and connected with straight lines to highlight regions of potential blade-backwall coupling. In actuality, these discrete modes may never cross; instead, these modes seemingly veer away from one another in the nodal diameter space [15]. The rate, or local curvature, at which the modes veer away has been shown to physically reflect the degree of modal coupling present between the modes [1]. The SAFE diagram in 1-5 does not show the true veering behavior of the impeller modes but is an adequate tool for identifying modes

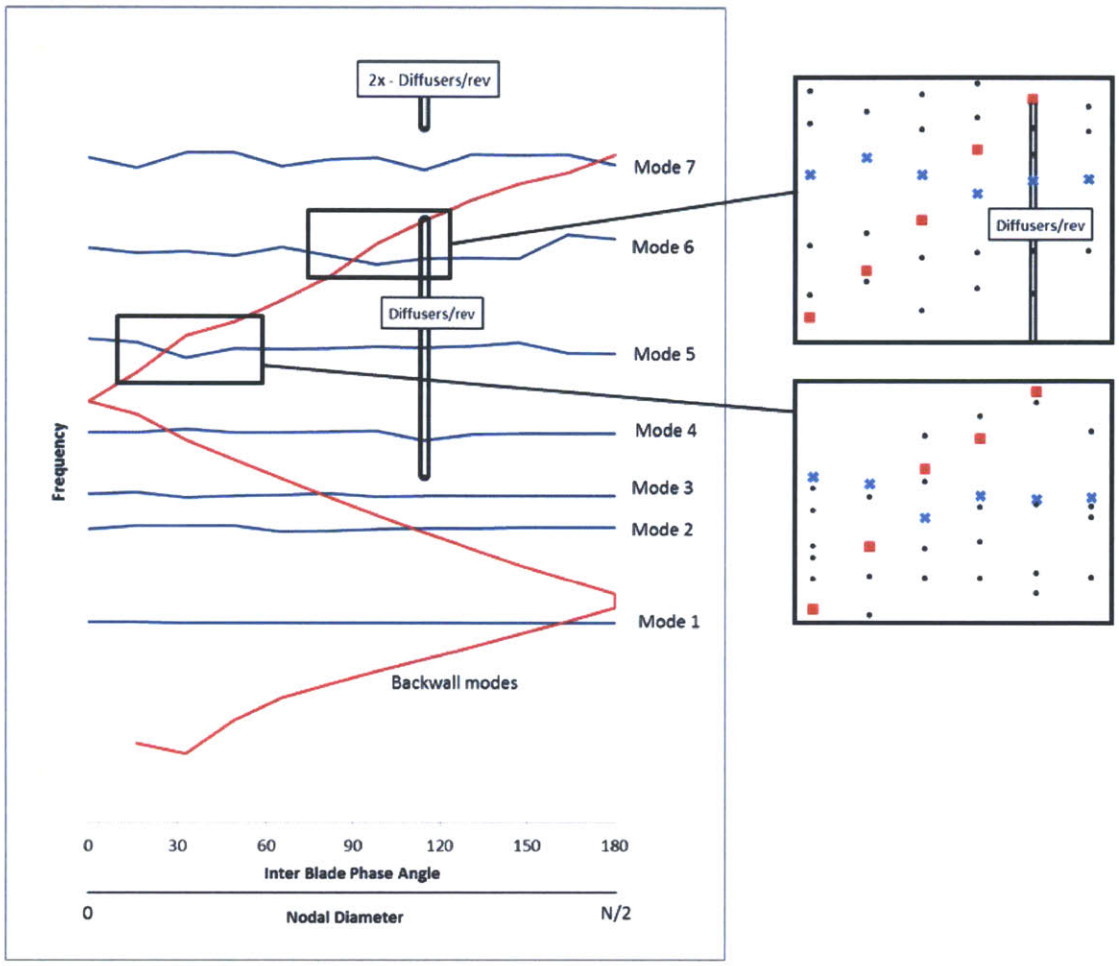

Figure 3-9: Simplified SAFE diagram of the splitter blade and backwall modes showing closeups of all modes in vicinity of the blade-backwall crossings for splitter modes 5 and 6. Red squares are backwall dominant modes, blue X's are splitter blade dominant modes and black dots are other modes of the impeller including main blade modes.

which may exhibit modal coupling; therefore, it is referred to as a "simplified SAFE diagram." The effect modal coupling has on the forced response will be shown in Chapter 4 and the results will be used to illustrate the utility of the SAFE diagram as a screening tool.

Although a bladed-disk may be limited to $N/2$ nodal diameters, a disk without discrete circumferential features has an infinite number of nodal diameters possible and this behavior is present in higher-order backwall dominant modes of the impeller. If the engine order of the excitation is greater than $N/2$, the excitation can excite

backwall modes with countable nodal diameters equal to the engine order or a nodal diameter, d, between 0 and $N/2$ by,

$$EO = cN \pm d \text{ for } c = 0, 1, 2, ... \tag{3.12}$$

The SAFE diagram indicates a spatial matching of the forcing function and structure in the circumferential direction. Since energy of the unsteady pressure field enters the structure through the vibrating blades, an effective transfer of energy occurs when the blades vibrate with an inter blade phase angle consistent with the circumferential distribution of the forcing function. If the excitation and mode shape do not cross on the SAFE diagram, the implication is that the vibration of some blades may actually be doing work on the unsteady pressure field which reduces the overall strength of the modal force.

The spatial matching identified by the SAFE diagram is for the full wheel and does not indicate the chordwise correlation of the forcing function and mode shape. It is hypothesized that even if the forcing frequency and engine order match the frequency and nodal diameter of the vibratory mode, the response can be mitigated if the acoustic wave traveling over the surface of the impeller is not effectively correlated to the vibratory mode shape.

3.2.3 Assessment of Computational Model

The structural FEM sector model of the centrifugal impeller was provided. The provided temperature distribution and steady-state loads are assumed to be acceptable representations of the conditions at the maximum speed [21]. At its current refinement, 22 thousand elements and 27 thousand nodes, the model gives acceptable computation of the steady-state stress state and vibratory modes of the physical impeller. It has been demonstrated that the model is accurate to within 5% of the actual impeller at room and operating conditions [21]. Vibratory modes are found using this FEM model at both "bench" (room temperature, zero speed) conditions and operating conditions. The crossing speed and frequency that a structural mode

makes with a particular engine order excitation on the Campbell diagram is found by extrapolating between the two modeled conditions with a previously determined fitting scheme. This model represents the average geometry of the centrifugal compressor stage considering the machining tolerances. In general the FEM model is quite representative of the actual impeller; however, as this study focuses on the physical mechanisms which set the forced response, absolute values are less important than the trends given by the model.

3.2.4 Physical Attributes of the Mode Shape Critical to a Forced Response

The unsteady loading arises from the unsteady pressure on the splitter blade surface. From Equation 3.3 (which is used to compute the modal force) it is clear that the dot product of the modal force is minimized when the modal displacement and the surface normal are orthogonal and maximized when aligned. Both the unsteady pressure field and the mode shape vary along the splitter blade chord in magnitude. As a result, the modal work performed on the splitter blade will not only be enhanced when the mode shape and surface normal are aligned, but also when high amplitude loading acts on regions of high modal displacement. If either of these conditions are not met, the work done on the structure will be less than the maximum achievable. In Figure 1-6 note the modal displacement of the trailing edge of mode 6 versus mode 5. If the unsteady pressure field is highest at the trailing edge, any modal displacement in this region will allow the structure to gain energy and vibrate at a higher amplitude.

Vibratory modes 5 and 6 of the splitter blade clearly have a structural wavelength present in the mode shape, seen in Figure 1-6. However, unlike the Bernoulli-Euler beam, this wavelength varies along the chord. Longer wavelengths appear near the trailing edge as the blade span is shortest in this location, causing the stiffness of the blade in the transverse direction to be at its highest. The approximation of the structural wavelength comes from the identification of peaks, troughs, and zeros in the mode shape. The zeros represent nodal line locations of the mode shape, which

are indicative of the apparent standing vibratory motion of the splitter blade.

Since the mode shape can be represented as a complex number it can have both standing and traveling components to it such that a phase difference may exist from the splitter leading edge to the trailing edge. FEM modal analysis using cyclic symmetry boundary conditions provides two eigenvectors for each eigenfrequency found. For eigenvectors ϕ_A and ϕ_B of the repeated eigenfrequency ω the magnitude and phase of the mode shape are, respectively,

$$|\phi| = \sqrt{\phi_A^2 + \phi_B^2} \tag{3.13}$$

$$\Phi = arctan\left(\frac{\phi_A}{\phi_B}\right) \tag{3.14}$$

Figure 3-10 highlights the variations in phase of the splitter blade modes along the chord of the airfoil. The phase is generally constant along much of the airfoil except near the trailing edge where the phase difference from inducer to exducer is nearly 90 degrees.

From the study of the forced response of a Bernoulli-Euler beam, it is hypothesized that the important characteristics of the mode shape that may impact the forced response are: 1) the presence of modal displacement at the trailing edge; 2) the appearance of structural wavelengths which give the mode shape a wavelike spatial distribution in the chordwise direction, and; 3) phase difference in the modal displacement from leading edge to trailing edge.

3.3 Forcing Function Model: Unsteady CFD Flow Field Description

The unsteady loading acting on the splitter blade in the centrifugal compressor stage is calculated numerically using CFD methods. The CFD model solves for the time-accurate flow conditions in both the impeller and diffuser and has shown good agreement to measurements on a rig test.

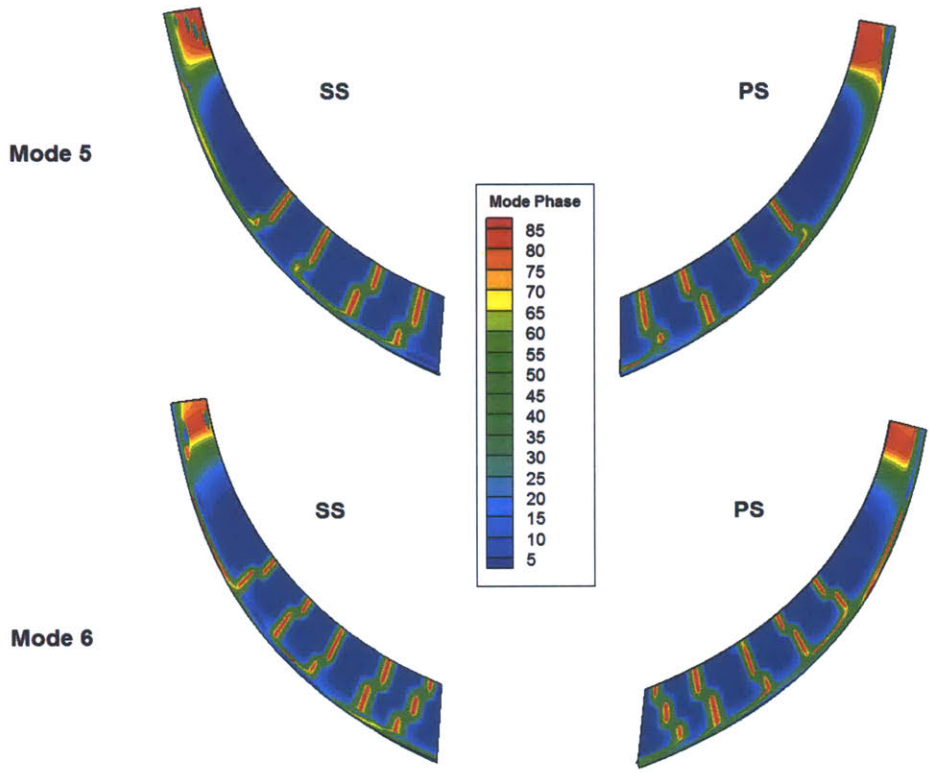

Figure 3-10: Phase of splitter mode shape for modes 5 and 6 at IBPA associated with diffuser excitation.

3.3.1 Description of Model

The CFD model of the centrifugal compressor stage was originally formulated by Gould [9] in CFX 5.7.1 and was updated for implementation in CFX 13.0. The model consists of a domain enclosing a sector of the impeller rotor and diffuser as shown in Figure 3-12. As the sector cut surfaces of the CFD model are coupled (phase lag of zero), an appropriate number of impeller blades and diffuser passages is chosen to capture the appropriate passage-to-passage variation in the impeller flow due to the circumferential spacing of the diffuser passages. The back pressure at the exit of the diffuser is iterated upon until the desired mass flow rate is achieved. Computed unsteady flow solutions were obtained at the design point for both standard temper-

ature and pressure (STP) inlet conditions and stage inlet conditions at the operating point. Additionally, computed flows were obtained off design on the nominal operating line for splitter mode 5 and 6 crossings with the diffuser engine order. The time step of the numerical analysis is chosen based on the stage characteristic time period, τ, which is the period of the blade passing frequency. The unsteady solver uses a 2^{nd} order Backward Euler scheme with a shear stress transport (SST) turbulence model.

The unsteady static pressure on the surface of the splitter blade can be cast in terms of a magnitude and phase at the diffuser vane passing frequency. Figure 3-13 shows the magnitude and phase information of the power spectrum (computed using a Fast Fourier Transform, or FFT) for the unsteady static pressures calculated at design point with STP inlet conditions. The peak magnitude of the static pressure occurs near the trailing edge on the pressure side and decays toward the leading edge. The phase plot of the static pressure distribution exhibits a classic traveling wave shape characterized by the repeating bands of equal phase.

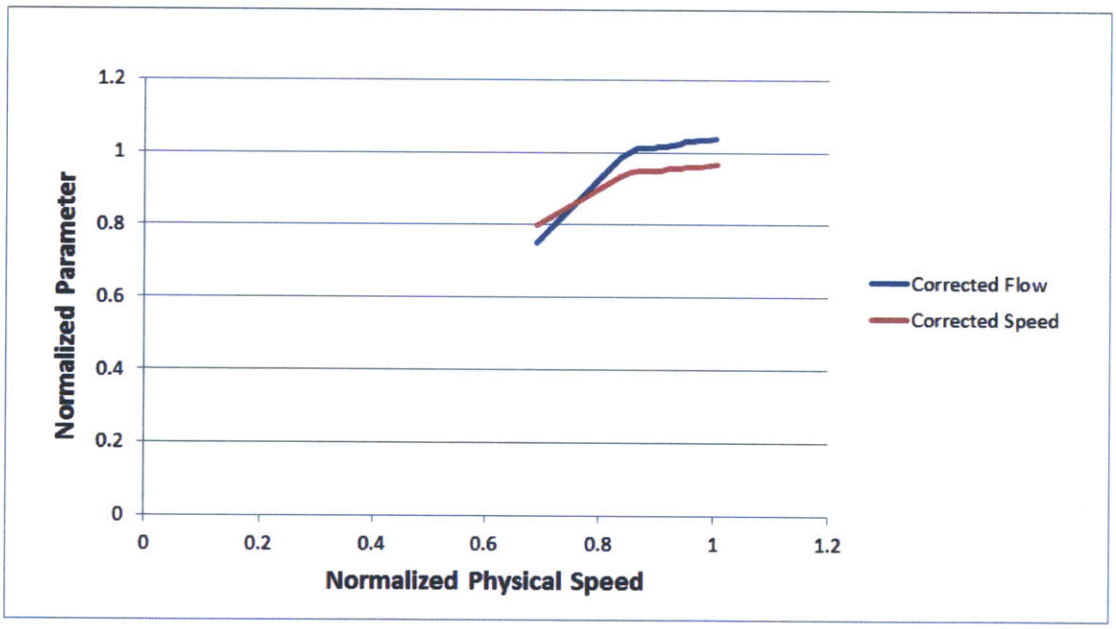

Figure 3-11: Centrifugal corrected conditions vs. engine physical speed, adopted from [9].

The unsteady CFD results are further used to calculate the unsteady loading acting on the splitter blade, defined by

Figure 3-12: Schematic of the research centrifugal compressor stage CFD domain, adopted from Gould [9].

$$\Delta P_s = \frac{P_{PS} - P_{SS}}{q} \tag{3.15}$$

where P_{PS} and P_{SS} represent the static pressure on the pressure and suction sides of the splitter blade respectively. The normalizing parameter is q, the exducer dynamic head or dynamic pressure, defined as

$$q = 1/2\rho_1 U^2_{exducer} \tag{3.16}$$

where U is the tip speed at the exducer radius and ρ_1 is the stage inlet density at the operating condition. Figure 3-14 shows the time-accurate loading on the splitter blade midspan and tip normalized by exducer dynamic head for the design point, mode 6 crossing, and mode 5 crossing at stage inlet conditions. In these plots the envelope of the unsteady loading across the splitter blade chord shows that the upstream extent of the unsteadiness is comparable. Figure 3-15 shows the maximum blade loading over two characteristic time periods on the splitter blade tip and

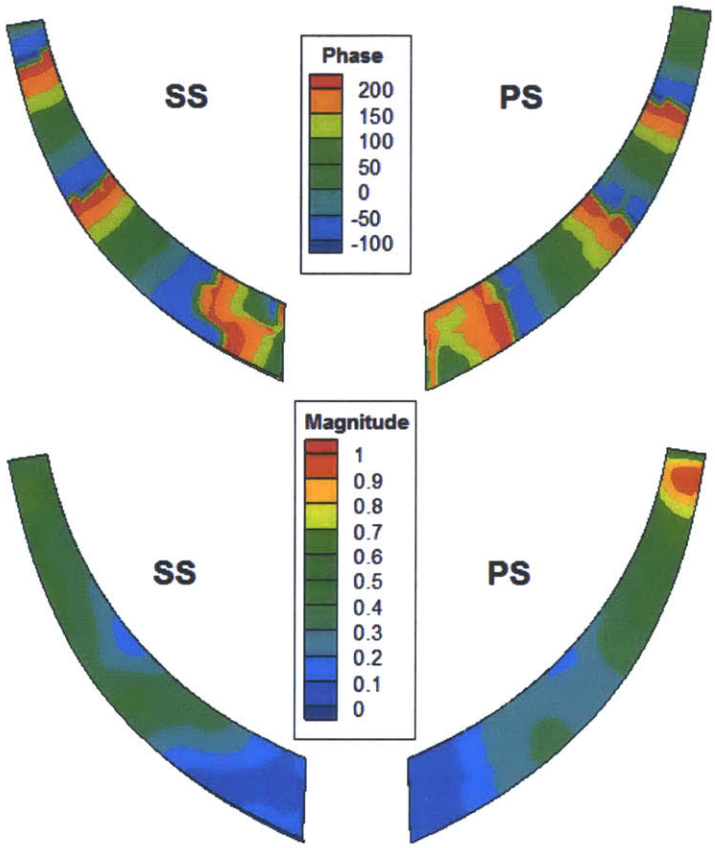

Figure 3-13: Magnitude and phase of splitter blade surface static pressure at design point with inlet STP inlet corrected conditions, magnitude normalized by maximum value.

midspan for the operating speeds and inlet conditions computed. Both plots show the maximum blade loading normalized by the exducer dynamic head as a function of percent corrected speed of the design point. The 100% corrected speed condition has a peak tip loading value of about 0.6. The peak loading occurs at about 95% chord which is consistent with other centrifugal stages assessed by Lusardi [14]. As defined by Gould [9], the loading fluctuation is the instantaneous amplitude of the unsteady loading averaged over a characteristic period

$$\Delta L = \Delta P_{s_{max,\tau}} - \Delta P_{s_{max,\tau}} \tag{3.17}$$

Figure 3-17 shows that the loading fluctuation also appears to scale with exducer

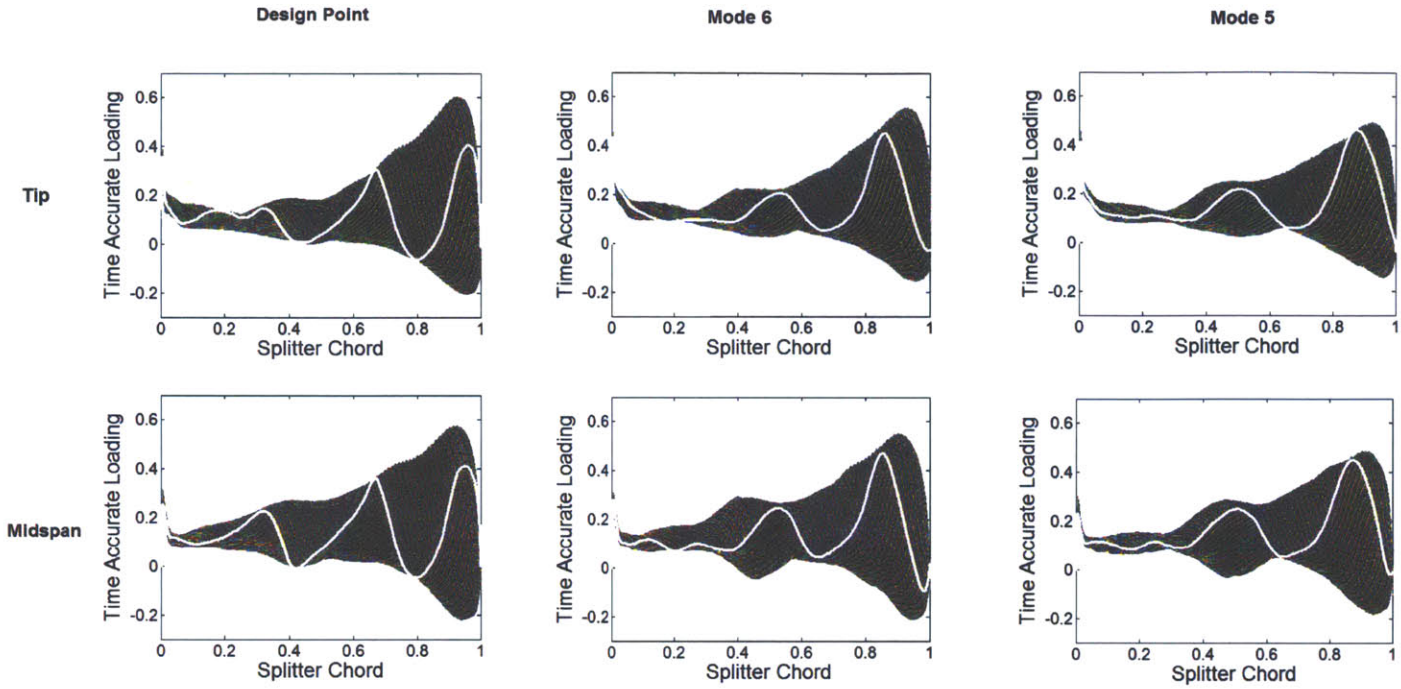

Figure 3-14: Time-accurate loading on the splitter blade normalized by exducer dynamic head for the design point, mode 6 crossing, and mode 5 crossing at stage inlet conditions.

dynamic head and decay from the trailing edge to the leading edge. The loading fluctuation is a measure of the forcing function amplitude along the chord of the airfoil which is highest at the trailing edge. As the corrected speed decreases the loading fluctuation decreases except near 50% chord where there is a reversal in this trend. Since the loading fluctuation scales with exducer dynamic head the strength of the unsteady loading acting on a vibrating impeller blade increases with physical speed.

The corrected speed and mass flow are both expressed as functions of the inlet total temperature, T_{STP}, and pressure, P_{STP}, at STP inlet conditions [8]

$$N_{corr} = \frac{N_{phy}}{\sqrt{\Theta_1}} \tag{3.18}$$

$$\dot{m}_{corr1} = \dot{m}_1 \frac{\sqrt{\Theta_1}}{\delta_1} \tag{3.19}$$

where Θ_1 and δ_1 are

$$\Theta_1 = \frac{T_{t1}}{T_{STP}} \tag{3.20}$$

$$\delta_1 = \frac{P_{t1}}{P_{STP}} \tag{3.21}$$

P_{t1}, T_{t1}, and $\dot{m}_1$ represent the total pressure, temperature and mass flow rate, respectively, at inlet conditions other than STP. Flow similarity is maintained for different inlet conditions when the corrected speed and mass flow remain constant. Figure 3-11 shows that the corrected conditions remain relatively constant near the design point despite the varying physical speed. The corrected speeds of modes 5 and 6 are quite similar at 97.5% and 99.4%, respectively, but the physical speeds have a much larger variation. By the similarity of flows at equal corrected conditions, it is hypothesized that the physical characteristics of the loading, such as amplitude and spatial distribution, will remain constant with corrected speed. Figure 3-16 shows that the splitter loading, as expected, is nearly identical at the design point when corrected speed and mass flow are maintained between STP inlet conditions and the stage inlet conditions at the operating point. It is important to note that the vibrations of structural components respond to EO excitation frequencies driven by the physical speed while the attributes of the unsteady loading are set by the corrected speed of the centrifugal stage.

3.3.2 Assessment of Computational Model Against Experimental Data

All numerical models, and especially CFD models, should be properly evaluated against known measurements, mesh refinement, convergence, and, for unsteady models, periodicity. Figure 3-18 shows the dominant frequency content (highest magni-

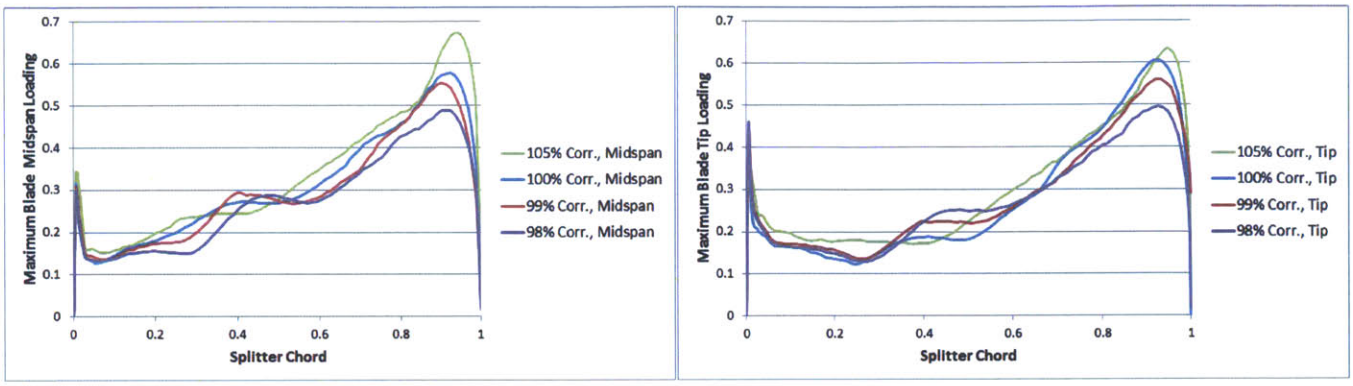

Figure 3-15: Maximum splitter blade loading at blade tip and midspan for the computed conditions assessed normalized by exducer dynamic head.

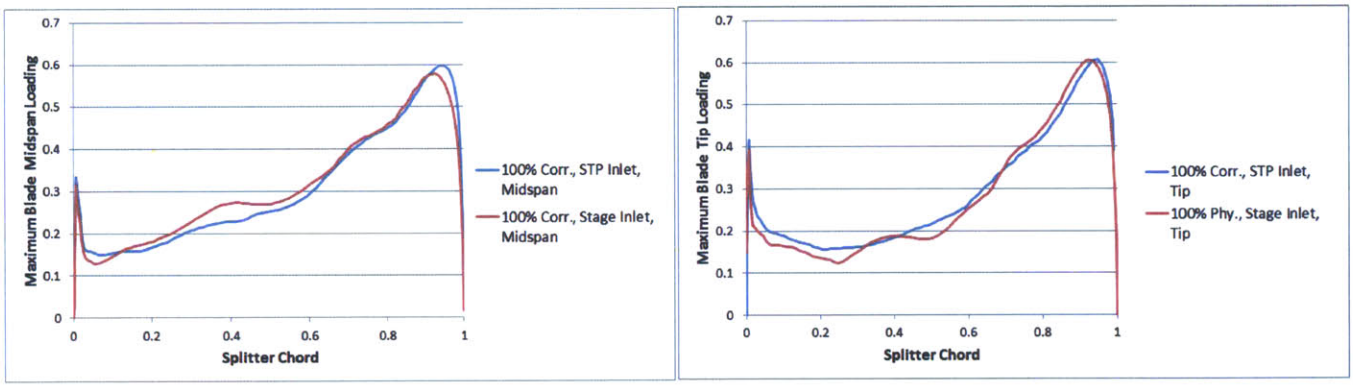

Figure 3-16: Comparison of maximum splitter blade loading at blade tip and midspan at the design point for STP inlet and stage inlet conditions normalized by exducer dynamic head.

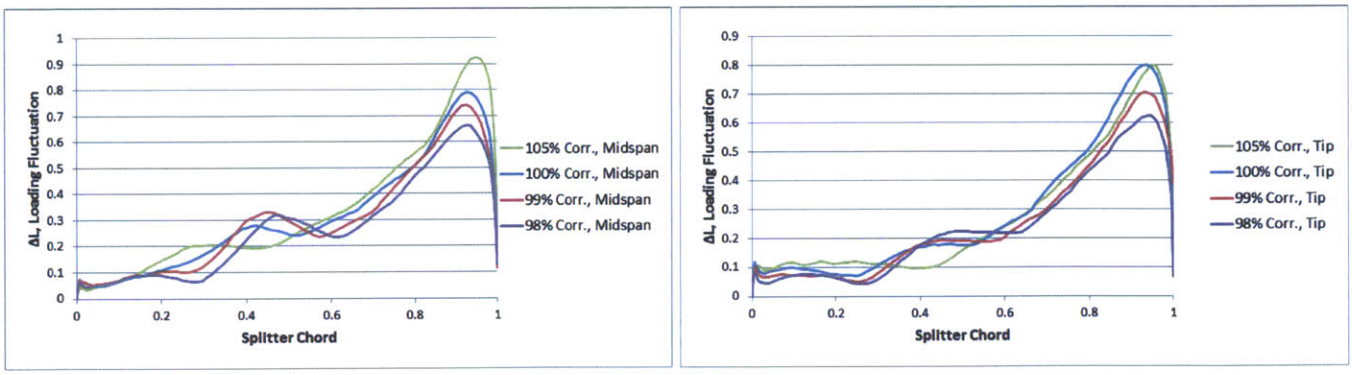

Figure 3-17: Splitter blade loading fluctuation at blade tip and midspan normalized by exducer dynamic head.

tude) of the unsteady pressure acting on the splitter blade. The plotted frequency is normalized against the expected diffuser vane passing frequency. Since other excita-

tion sources were not modeled explicitly, the plot shows that the dominant unsteady pressure acting on the splitter blade has the frequency content associated with the diffuser passing frequency as expected.

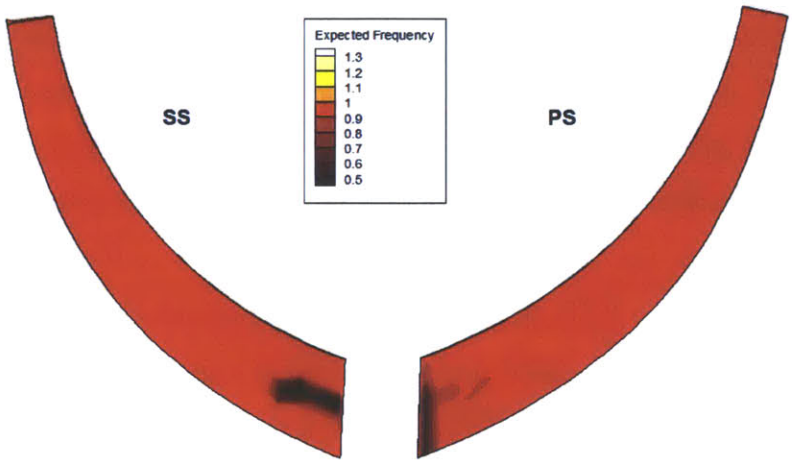

Figure 3-18: Highest magnitude frequency content on the splitter blade normalized by diffuser passing frequency from unsteady CFD at design point, STP inlet corrected conditions.

The CFD model has 3.7 million nodes and 2.2 millions elements in its current refinement. Gould performed detailed mesh refinement and timestep studies of this CFD model which is used to generate the unsteady loading on the splitter blade. He found that the medium grid captures the midspan and peak static pressure fluctuations, defined as

$$P_f = \frac{P_{max,\tau} - P_{min.\tau}}{1/2\rho_1 U_{tip}^2} \tag{3.22}$$

to be within less than 0.01 between the medium and fine grids for a timestep of $\tau/160$ [9]. $P_{min.\tau}$ and $P_{max.\tau}$ represent the maximum and minimum static pressures in one characteristic period. At any new operating point, the model is said to have converged when the residuals have dropped to less than 1E-3 and static pressure on the splitter blade is periodic in time. All timestep results over two characteristic periods are processed in the modal force calculation. Time averaged values of the

mass flow and total pressure agree to within 3% of the compressor map provided for the Campbell crossing speeds of mode 5 and mode 6 [9].

The research centrifugal compressor stage has been run both in full engine tests and rig tests. The rig is instrumented with high response Kulite pressure transducers to record unsteady static pressures in regions of interest. One Kulite exists in the impeller shroud near the exducer of the impeller. In the time domain, the signals from this Kulite and the CFD have a similar appearance in that they both capture the rise in static pressure due to an approaching impeller blade, followed by a sharp drop in pressure with the passing of the blade. The time averaged static pressure between the rig and the CFD model varies by 7.7% at this location. Figure 3-19 compares the FFT of the recorded unsteady pressure signal of the CFD model with the impeller shroud Kulite measurement on the rig. The plotted magnitude has been normalized by exducer dynamic head. Frequencies have been normalized by the expected impeller blade passing frequency at the particular operating point. The magnitude of the unsteadiness is 17.1% lower in the CFD model than the rig data while the frequency content of both data sets captures the expected blade passing frequency to within 1%. Both the CFD model and rig results indicate the presence of harmonics at multiples of the blade passing frequency.

Kulites in the discrete passages of the diffuser are used to evaluate the phase of the CFD and rig data signals. One Kulite near the throat of the diffuser passage exhibited high variation to the CFD model with the magnitude varying by a factor of 3.5. The variation between the CFD and rig measurement in this location is potentially due to a leading edge shock at the inlet of the diffuser throat at the operating point assessed. The presence of this shock induces a strong gradient in pressure in the vicinity of the Kulite which may explain the variation between the CFD and rig measurement at this location. The Kulite downstream of the diffuser throat has a variation of 28% in unsteady amplitude between CFD and the rig while the frequency content of both locations is within 1% of the expected blade passing frequency. The resulting phase difference between these two locations indicates a discrepancy of 14.5% between the CFD and rig data.

Despite the shortcomings of the CFD model in exactly matching the rig model, the results are consistent enough for this study of the splitter blade's forced response at resonance for a couple of reasons. First, the unsteady blade loading generated by this CFD model is consistent in amplitude, spatial distribution and upstream extent with blade loadings calculated on other centrifugal stages with other CFD solvers (namely that of Lusardi [14]). Secondly, the forcing function found exhibits physical characteristics (e.g. an acoustic wavelength, spatially distributed traveling loading, maximum loading near the trailing edge) which influence the modal force calculation but do not substantially vary its accuracy. As with the FEM model, the absolute values computed are less important than the trends arising from the model.

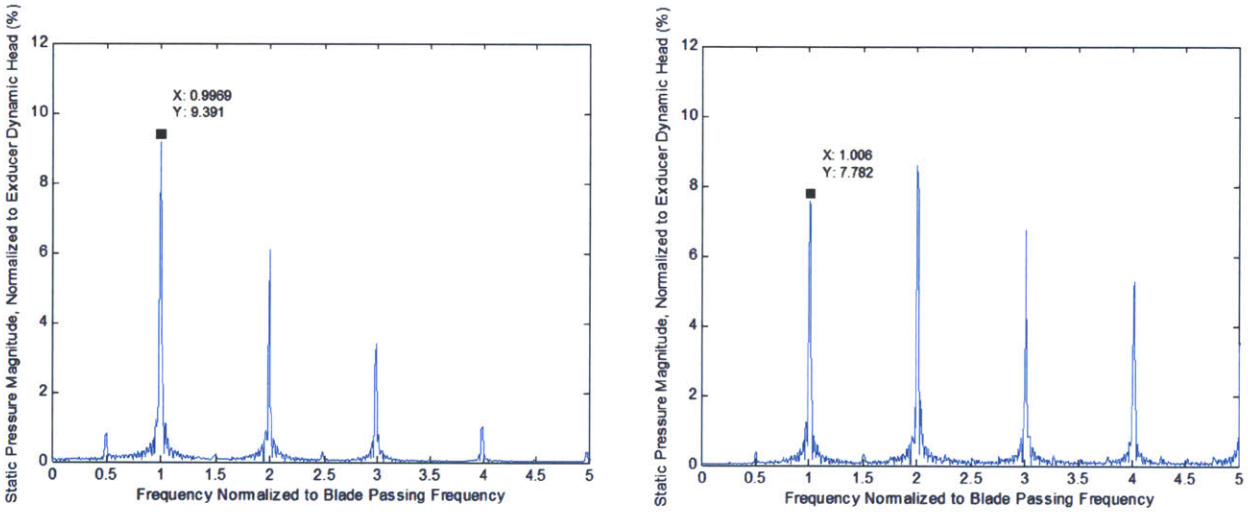

Figure 3-19: FFT comparison of impeller shroud kulite location from CFX CFD (right) and rig data (left).

3.3.3 Physical Attributes of the Flow Field Critical to a Forced Response

From Equation 3.3 (which is used to compute the modal force) the modal force is maximized when the modal displacement is aligned with the unsteady pressure acting normal to the blade surface. Figure 3-4 shows that mode 6 exhibits modal displace-

ment near the trailing edge which is near the chordwise location of the maximum unsteady loading shown in Figure 3-15. This unsteady loading also extends upstream to regions of higher modal displacement. For mode 5, which has relatively little modal displacement at the trailing edge, modal work can only be done at chordwise locations away from the highest unsteadiness. Figure 3-15 also shows that the unsteady loading scales with exducer dynamic head. For higher physical speeds, the amplitude of the unsteady static pressure on the surface of the splitter will increase with the tip speed squared. From Equation 3.3 the modal force will scale directly with the unsteady pressure amplitude which will, consequently, directly scale the displacement amplitude of the blade's vibration. Since the unsteady pressure scales with the exducer dynamic head, the unsteady loading acting on the splitter blade will be stronger at high speed Campbell crossings as more unsteady energy is present in the system.

To summarize, the unsteady flow field is hypothesized to have three characteristic features which contribute to the forced response of the splitter blade: 1) the spatial distribution of the unsteady traveling wave loading has a characteristic acoustic wavelength in the chordwise direction; 2) the extent of the upstream unsteadiness extends into regions of high modal displacement, and; 3) the magnitude of the peak unsteadiness sets the overall level of vibratory energy present in the stage.

3.4 Forced Response Computational Models

Several computational models are explored to elicit physical mechanisms which set the forced response of the impeller. Figure 3-20 shows a flowchart summarizing the various FEM models that are assessed.

Model 1 is referred to as the baseline case as it uses unsteady CFD corrected to STP inlet conditions and fixed in space boundary conditions. The forced response of splitter mode 5 and 6 are computed against the same unsteady pressures scaled by exducer dynamic head to the respective crossings. By evaluating these modal responses against the same forcing function, the influence of loading fluctuation and acoustic wavelength can be discerned. The fixed in space boundary conditions isolate

the modal displacement of the blade from the disk by fixing the nodes on the cut surfaces of the sector.

Model 2 uses the same set of boundary conditions as Model 1 but uses unsteady CFD computed at the physical crossing speed of splitter mode 5 and 6 to the diffuser engine order excitation. The unsteady pressures computed are used without scaling by exducer dynamic head when computing the modal force.

Model 3 uses cyclic symmetry boundary conditions which introduce the potential influence of disk motion on the forced response of the splitter blades. The forcing function is also the unsteady CFD computed at the physical crossing speed of splitter mode 5 and 6 to the diffuser engine order excitation.

Models 4 and 5 are sensitivity studies of the forced response due to variations in the backwall and blade thickness, respectively. The boundary conditions are the cyclic symmetry boundary conditions. The forcing function is also the unsteady CFD computed at the physical crossing speed of splitter mode 5 and 6 to the diffuser engine order excitation.

All calculations are performed on the surface nodes of the splitter blade structural mesh. Appropriate normalization factors are applied during the calculation to adjust the mode shape normalization to the sector mass matrix instead of the full wheel mass matrix. Equations 3.3 and 3.1 are applied to the centrifugal compressor to calculate the modal force and the physical displacement of the splitter blade. Since the mode shape and unsteady pressure are expressed as a complex number, the absolute value of modal force is taken after the summation of the dot product at each surface node. For the models assessed only the modal work exerted on the splitter blade is considered. Modal work performed on the main blade is not computed as the splitter blade dominant modes being considered show little modal displacement in the main blades. For modes that contain both blade and backwall motion, the contribution of modal work from the unsteady pressure acting on the disk's hub flow path in the vicinity of the exducer is also not computed. Also, the unsteady CFD model domain does not include the backwall of the impeller disk so any modal work done by unsteady pressures here cannot be computed.

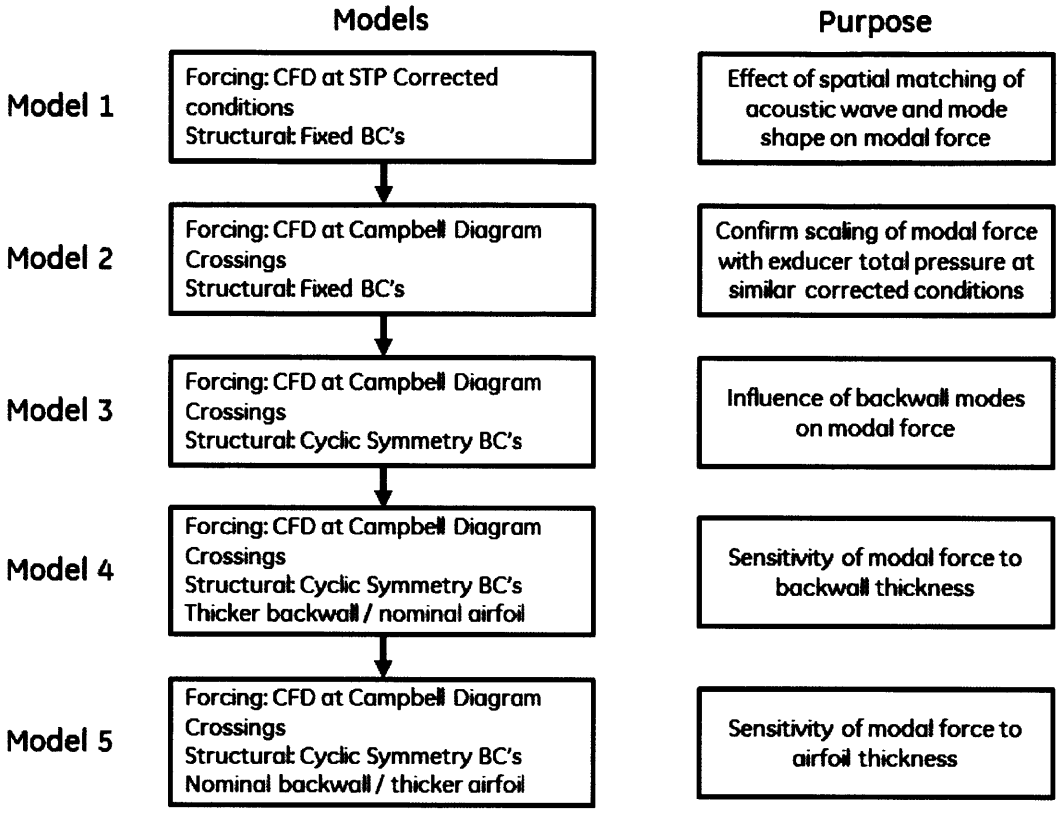

Figure 3-20: Flowchart of FEM models assessed and the purpose for each model.

3.5 Summary

The mode shape is derived from the FEM software ANSYS 14 for both cyclic symmetry and fixed in space boundary conditions. For this study, the sector model provided is assumed to be an acceptable model of the full impeller's natural modes of vibration. The unsteady pressure acting on the splitter blade is found using CFX 13. The unsteady pressures found from this model appear consistent with Kulite measured responses on a rig test with the same geometry. The refinement of the grid and appropriate timestep has been assessed by Gould [21] and is presented here for ease of reference.

Several models at different physical levels of approximation are utilized to determine the driving physical mechanisms that set the forced response of the centrifugal impeller. These various models assess the effect boundary conditions and geometri-

cal variations have on the calculation of modal force and the maximum response at resonance.

Chapter 4

Results: Physical Mechanisms Controlling the Forced Response

The findings of this thesis are focused on the physical mechanisms that set the forced response of an impeller blade as a result of the unsteady pressure field generated by the impeller-diffuser interaction. The mechanisms are identified through the use of several computational models that vary the structural boundary conditions and corrected flow conditions. These findings are enumerated below as,

1. Forcing frequency versus natural structural frequency:

   (a) facilitates narrow frequency band energy transfer when the forcing frequency and natural frequency are nearly equal, and

   (b) diminishes response when the forcing frequency is not equal to a natural frequency of the structure.

2. Forcing wavelength versus natural structural wavelength:

   (a) facilitates energy transfer where the spatial distribution of the unsteady loading and mode shape are well correlated, and

   (b) enhances response when the ratio of the forcing wavelength to the structural wavelength is between 0.5 and 1.5.

3. Physical speed of the crossing:

   (a) scales the loading fluctuation with exducer dynamic head for similar corrected conditions, and

   (b) increases the forced response risk of high speed crossings as the modal force scales with the magnitude of the loading fluctuation.

4. Modal displacement at the trailing edge:

   (a) enhances vibratory energy transferred to the structure as the unsteady loading is highest in the vicinity of the trailing edge, and

   (b) indicates potential blade-backwall mode coupling which alters the calculated modal work and forced response amplitude.

5. Blade-backwall mode placement:

   (a) reduces the impact general structural stiffening may have on mitigating the forced response if blade and backwall dominant modes begin to couple, and

   (b) increases sensitivity of the forced response to variations in geometry if blade and backwall dominant modes couple at a known excitation frequency.

Figure 4-1 shows how displacement amplitude of the forced response varies across the five models delineated in Figure 3-20. The absolute value of the computed displacement is not labeled, but the relative height of each column shows how the computed displacement varies between the models. The black bars show the sensitivity of the splitter blade's forced response over the domain of geometry variations assessed. The results shown in Figure 3-20 will be revisited as needed in the following sections.

4.1 Structural Wavelength Versus Acoustic Wavelength

The splitter blade mode shape exhibits a spatial distribution much like the acoustic wave propagating upstream along the surface of the blade. This structural waveform

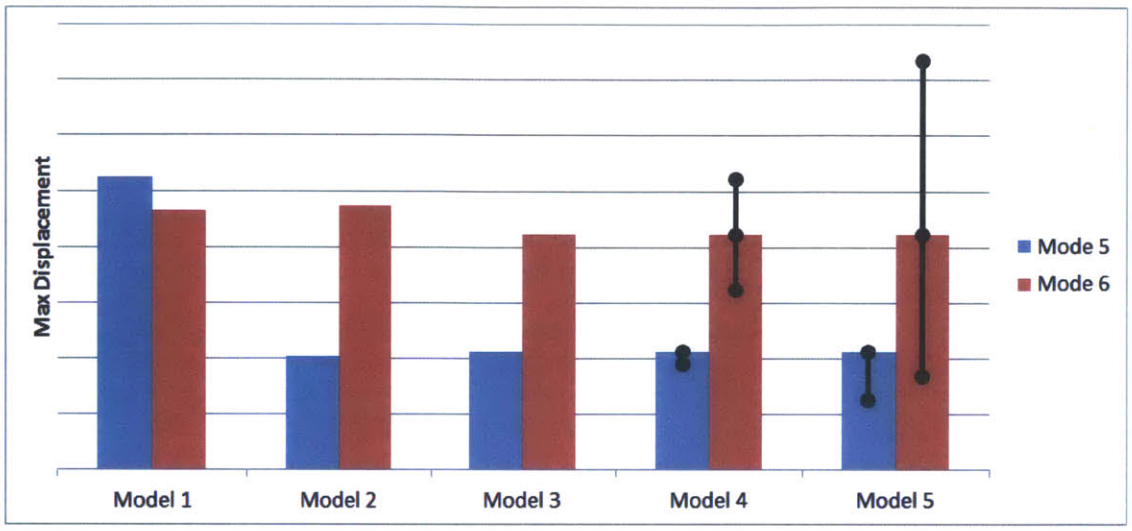

Figure 4-1: Variation in modal displacement for the five models studied.

and acoustic waveform are found to be nearly equal in length when the structural wavelengths of splitter modes 5 and 6 are compared to the acoustic wavelength estimated from the computed flow field. Figures 4-2 and 4-3 show an overlay of the approximate structural mode shapes and the acoustic wavelengths for modes 5 and 6 respectively. The acoustic wavelength is shown for two approximations: 1) From steady-state CFD by evaluating Equation 1.1 outside the boundary layer and 2) averaged from time-accurate loading using unsteady CFD. The acoustic wavelength is determined from CFD results at the respective operating points for both mode crossings. The structural wavelength is approximated by identifying peaks, troughs, and zeros in the mode shape along the splitter chord. Both approximations of the acoustic signal show that at some point along the splitter chord the acoustic wavelength matches the structural wavelength of either mode 5 or 6. It is not obvious from Figures 4-2 or 4-3 whether mode 5 or mode 6 will lead to a higher forced response, but that either mode could be excited by the spatially distributed traveling wave loading.

Figures 4-4 and 4-5 show the modal pressure distribution on both the pressure side (PS) and suction side (SS) normalized by the maximum modal pressure computed with CFD at stage inlet conditions. The modal pressure is the dot product portion of the modal force calculation in Equation 3.3 prior to integration over the surface.

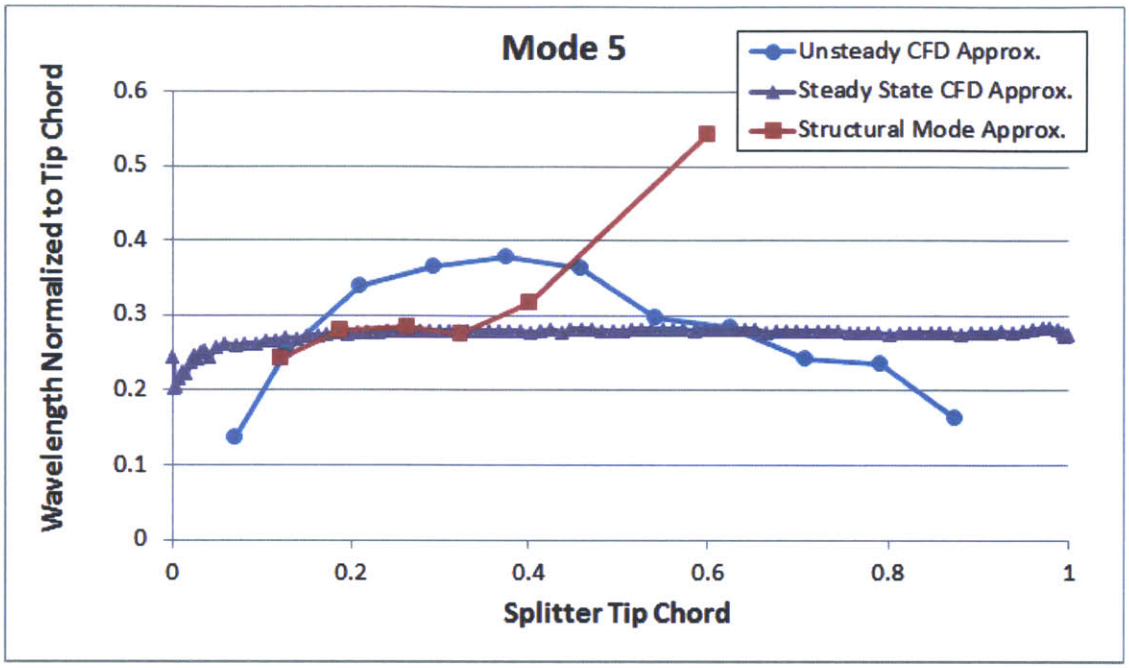

Figure 4-2: Comparison of acoustic and structural wavelengths derived from CFD and FEM respectively for splitter mode 5.

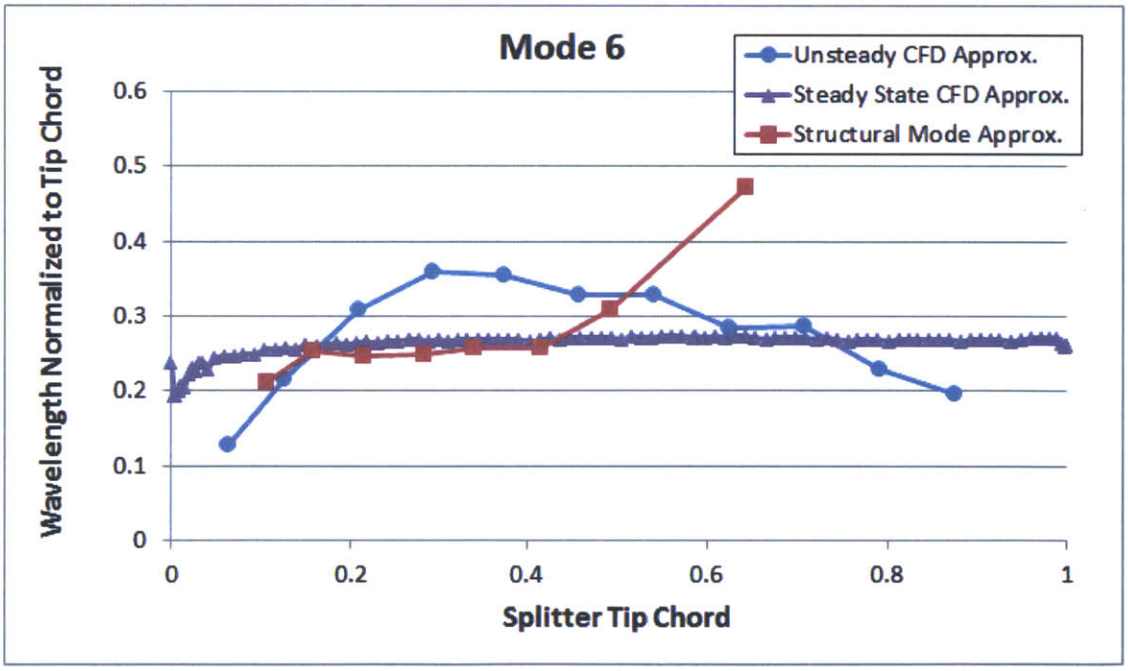

Figure 4-3: Comparison of acoustic and structural wavelengths derived from CFD and FEM respectively for splitter mode 6.

This modal pressure distribution shows where the forcing function and mode shape are well correlated. The strength of the correlation indicates the amount of work being done by the unsteady flow field on the structure during one vibratory period. For both modes, the highest modal pressure is found at tip locations along the chord. Mode 6 also shows non-zero modal pressure on the last 15% of the chord while mode 5 does not, indicating additional work is done in the vicinity of the trailing edge. For Model 1, since the CFD is not implemented at the operating conditions, the computed unsteady pressures are scaled by the exducer dynamic head. This scaling assumes the Campbell crossing speeds for both modes are similar in corrected conditions, an assumption that will be revisited when Model 2 is elaborated further.

The variation seen in the resonant displacement from Model 1 to Model 2 in Figure 4-1 is a result of introducing unsteady pressures calculated at the Campbell crossing speed for each mode. By using the same unsteady pressures at STP inlet corrected conditions in Model 1, the assumption is made that the loading fluctuation varies proportionally with exducer dynamic head if the corrected conditions are maintained. This assumes that flow similarity exists between the design point at STP inlet conditions and the Campbell crossings at operating speed. If the corrected conditions are equal, flow similarity should maintain the unsteady amplitude, acoustic wavelength and upstream extent of the loading as seen in Figure 3-14. As expected, the loading fluctuation is found to scale approximately (<1% on average at tip and midspan) with the exducer dynamic head from STP corrected inlet conditions to the aerodynamic design point stage conditions while maintaining corrected speed and flow. However, despite that the mode 5 and 6 crossings are less than 3% different in corrected speed, Figure 4-6 shows that the normalized loading fluctuation at the mode 5 crossing is about 19% less than that at the design point. This variation in blade loading helps explain why Model 1 overestimates the forced response of mode 5 relative to Model 2; however, the variation in loading fluctuation with corrected speed does not fully account for the remaining overestimation of the blade's displacement. If the amplitude of the forcing function cannot account for the total overestimation in blade displacement, then the upstream extent or shape of the forcing function must

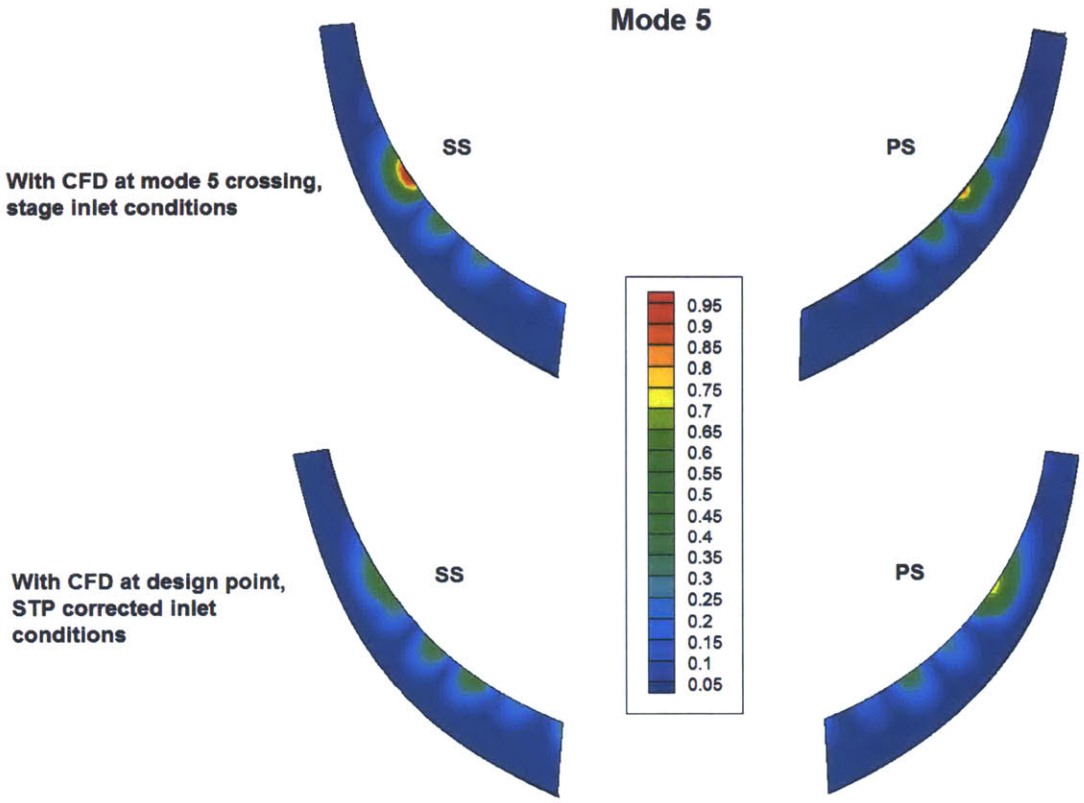

Figure 4-4: Comparison of modal pressure distribution of splitter mode 5 with unsteady pressure calculated at the mode 5 crossing speed and design point speed. Design point CFD is run at STP inlet corrected conditions and scaled by exducer dynamic head. All results normalized to maximum design point modal pressure.

be responsible.

Figure 3-15 shows that the upstream extent of the loading is nearly identical for the corrected speeds considered. The overestimation in displacement is then set by the variation in acoustic wavelength with corrected speed. Figure 4-7 shows the computed acoustic wavelengths at the splitter blade tip and midspan. The acoustic wavelengths are computed at the aerodynamic design point with STP inlet conditions and the mode 5 and 6 crossings at stage inlet conditions. Good agreement exists in the computed acoustic wavelength at the splitter tip in the region of highest unsteadiness (>50% chord). However, in the region of highest unsteadiness, the computed midspan

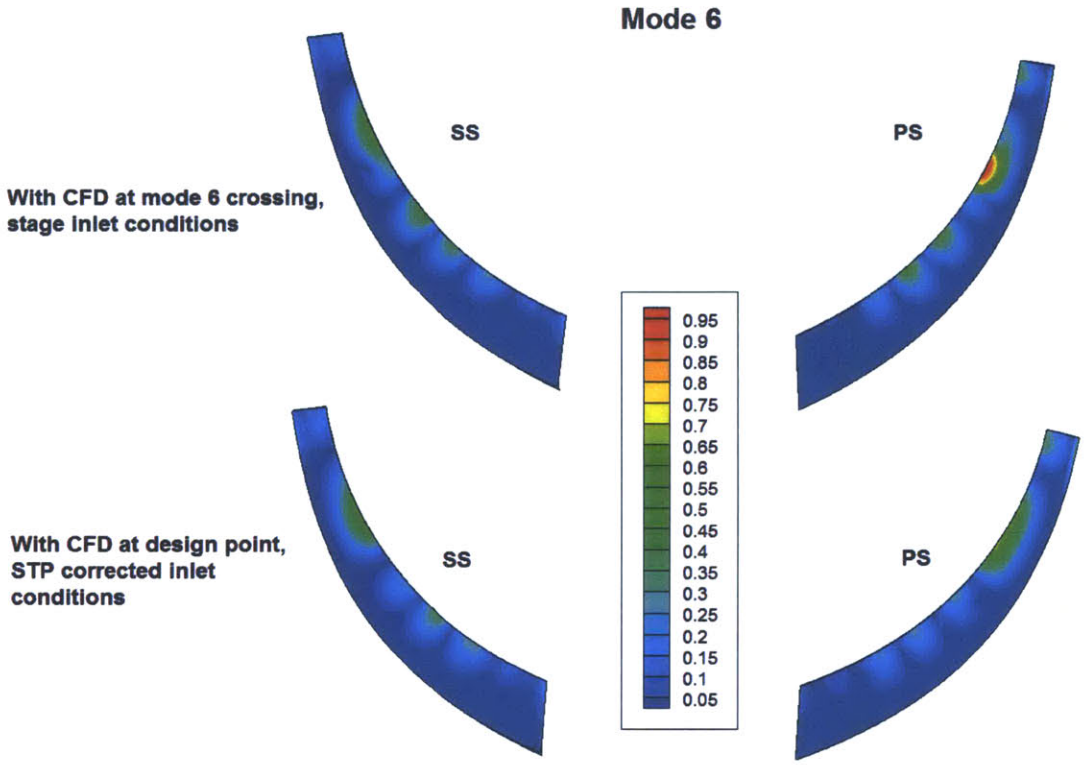

Figure 4-5: Comparison of modal pressure distribution of splitter mode 6 with unsteady pressure calculated at the mode 6 crossing speed and design point speed. Design point CFD is run STP inlet corrected conditions and scaled by exducer dynamic head. All results normalized maximum design point modal pressure.

acoustic wavelength of mode 5 is about 27% greater than that computed at the mode 6 crossing and design point speeds. With this difference in wavelengths, the forced response varies by over a factor of 50% which indicates the sensitivity of the forced response to the spatial correlation between the mode shape and forcing function.

In Chapter 2, the sensitivity of the forced response due to the spatial correlation of the mode shape and forcing function was assessed for a Bernoulli-Euler beam. Since the wavelength of the unsteady loading and mode shape for both modes are shown to be equal at some chord location, Figures 4-2 and 4-3, a reduction factor on the computed forced response with STP inlet corrected CFD can be estimated from the BE beam assessment. Figure 2-8 indicates that for a 27% mismatch in

wavenumbers (or wavelengths) the BE beam forced response should be mitigated by 60%. With this reduction in the forced response amplitude, the mode 5 response of Model 1 now varies by only 15% relative to the response computed with Model 2. For mode 6 the reduction factor for load fluctuation is 9% and the reduction factor for spatial correlation is <1% making the variation in forced response between Model 1 and 2 11%. The spatial correlation reduction factor applied assumes that the forced response is maximized with the STP inlet corrected CFD and reduced when the Campbell crossing CFD is introduced. Since the Model 1 response with the two reduction factors applied agrees well with the Model 2 response, the rationality of the assumption is supported. Figure 4-8 shows the variation between the computed forced response of Model 1 and 2 when the reduction factors are applied.

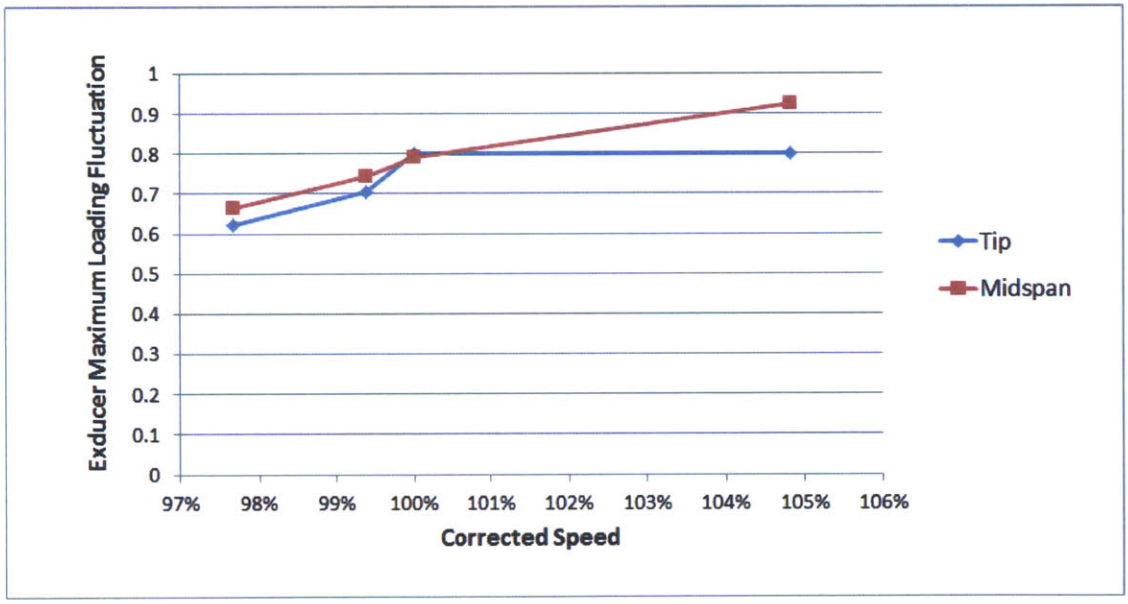

Figure 4-6: Variation in loading fluctuation normalized by exducer dynamic head with corrected speed. The loading fluctuation represents the maximum value along the splitter chord which is in the vicinity of the trailing edge.

4.2 Role of Backwall Modes

The variation in maximum resonant displacement seen in Figure 4-1 from Model 2 to Model 3 is a result of using cyclic symmetry boundary conditions rather than

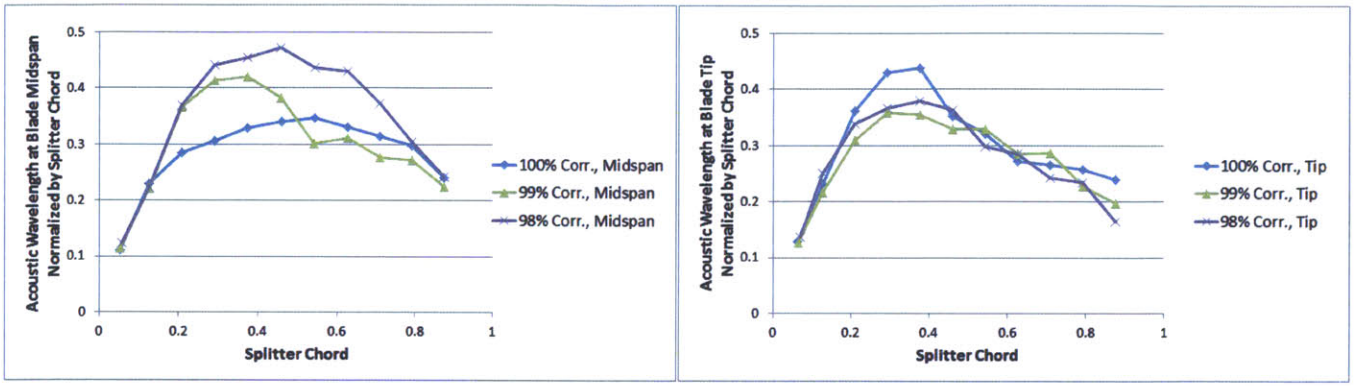

Figure 4-7: Comparison of midspan and tip acoustic wavelengths derived from CFD unsteady loading for the design point at STP inlet conditions and the mode 6 and mode 5 crossings at stage inlet conditions.

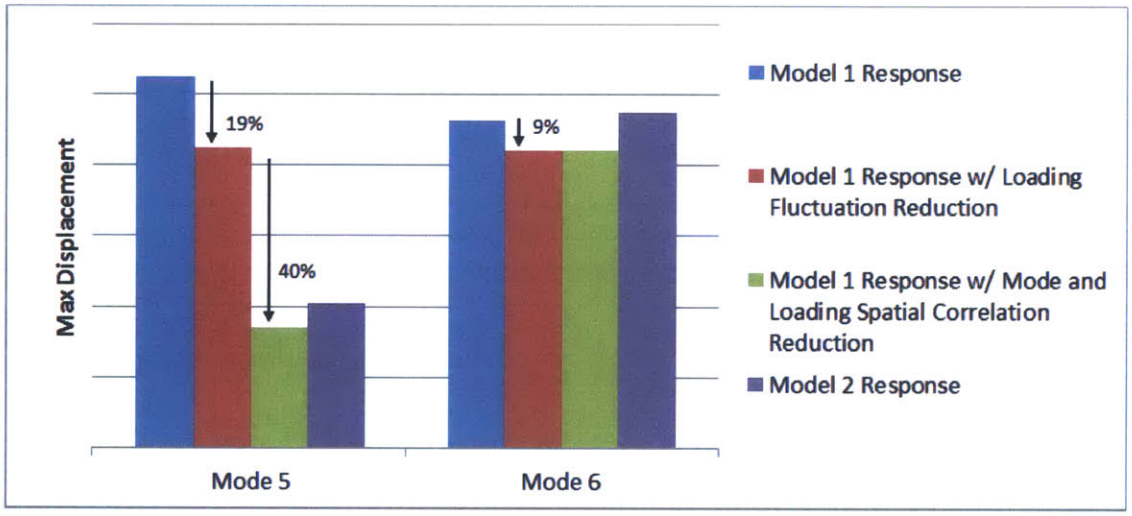

Figure 4-8: Waterfall of reduction factors applied to approximate the response of Model 2 from Model 1. Model 1 uses unsteady CFD computed at the design point corrected to STP inlet conditions for both mode 5 and 6 while Model 2 using CFD calculated at the respective Campbell crossings to compute the forced response.

fixed in space boundary conditions on the cut surfaces of the sector model. The new boundary conditions are introduced while maintaining the use of unsteady CFD calculated at the respective Campbell crossing speeds. Note the relatively larger change in forced response displacement for mode 6 (12%) than mode 5 (3%) as the boundary conditions are changed. The variation in displacement computed for mode 6 is attributed to the altered mode shape at the splitter trailing edge due to the different boundary conditions. Figure 3-4 shows that the magnitude of the mode shape at the

trailing edge is altered more for mode 6 than mode 5 when cyclic symmetry boundary conditions are introduced. When the modal force is computed for nodal diameters 0 to *N/2*, shown in Figure 4-9, it appears that mode 6 has a local variation in the modal force at an IBPA, or nodal diameter, close to the diffuser engine order while mode 5 does not.

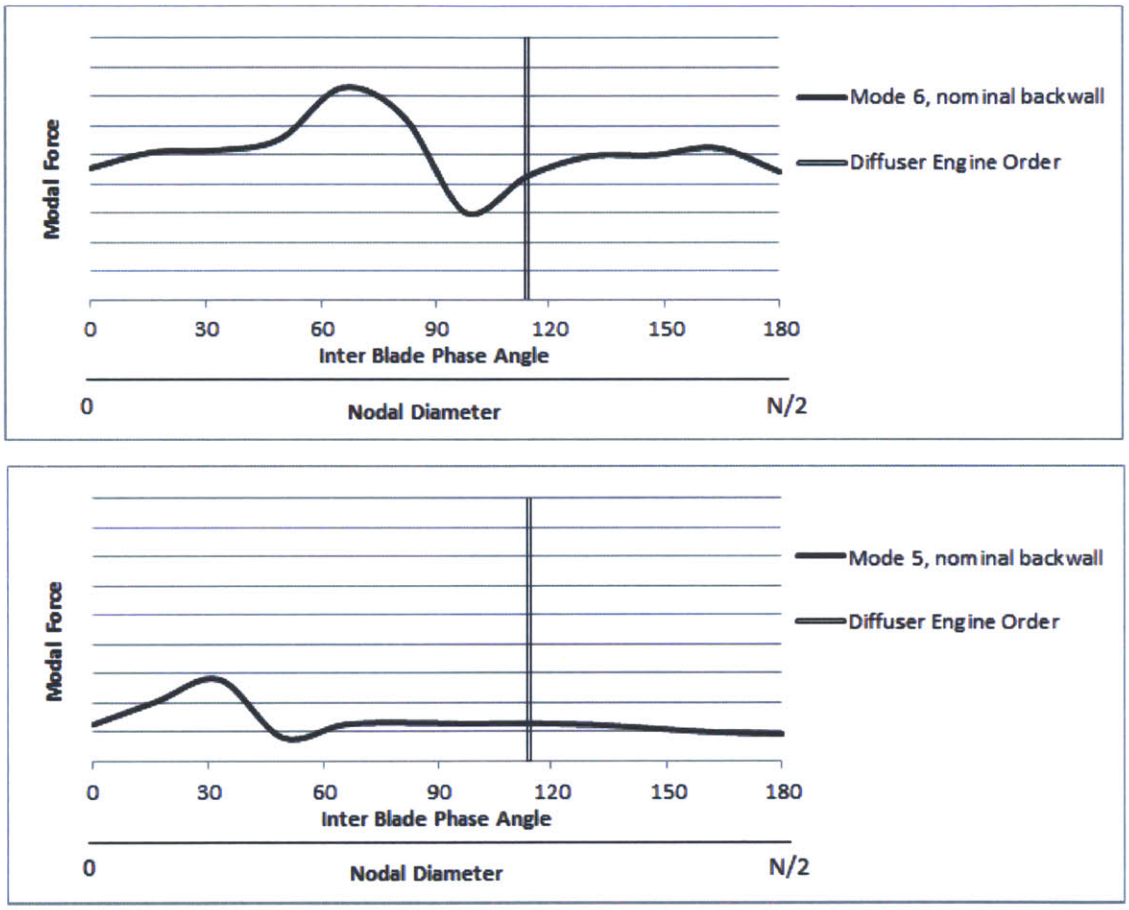

Figure 4-9: Modal force calculated for splitter modes 5 and 6 as a function of IBPA or nodal diameter.

The variation in the computed modal force with nodal diameter is hypothesized to be directly related to the proximity of backwall dominant modes to the splitter blade dominant modes as indicated on the simplified SAFE diagram. The SAFE diagram for this impeller shown in Figure 1-5 indicates that mode 6 is close to the blade-backwall mode interaction with the diffuser excitation while the same is not true for mode 5. The proximity, in frequency and nodal diameter, of the blade-backwall mode

coupling to a splitter blade mode appears to be responsible for the variation in forced response seen with cyclic symmetry boundary conditions on Model 3. The proximity of this coupling and its effect on the forced response is quantified through sensitivity studies of the forced response on backwall and blade thickness.

4.2.1 Influence of Backwall Thickness

To further explore the impact backwall modes have on the forced response of the splitter blades, a sensitivity study on backwall thickness is performed. Figure 4-10 shows the geometry variation performed on the impeller backwall. The backwall thickness is varied at the exducer radius between -24% and +18% with the positive sign indicating an increase in thickness. The same FEM model is used to assess each backwall thickness by translating only the backwall surface nodes a prescribed axial distance. The variation in the blade's displacement at resonance as a result of backwall thickness changes is captured by the black bars on Model 4 in Figure 4-1. These bars indicate that the variation in displacement with backwall thickness is about 9 times greater for mode 6 than mode 5. Figure 4-11 shows the updated SAFE diagram for this impeller stage for the increased backwall thickness of 6%. The backwall frequencies increased (by about 3% at the diffuser engine order) as the outer circumference of the disk has become stiffer. Figure 4-14 shows how the frequencies of the backwall and airfoil dominant modes change with the backwall thickness. The airfoil frequencies change by less than 1% so the backwall thickness sets the disk mode frequency relatively independent of the airfoil modes. As expected, the backwall mode frequencies linearly increases with backwall thickness in accordance with Equation 3.11.

As the backwall thickness is increased at the engine order of the diffuser, the forced response amplitude of the splitter blade increases by about 60%. Figure 4-12 shows this trend in displacement with backwall thickness. The result is surprising because despite an increase in the frequency margin between splitter mode 6 and the disk modes the maximum physical displacement at the diffuser engine order increases! The modal coupling of the blade and backwall affects the net modal force calculated.

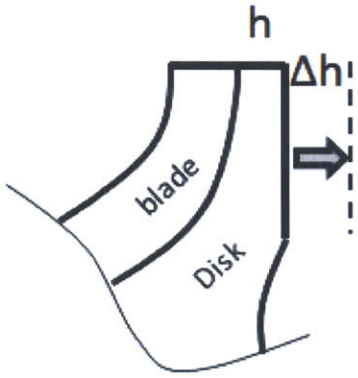

Figure 4-10: Schematic of how the disk's backwall geometry is changed for modeling Model 4.

Figure 4-13 shows how the modal force varies in the IBPA or nodal diameter space. It appears that this interaction between the disk and blade motion can either constructively or destructively interfere, resulting in a variation of modal force about a nominal value. If the diffuser engine order excitation was at an IBPA closer to 80 degrees (say due to a different vane count) then an increase in thickness would have brought a drop in the modal force for mode 6 assuming the forcing function remains unchanged.

4.2.2 Influence of Airfoil Thickness

Model 5 further explores the impact backwall modes have on the forced response of the splitter blade due to small changes in the impeller geometry. For this model, small changes in the airfoil geometry are made by uniformly thickening the splitter and main blade along the span, as shown schematically in Figure 4-15. The variation in the blade's displacement at resonance as a result of airfoil thickness changes is captured by the black bars on Model 5 in Figure 4-1. The bars indicate that the variation in displacement is greater for mode 6 again than for mode 5, by a factor of about 6.5. Figure 4-16 shows the updated SAFE diagram for this impeller stage for the increased airfoil thickness of 13% at the tip. The airfoil frequencies increased by

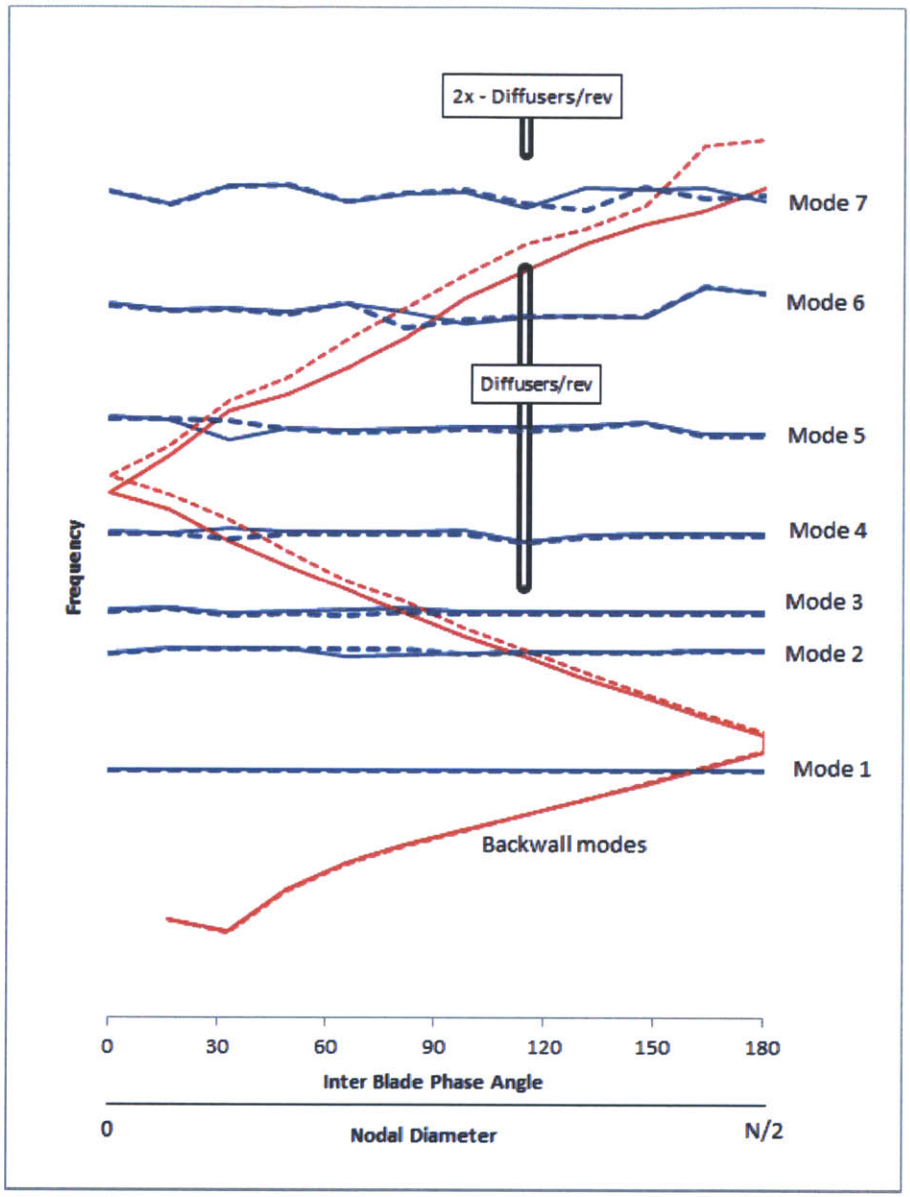

Figure 4-11: Updated SAFE diagram for the impeller showing the change in backwall mode placement for a 6% thicker backwall at the exducer radius. Blue = splitter modes, red = backwall modes, solid line = nominal geometry, dashed line = thicker geometry.

about 10-12% as the airfoil becomes stiffer. Figure 4-18 shows how the frequencies of the backwall and airfoil dominant modes change with the airfoil thickness. The backwall frequency changes by less than 1% so the airfoil thickness sets the airfoil mode frequency relatively independent of the backwall modes. As expected, the

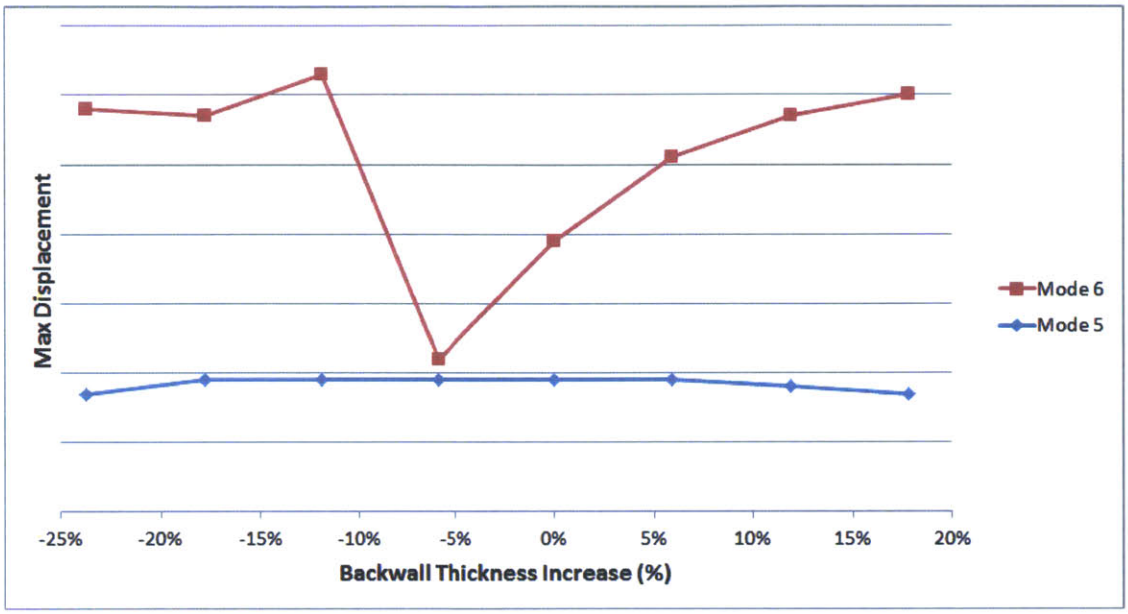

Figure 4-12: Maximum displacement at resonance as a function of backwall thickness increase at the IBPA (or nodal diameter) of the diffuser engine order.

airfoil mode frequencies linearly increase with airfoil thickness in accordance with Equation 3.10.

As the airfoil thickness is varied between -10% and 25%, at the engine order of the diffuser, the maximum physical displacement is seen to drop for both modes 5 and 6. This trend indicates that as the blade becomes stiffer, due to the added thickness, the forced response of the blade decreases. The variation in the computed displacement about this nearly linear decay shows both a drop and increase in the displacement between 3% and 10% increase in airfoil thickness. In agreement with the backwall thickness change assessed previously, the maximum variation in the forced response occurs when the backwall and mode 6 frequencies are equal, as shown in Figure 4-18. Since the same unsteady loading is used to compute the forced response for all airfoil or backwall thicknesses, the magnitude and phase of the mode shape must set the computed modal force variation.

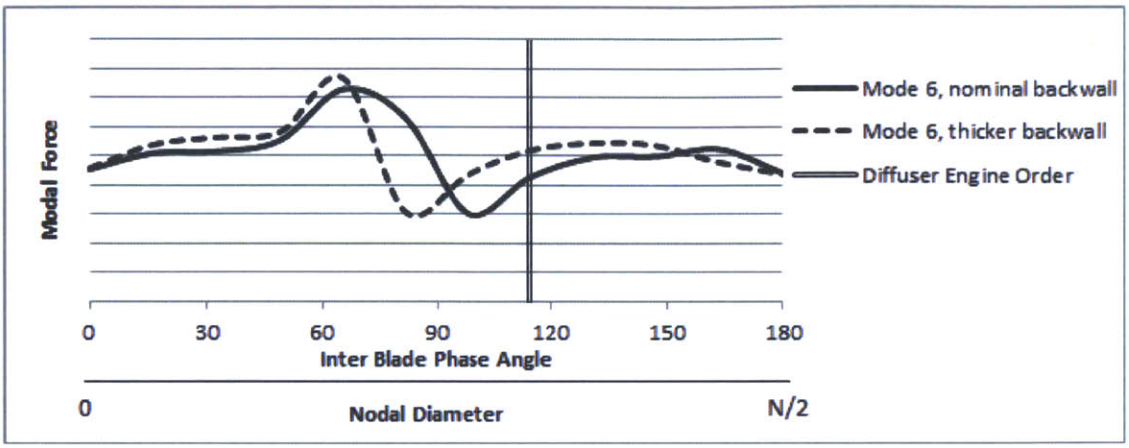

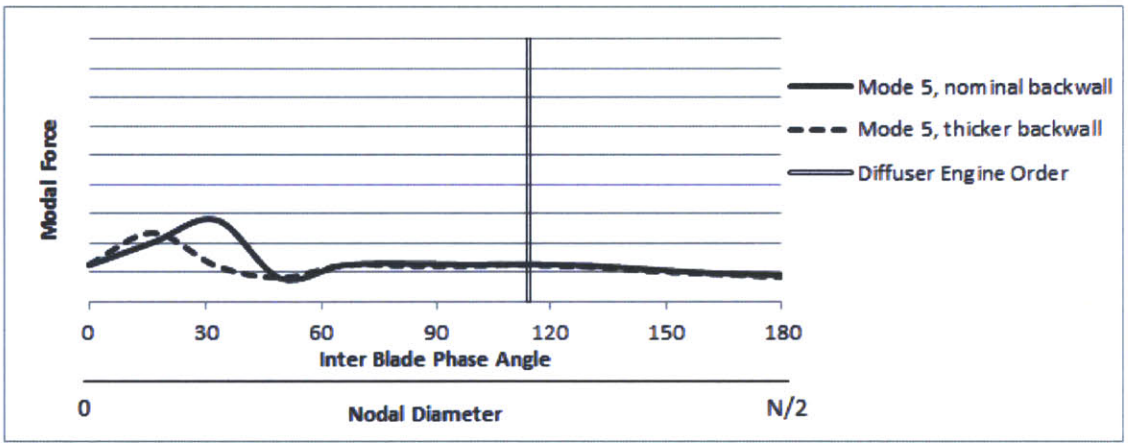

Figure 4-13: Modal force calculated for splitter modes 5 and 6 as a function of IBPA or nodal diameter with the nominal and 5% thicker impeller backwall.

4.2.3 Role of Mode Shape Magnitude and Phase

For both thickness variation studies the modal force varied more for mode 6 than mode 5 which is attributed to the coupling of blade and backwall modes. How this coupling leads to variation in the forced response is explained by the magnitude and phase of the mode shape defined by Equations 3.13 and 3.14. Figure 4-19 plots the mode shape magnitude at the blade tip for several airfoil and backwall thicknesses. In the trailing edge of the splitter blade where the unsteadiness is highest, the mode shape magnitude of splitter mode 5 is virtually unchanged over the range of thicknesses assessed. Mode 6, however, shows greater variation in magnitude with a maximum value near the blade-backwall coupling thickness. Figure 4-19 plots the mode shape

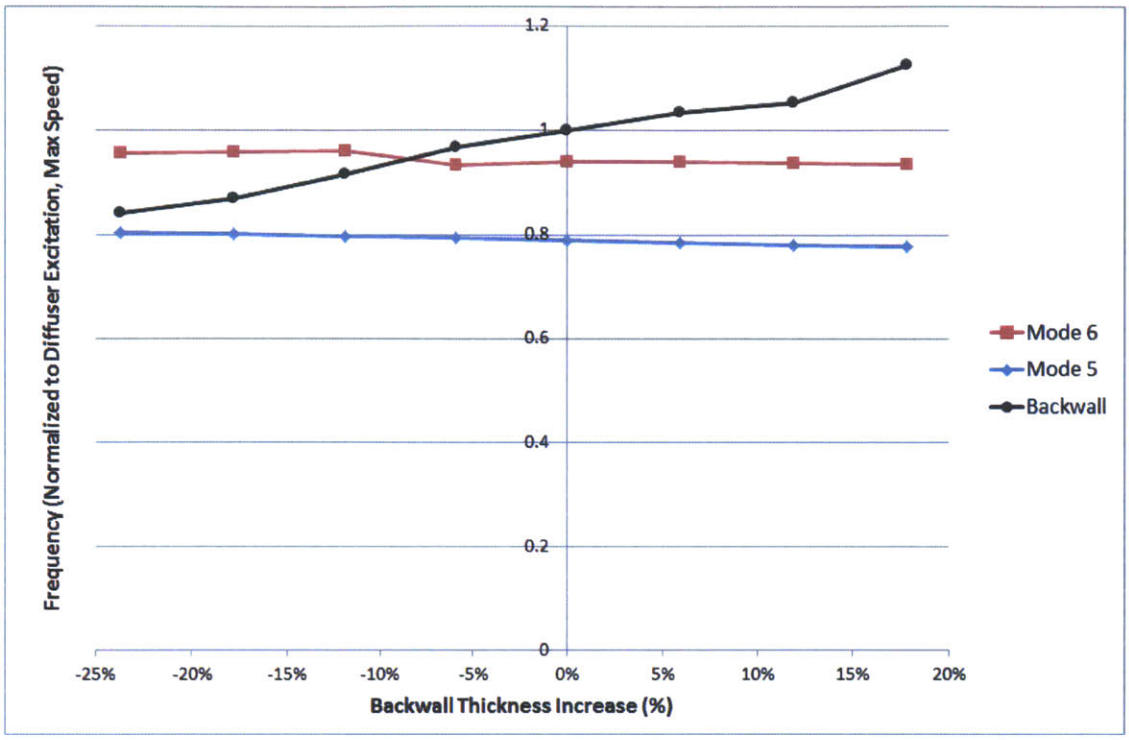

Figure 4-14: Frequency map showing interaction of backwall and disk modes as backwall thickness is varied.

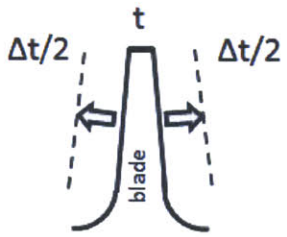

Figure 4-15: Schematic of how the splitter blade geometry is changed for modeling model 5.

phase at the tip for several airfoil and backwall thicknesses. Much of the airfoil has the same phase except for the tailing edge region. For mode 5 there is little variation in the mode shape phase for changes in both blade and backwall thickness. The phase of mode 6 shows a 180 degree phase shift between the airfoil leading edge and trailing edge which occurs near the blade-backwall coupling thickness. Figures 4-21 and 4-22 compare the forced response amplitude, mode shape magnitude and phase

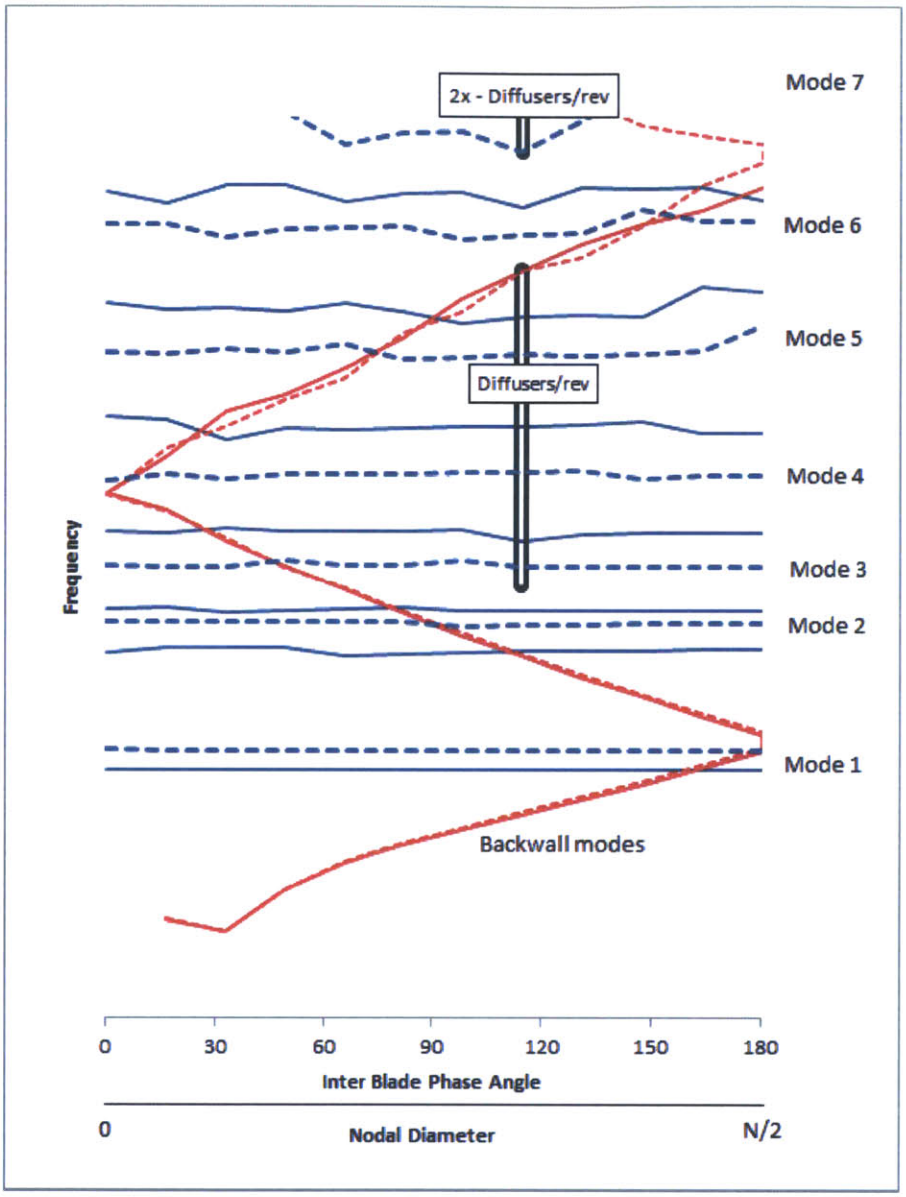

Figure 4-16: Updated SAFE diagram for the impeller showing the change in backwall mode placement for a 13% thicker airfoil. Blue = splitter modes, red = backwall modes, solid line = nominal geometry, dashed line = thicker geometry.

as a function of blade or backwall thickness. For mode 6 the variations in these three parameters all occur near the blade-backwall coupling indicating their role in the forced response behavior at a veering point.

In Appendix A a two mass-spring system model is constructed to assess the role of mode coupling on the forced response. The system models the impeller with an airfoil

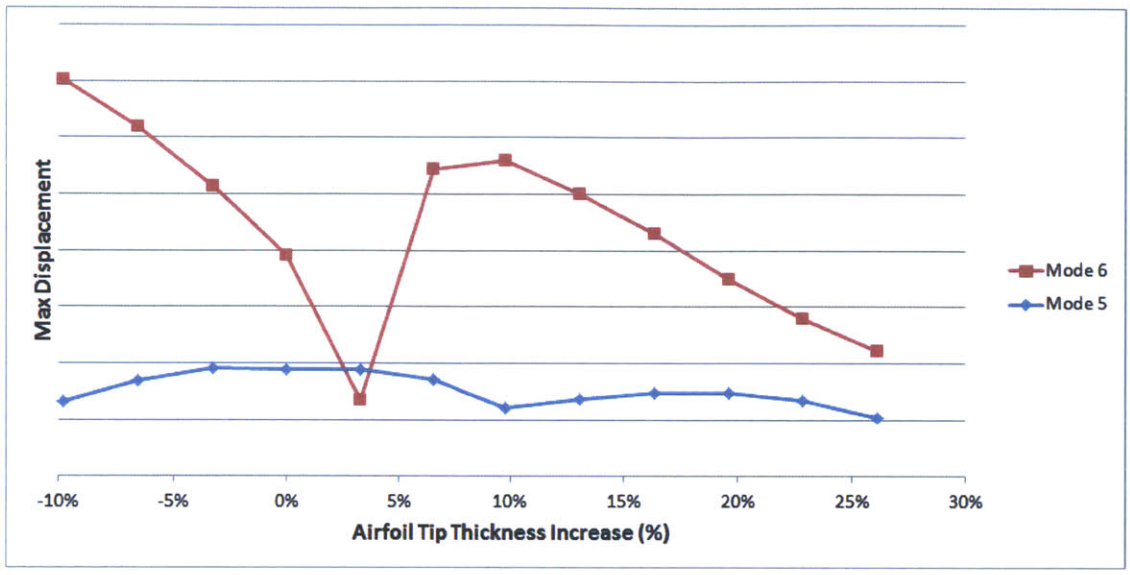

Figure 4-17: Maximum displacement at resonance as a function of airfoil thickness increase at the IBPA (or nodal diameter) of the diffuser engine order.

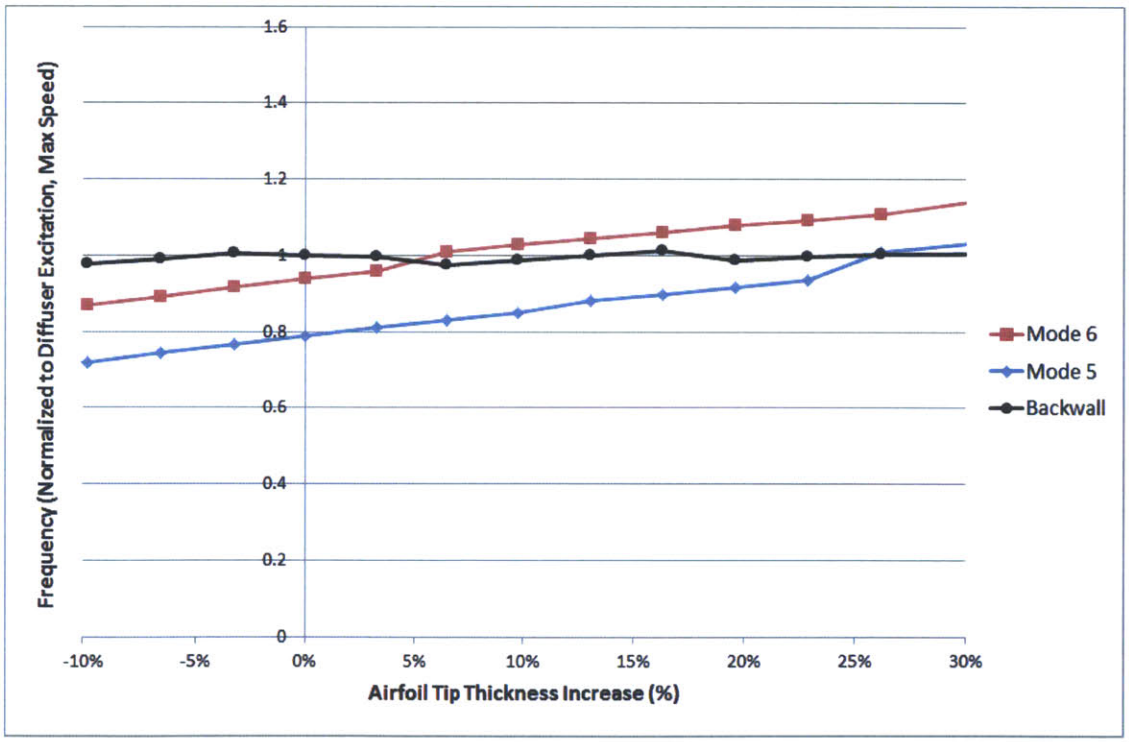

Figure 4-18: Frequency map showing the interaction of backwall and disk modes as airfoil thickness is varied.

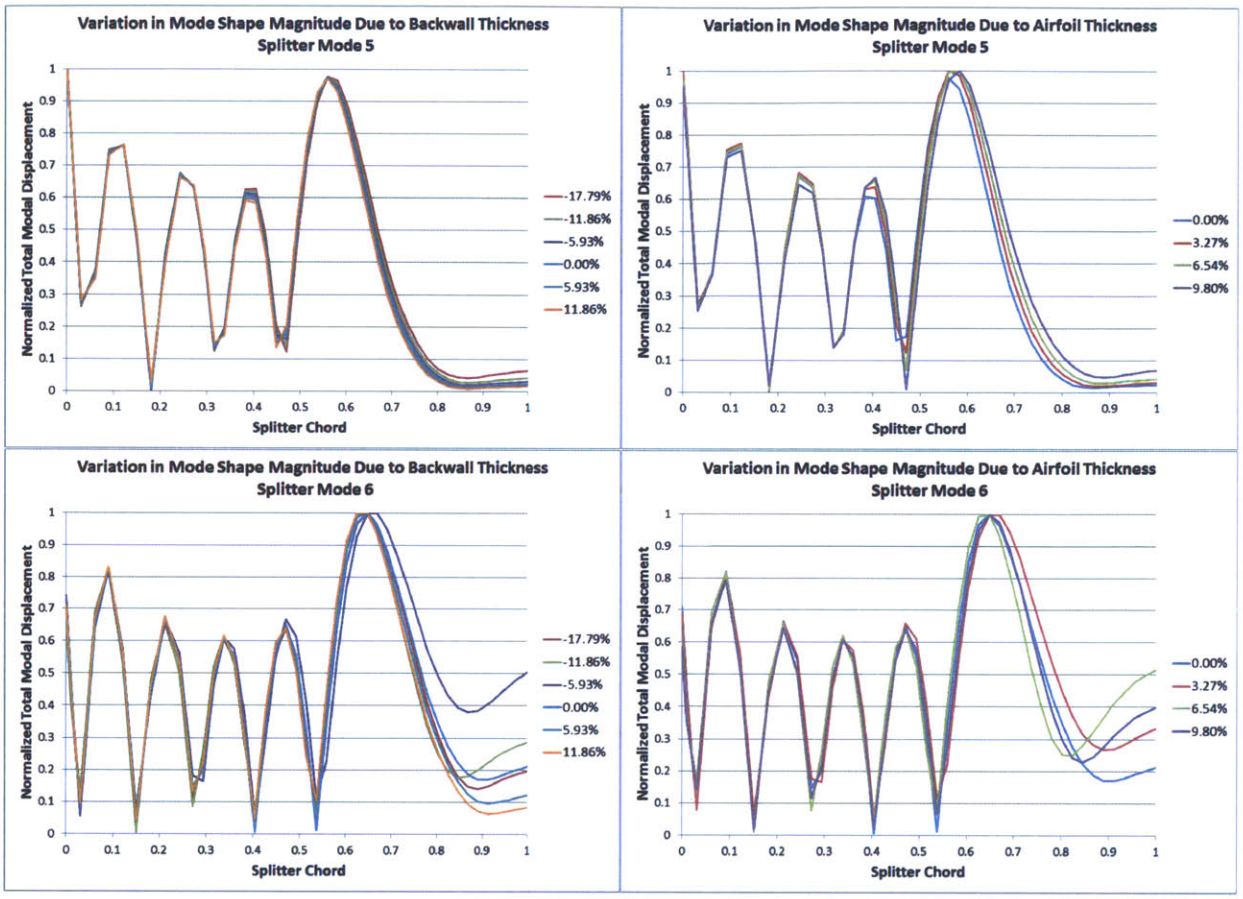

Figure 4-19: Mode shape magnitude variation for splitter modes 5 and 6 for the two geometry variations assessed.

mass and disk mass connected by springs. Further details of this model can be found in Appendix A. Similar to the impeller, the system is found to have a variation in the blade's forced response when frequency of the blade dominant and disk dominant modes are nearly equal. Unlike the impeller, however, the two masses of this system always have the same phase as the modes of vibration are standing modes. Figure A-6 shows that the behavior the computed forced response of the impeller and the two mass-spring system shows good agreement in the vicinity of a modal veering point.

The impact of mode shape phase on the impeller's forced response helps explains why the forced response increases and decreases while for the two mass-spring system, only a reduction in the forced response occurs. For the impeller, variations in mode shape magnitude and phase at a veering point contribute to the variation in forced

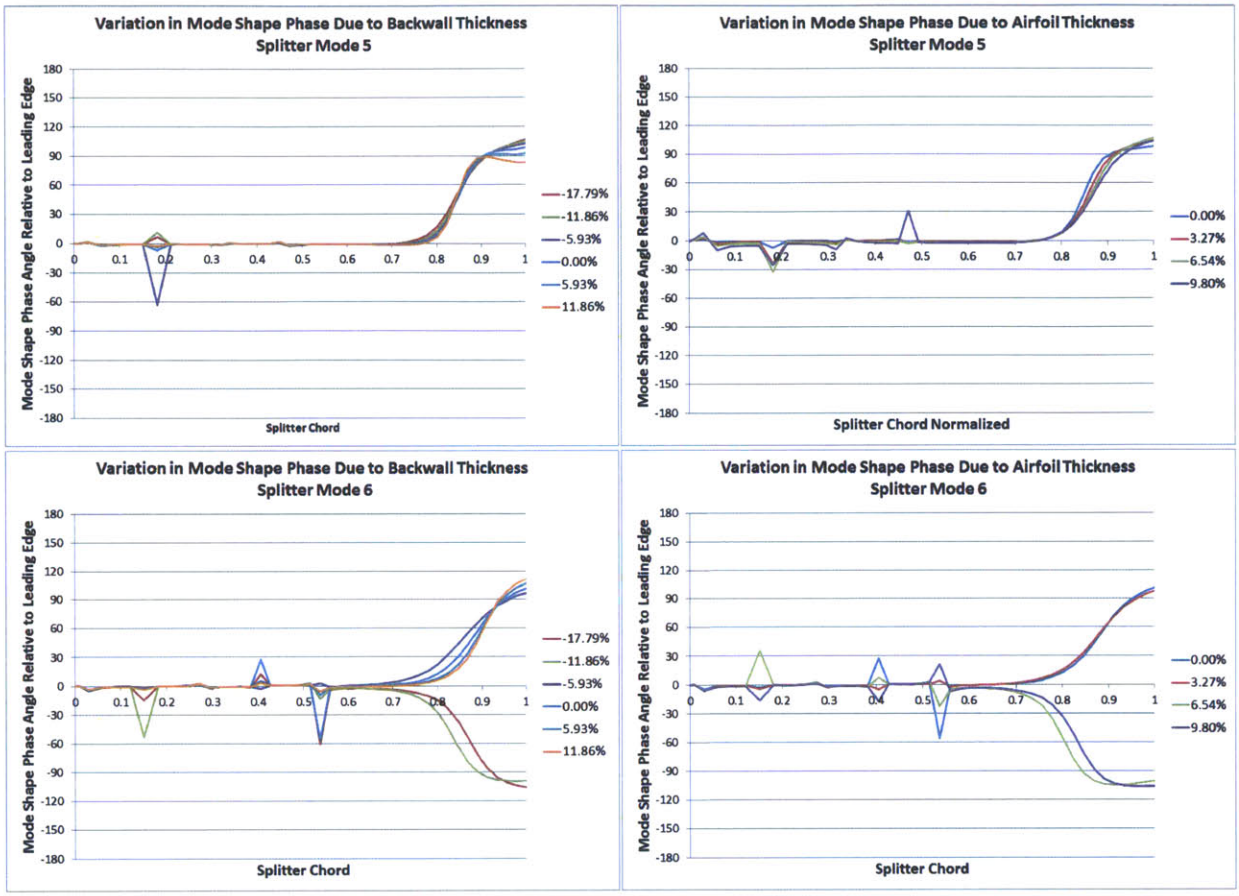

Figure 4-20: Mode shape phase variation for splitter modes 5 and 6 for the two geometry variations assessed.

response while for the two mass-spring system, only variations in magnitude at the veering point contribute to the forced response variation as the two masses are always in phase.

4.3 Summary

The conditions and attendant governing physical mechanisms that set the forced response of the centrifugal impeller have been elucidated. The correlation of the mode shape with the unsteady forcing function is important but not the dominant mechanism at play for this centrifugal impeller as both structural vibratory modes have wavelength equal to the acoustic forcing wavelength at chordwise locations on the

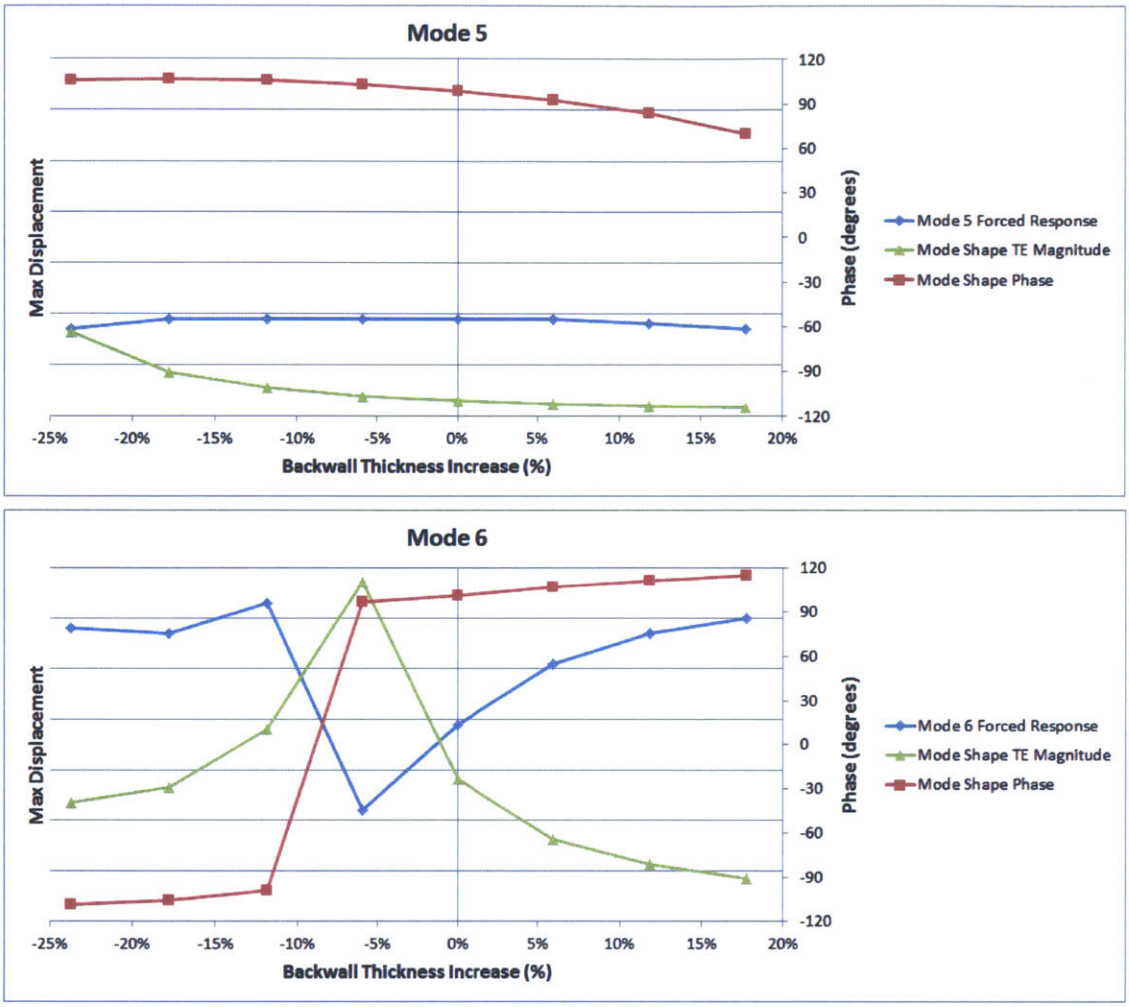

Figure 4-21: Variation in splitter mode 5 and 6 forced response, mode shape magnitude, and mode shape phase with backwall thickness.

splitter. The role of backwall modes, instead, is the dominant feature which sets the forced response of the research impeller. The placement of the backwall dominant modes relative to the airfoil dominant modes, considering the manufacturing tolerances of the blade and backwall thicknesses, is an important driver of the impeller's forced response. The real implication of this finding is that the forced response of an impeller blade cannot be solved solely by stiffening the structure without consideration of potential mode couplings with the disk.

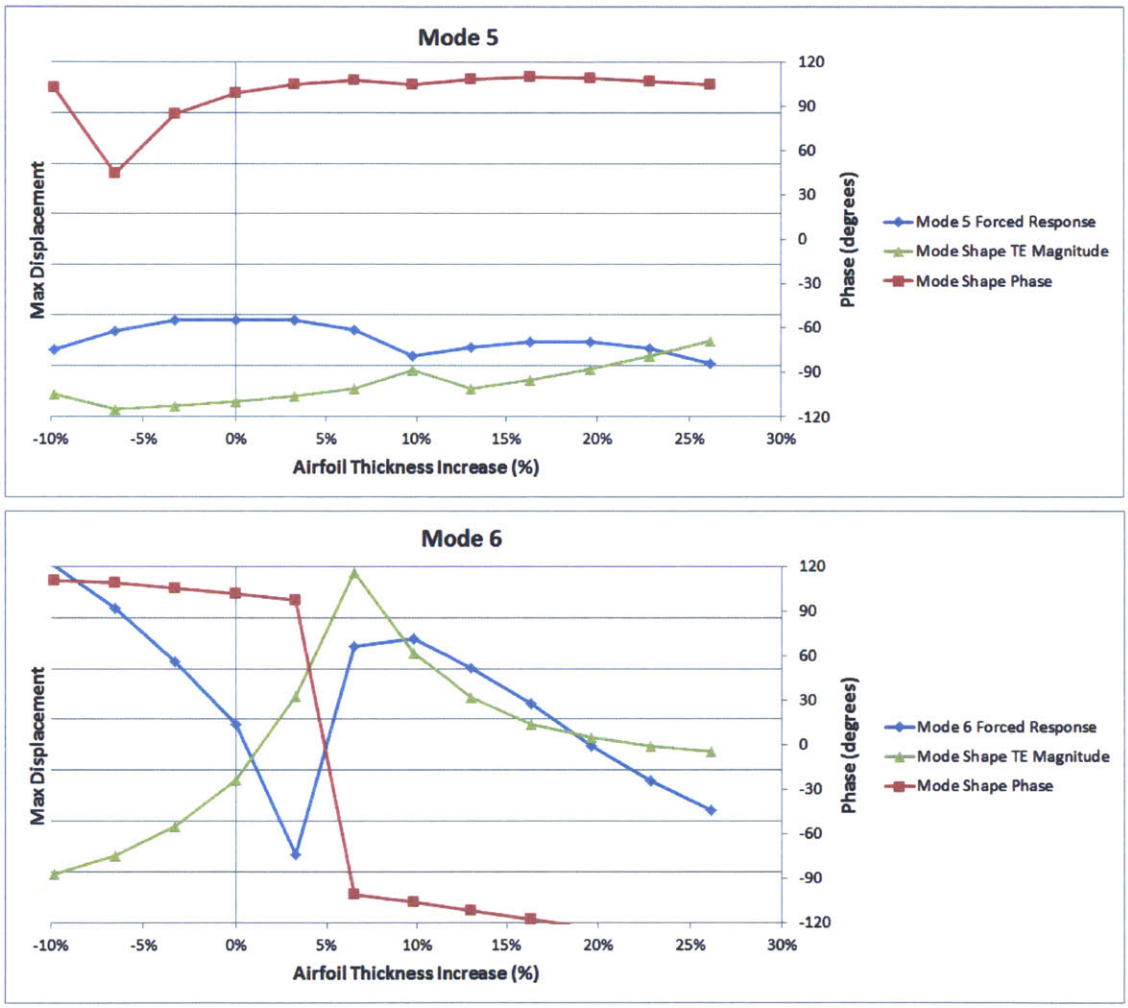

Figure 4-22: Variation in splitter mode 5 and 6 forced response, mode shape magnitude, and mode shape phase with airfoil thickness.

Chapter 5

Assessing the Forced Response Risk of a Centrifugal Impeller

5.1 Decision Tree Risk Assessment Tool

As shown in Chapter 4, there are several physical mechanisms that influence the resonant response of a centrifugal compressor stage impeller due to the impeller-diffuser interaction. To evaluate the relative risk each mechanism has on the forced response of the impeller, a decision tree is proposed. Figure 5-1 shows the proposed decision tree which asks a series of questions regarding the state of natural modes in the operating range. The final question suggests that low risk blade mode crossings with the diffuser may exist in the operating range. The proposed decision tree relies mainly on FEM analysis and steady-state aerodynamics. This tool serves as a method to qualitatively assess risk and determine if more detailed analyses are needed. In practicality, this decision tree helps to identify when a detailed modal force response calculation (using unsteady CFD and FEM mode shapes) is called for.

5.1.1 Campbell Diagram Assessment

The first two questions in the proposed decision tree in Figure 5-1 pertain to the use of the Campbell diagram. If there are no known excitations in the operating range, then

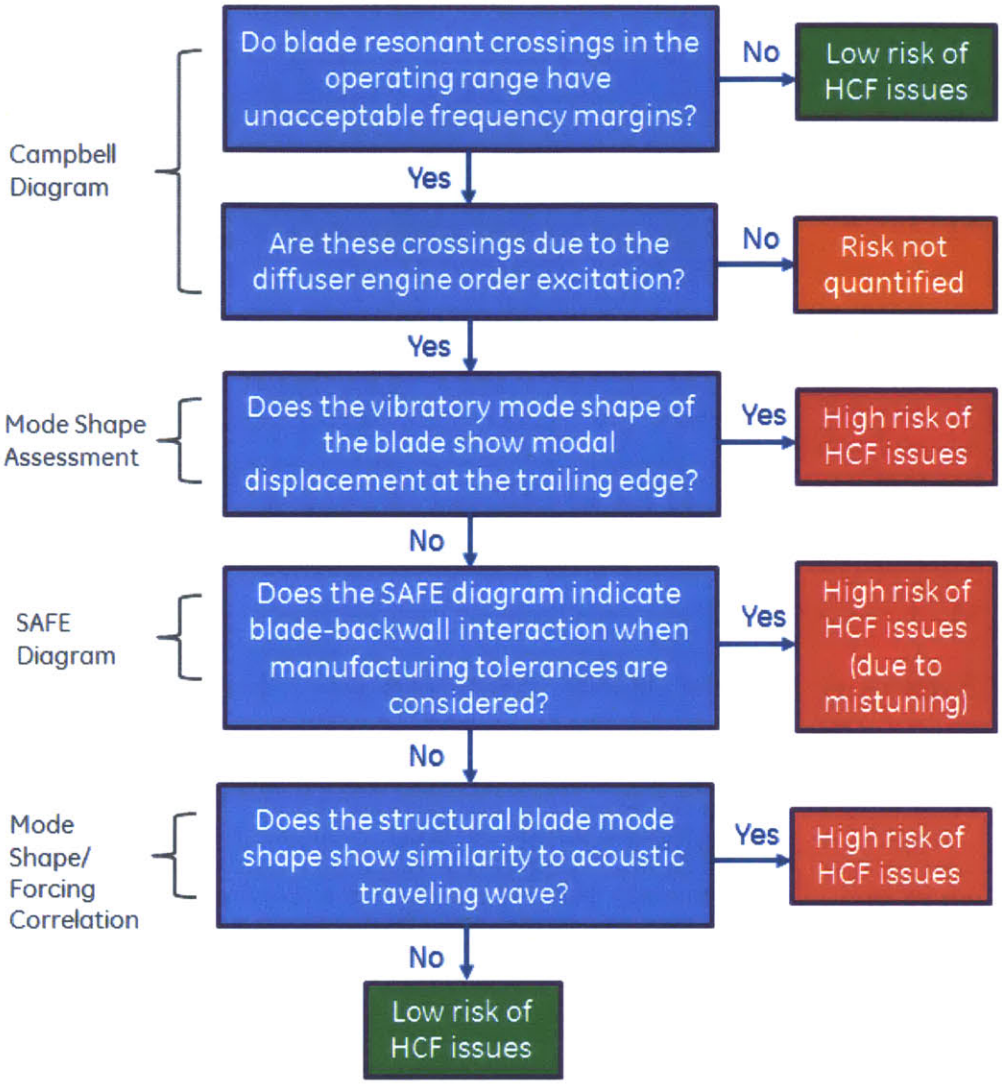

Figure 5-1: Proposed decision tree for identifying resonant risk early on in the design process.

there should be no aeromechanical difficulties due to HCF as a result of synchronous engine order excitation. If there are known excitations in the operating range, and the excitation is due to the diffuser engine order, then risk is further assessed. However, if the excitation in the operating range is from a source other than the diffuser, such as upstream wakes from stationary inlet guide vanes, then the risk is not further ranked here.

Due to the long chord of centrifugal impellers, some structural blade modes may be of the same edgewise family and can therefore not be tuned independently. As a result, it may not be possible to completely free the operating range of impeller blade modes. Some modes may be allowed to exist away from critical design speeds as they are only encountered for a short period during an operational transient such as a start up or shutdown. The decision tree is still applicable but adequate frequency margin to these critical speeds should be the first priority. This frequency margin is defined as

$$frequency_{margin} = \left| \frac{f_{excitation}}{f_{structure}} - 1 \right| \tag{5.1}$$

where both the frequency of the excitation and the structural mode are computed at the same engine speed. The frequency margin is expressed as a percentage and is typically chosen based on previous experience. The resonant spectrum plots for the taut string and the Bernoulli-Euler beam, Figures 2-3 and 2-4 respectively, show that the risk of resonance is primarily driven by the temporal frequency matching and only then, subsequently, by the shape matching. As is typical, setting the appropriate frequency margin or clearing the operating range of structural modes of vibration is a good first step to address resonant risk.

If multiple structural mode crossings exist with the diffuser engine order excitation in the operating range, the decision tree can be applied to all crossings. If the risk assessment shows similar levels of risk for all mode crossings, emphasis should be placed on addressing the Campbell crossing at the higher speed. Figure 4-6 shows that the fluctuation in blade loading imposed on the splitter blade increases linearly with corrected speed in the vicinity of the design point and scales with exducer dynamic head; therefore, as the strength of the forcing function increases with speed so too does the computed forced response and risk of resonance.

5.1.2 Mode Shape Assessment

The third decision in the risk assessment decision tree shown in Figure 5-1 concerns the mode shape found from FEM analysis. The question asks whether the mode shape exhibits modal displacements at the trailing edge. For this question, FEM modal analysis is required to determine the centrifugal impeller's structural modes. The objective of the question is to assess the relative stiffness of the trailing edge. The stiffness of the trailing edge is related to the blade span by $1/L^2$, as indicated in Equation 3.10. Designs with stiff trailing edges show little to no modal displacement in the exducer, replicating a clamp-like boundary condition at the trailing edge which cancels out the peak loading fluctuation shown to be near 95% chord in Figure 3-17. Per the modal force equation, Equation 3.3, having little modal displacement in the region of highest unsteadiness is an effective means for reducing the modal work done on the impeller blades. In some cases, as is true for this research centrifugal stage, the upstream extent of the unsteadiness may extend the entire length of the blade chord such that modal work is possible anywhere the mode shape exhibits displacement. Gould showed that this upstream extent of the unsteady loading decays exponentially from the trailing edge to the leading edge and obeys Laplaces equation solved for a background flow with a periodic non-uniformity [9]. The exponential decay of the loading fluctuation is confirmed when plotted on a semi-log axes as in Figure 5-2. On this axis, an exponential decay from the trailing edge to leading edge appears as a linear decay. Regardless of the upstream extent of the unsteadiness, reducing any trailing edge displacement would mitigate the modal work on the blade as the unsteadiness is highest in this location.

To adequately assess the modal displacement of the trailing edge, either the magnitude of total displacement of the mode shape from a sector model with cyclic-symmetry or fixed in space boundary conditions can be used. A full wheel model could also be used; however, a phase sweep should be performed to find the maximum modal displacement of a single blade. Emphasis should be placed on the mode shape's displacement at the blade tip for the full chord as edgewise modes are the

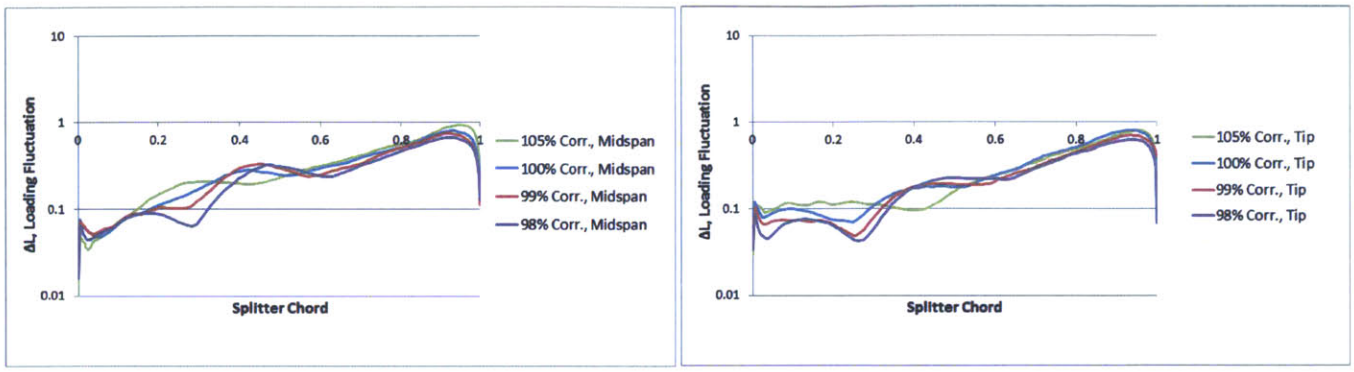

Figure 5-2: Splitter blade loading fluctuation normalized by exducer dynamic head at blade tip and midspan. The linear decay of the loading fluctuation on this semi-log axes confirms the exponential decay of the loading fluctuation from trailing edge to leading edge.

most active here.

If the blade mode shape shows modal displacement at the trailing edge, adding stiffness locally to the trailing edge may be a more effective way to reduce the forced response without affecting the frequency substantially. As shown in Equation 3.10, a global change to the blade's thickness will linearly raise the frequency of the vibratory mode which will impact the Campbell diagram crossing speed and may negatively impact the aerodynamic performance of the impeller blade.

5.1.3 SAFE Diagram Assessment

The fourth decision in the risk assessment decision tree shown in Figure 5-1 asks whether the backwall dominant modes have adequate frequency separation or margin. If the blade mode shapes appear relatively inactive at the trailing edge, the next proposed step is to map the blade-backwall mode interactions. This step also requires no CFD analysis, only further FEM analysis. A full map of the impeller vibratory modes should be plotted in a SAFE diagram showing frequency versus nodal diameter with blade and backwall dominant modes highlighted. The excitation of the diffuser engine order should be away from blade-backwall mode crossings or veering points. As shown in Sections 4.2.1 and 4.2.2, these veering points have been shown in Chapter 4 to significantly vary the forced response of the impeller blades by being highly sensitive

to small changes in the airfoil and backwall thickness. To avoid the blade-backwall interactions, the manufacturing tolerances on both the blades and backwall should be considered to ensure blade and disk dominant modes have adequate frequency margin. The required margin to modal coupling could be found by performing a similar assessment of the trailing edge mode shape magnitude with airfoil thickness, like that shown in Figures 4-21 and 4-22. The attenuation of the trailing edge modal displacement with blade or backwall thickness may give a good indication of the required frequency margin to avoid blade-backwall coupling.

Appendix A shows the blade-backwall interaction modeled as a two mass-spring system. The model shows similar behavior to the centrifugal impeller blade response in the vicinity of a veering point. The stiffness of the springs in the system are varied so that the two natural frequencies of the system couple and decouple. The forced response of the two masses varies accordingly with the coupling. In Figure A-6 the forced response of the "blade" in this simplified model exhibits the same blade-disk interaction seen on the centrifugal impeller. The mode shape magnitude of the blade also appears to increase and decrease at the veering point like that of the impeller.

Effect of Blade-Backwall Mode Coupling on Mistuning

The variation in the computed forced response of the splitter blade due to blade-backwall mode coupling increases the mistuning risk of the impeller. Mistuning is the effect of blade-to-blade frequency variation as a result of manufacturing tolerances on the geometry, variation in material properties, or variations in boundary conditions. If all the blades are identical, at resonance the response amplitude of each blade should be the same which indicates that the vibratory energy is shared equally among the blades. For a mistuned impeller, vibratory energy may be concentrated to a few blades, increasing the response amplitude of these blades relative to the tuned impeller at the same conditions. Mistuning in the vicinity of blade-disk coupling is known to increase as the blades are effectively allowed to "communicate" through the disk which is participating in the vibration [1]. As a result, the risk of a high response due to mistuning becomes increasingly sensitive to geometry variations the closer the

impeller operates to frequencies at which the blades and backwall modes can couple. Studies of mistuned bladed disks have shown that the maximum blade amplitude magnification considering mistuning effects can be as high as 1.8 at a veering point [1]. The results presented here in Chapter 4 do not include the effect of blade-to-blade mistuning.

5.1.4 Spatial Correlation of Mode Shape and Forcing Function

The final decision on the risk assessment decision tree of Figure 5-1 questions how well the vibratory mode shape and the forcing function are spatially correlated. This shape matching is more effective at addressing the resonant risk of modes with mid-chord edgewise modal displacements, as these types of modes are most similar to the transverse modes of the BE beam assessed in Chapter 2. Figure 2-8 shows that as the ratio of the forcing wavenumber to structural mode wavenumber moves away from one, the forced response amplitude of the mode quickly decreases. The acoustic wavelength of the forcing function can be approximated by Equation 1.1 while the structural wavelength can be estimated from the FEM mode shape. The speed of sound and relative Mach number in this equation can be found from steady-state CFD modeling of the flow through the blade passage. Figures 4-2 and 4-3 show that the steady-state approximation of the forcing function using Equation 1.1 gives a good estimate of the average chordwise forcing wavelength computed by unsteady CFD. From this equation, the higher the relative Mach numbers in the blade passage, the lower the upstream phase velocity of the acoustic wave forcing the blade, and therefore, the shorter the forcing wavelength. Also note that Equation 1.1 states that the acoustic wavelength decreases with increasing rotational speed. For small engines with generally higher rotational speeds, there may be an inherent mismatch in the characteristic wavelengths if the modal wavelengths do not scale in accord with the acoustic wavelengths. As shown in Figure 2-8 for classical BE beam forced response, if the ratio of the wavelengths (or wavenumbers) is not between 0.5 and 1.5 the strength

of the response should be reduced by more than 75% of the fully matched result.

5.1.5 Implications of Resonant Risk Assessment Decision Tree

The decision tree presented here shows how to evaluate the resonant risk of centrifugal impeller blades due to the unsteady loading generated by the impeller-diffuser interaction. It is proposed as a way to identify which of the mechanisms enumerated in Chapter 4 may be present in the current design. With this knowledge, appropriate steps can be taken earlier in the design process to minimize the danger of resonance. Ultimately, the physical response of the blade is best found from physical testing and measurement; however, the proposed decision tree may serve as an effective screening tool to identify physical mechanisms critical to the impeller's forced response before testing.

5.2 Summary

The resonant risk decision tree proposed seeks to relate the driving physical mechanisms identified in Chapter 4 to the design process. The questions in the decision tree are presented in an order that requires the least amount of analysis up front. Subsequent decisions require more analysis but stop short of a full modal force calculation with unsteady CFD. The goal of the proposed decision tree is to provide an effective preliminary assessment of the resonance risk imparted by the impeller-diffuser interaction.

Chapter 6

Conclusion

6.1 Summary

The impeller-diffuser interaction has been shown to generate spatially distributed traveling wave loading on the impeller blades. The generated loading can be a dominant forcing function in a centrifugal compressor stage that may induce HCF problems on the rotating airfoils. The forced response of two splitter blade modes has been computed and shows good agreement with simplified models derived from first principles.

The forced response of continuous systems, such as Bernoulli-Euler beams and taut strings, are studied to determine how the spatial distribution of a loading influences the vibratory response of a natural structural mode of vibration. These models indicate that when the wavenumber of the forcing function is equal to the wavenumber of the mode shape, the forced response is maximized. The matching of wavenumbers physically implies that the phase speed of the forcing function matches the phase speed of the vibratory excitation, provided the forcing frequency and natural frequency are equal. For the research centrifugal compressor stage, the acoustic wavelength and structural vibration mode wavelength are found to be equal at chordwise locations for both splitter modes 5 and 6. Lightprobe data suggests that mode 6 has a stronger response than mode 5 which is consistent with the computed results. Since the characteristic wavelengths of the excitation and mode shape match

for modes 5 and 6, the spatial correlation of the forcing function and mode shape is not the key driving mechanism distinguishing the forced response of mode 5 from mode 6.

Further assessment of the impeller's forced response is performed for splitter blade modes 5 and 6 by computing the displacement amplitude of five models with various boundary and loading conditions. The results from the models are assessed and contrasted to identify the driving physical mechanisms that set the impeller's forced response at resonance. The loading is computed numerically using unsteady CFD and the structural vibratory mode shapes computed from FEM analysis. Geometry variations of the airfoil and backwall thickness, similar to those imposed by manufacturing tolerances, are performed to determine the sensitivity of the forced response. Mode 6 shows high sensitivity to geometry variation while mode 5 does not. The variation in the forced response of mode 6 is found to be a result of the blade-backwall mode coupling which does not exist within the domain of geometry variation assessed for mode 5. The utility of a simplified SAFE diagram is also demonstrated as it effectively shows where modal coupling is likely. Variations in the computed modal force are consistent with the veering points identified on the SAFE diagram. Additionally, a simple two mass-spring system is constructed to replicate the forced response variation seen on the impeller as a result of blade-backwall coupling. The behavior of this model at resonance shows good agreement with the impeller's forced response in the vicinity of a veering point, supporting the hypothesis that this response variation is driven by the coupling of natural modes.

6.2 Conclusions

The findings of this thesis are focused on the physical mechanisms that set the forced response of an impeller blade as a result of the unsteady pressure field generated by the impeller-diffuser interaction. The mechanisms are identified through the use of several computational models that vary the structural boundary conditions and corrected flow conditions. These findings are enumerated below as,

1. Forcing frequency versus natural structural frequency:

   (a) facilitates narrow frequency band energy transfer when the forcing frequency and natural frequency are nearly equal, and

   (b) diminishes response when the forcing frequency is not equal to a natural frequency of the structure.

2. Forcing wavelength versus natural structural wavelength:

   (a) facilitates energy transfer where the spatial distribution of the unsteady loading and mode shape are well correlated, and

   (b) enhances response when the ratio of the forcing wavelength to the structural wavelength is between 0.5 and 1.5.

3. Physical speed of the crossing:

   (a) scales the loading fluctuation with exducer dynamic head for similar corrected conditions, and

   (b) increases the forced response risk of high speed crossings as the modal force scales with the magnitude of the loading fluctuation.

4. Modal displacement at the trailing edge:

   (a) enhances vibratory energy transferred to the structure as the unsteady loading is highest in the vicinity of the trailing edge, and

   (b) indicates potential blade-backwall mode coupling which alters the calculated modal work and forced response amplitude.

5. Blade-backwall mode placement:

   (a) reduces the impact general structural stiffening may have on mitigating the forced response if blade and backwall dominant modes begin to couple, and

   (b) increases sensitivity of the forced response to variations in geometry if blade and backwall dominant modes couple at a known excitation frequency.

6.3 Recommended Future Work

The forced response of the impeller's splitter blade is computed with some basic assumptions. It is recommended that these assumptions be further elaborated upon in future study.

First, the damping acting on the impeller, whether mechanically, aerodynamically, or internally in the material, was not studied in this thesis but has an equally important contribution in setting the overall level of the blade's forced response. The aerodynamic portion of the total damping is one area that should be studied in greater detail as its contribution may be significant during certain operating points as the modal displacement and aerodynamic characteristics of the flow change. Understanding the physical mechanism that set the level of aerodynamic damping would be of great utility as even a "small" amount of modal force can lead to high amplitude resonance if the total damping is driven close to zero.

Secondly, the physical mechanism that sets the blade loading amplitude is not well understood. The amplitude of the loading generated by the impeller-diffuser interaction is a function of the phase lag of the acoustic waves traversing the pressure and suction sides of the impeller blades. The unsteady static pressure amplitude at any location on the blade surface has been shown to be a function of the physical speed, impeller-diffuser gap, diffuser incidence and blade passage relative diffusion; however, the physical mechanisms that set the unsteady pressure difference from the pressure side to the suction side have not been quantified on a parametric basis.

Lastly, for the research centrifugal impeller, the correlation of the forcing function and mode shape alone did not lead to a definitive conclusion of whether splitter mode 5 or 6 would have a higher response. It is recommended that the concept of wavenumber matching at resonance be extended to other centrifugal machines, or other turbomachinery applications, to determine the potential value of this condition in identifying the strength of a resonance early in the design process.

Appendix A

Modeling the Blade-Backwall Interaction

A.1 Simplified Model: Two Mass-Spring System

To further explore the blade-backwall interaction witnessed in Chapter 4 a simple two mass-spring system is assessed. Figure A-1 shows schematically the system considered. The ratio of the two masses in this system are chosen to reflect the relative mass of the blades and disk, which is about 5%. As the system has two masses and motion is only permitted horizontally along the axis of the springs, the system has two degrees of freedom (DOF). As a result, this 2-DOF system has two natural modes of vibration. The relative displacement amplitude of each mass during a forced response is related to the mass and stiffness parameters of the system. The governing differential equation for this 2-DOF system is

$$\boldsymbol{M}\ddot{\vec{x}} + \boldsymbol{C}\dot{\vec{x}} + \boldsymbol{K}\vec{x} = \vec{F} \tag{A.1}$$

where $\vec{x}$ is the horizontal displacement vector in the spatial coordinate x and time t. **M** is the *2-by-2* mass matrix, **C** is the *2-by-2* damping matrix, **K** is the *2-by-2* stiffness matrix, and $\vec{F}$ is the load vector which represents the total sum of the forces in the x-direction acting on the masses. Note the only external load applied to the

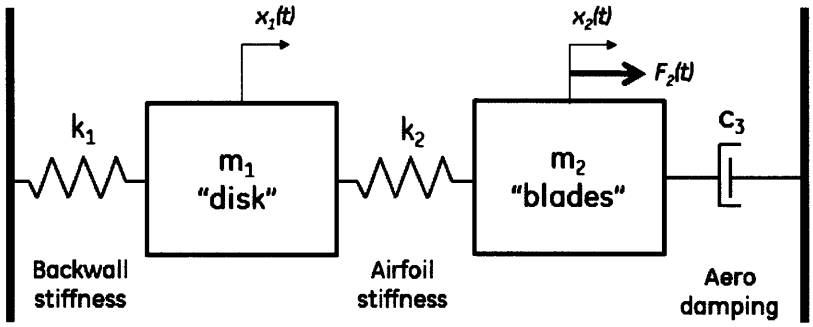

Figure A-1: Two mass-spring system to approximate the blade-disk interaction.

system is a harmonic load, $F_2(t) = F_o sin(\Omega t)$, acting on the blade mass. Summing the forces acting on each mass yields the coupled set of equations describing the dynamic motion of both masses,

$$\begin{bmatrix} m_1 & 0 \\ 0 & m_2 \end{bmatrix} \times \begin{bmatrix} \ddot{x}_1 \\ \ddot{x}_2 \end{bmatrix} + \begin{bmatrix} 0 & 0 \\ 0 & c_3 \end{bmatrix} \times \begin{bmatrix} \dot{x}_1 \\ \dot{x}_2 \end{bmatrix} + \begin{bmatrix} k_1 + k_2 & -k_2 \\ -k_2 & k_2 \end{bmatrix} \times \begin{bmatrix} x_1 \\ x_2 \end{bmatrix} = \begin{bmatrix} 0 \\ F_2(t) \end{bmatrix} \tag{A.2}$$

If the damping is small, the damped and undamped natural frequencies are nearly identical. Ignoring damping and assuming a solution of the form $\vec{x}(t) = \vec{\phi} sin(\omega t)$ to Equation A.2 yields

$$-\omega^2 \boldsymbol{M} \vec{\phi} sin(\omega t) + \boldsymbol{K} \vec{\phi} sin(\omega t) = 0 \tag{A.3}$$

or further simplified yields

$$\boldsymbol{M}^{-1} \boldsymbol{K} \vec{\phi} = \Lambda I \vec{\phi} \tag{A.4}$$

where I is a *2-by-2* identity matrix and Λ is one of two eigenvalues of the 2-DOF system. Λ is related to the natural frequencies of the system by

$$\Lambda = \omega^2 \tag{A.5}$$

The eigenvalues are found from the nontrivial solution of the determinant [5]

$$det(\boldsymbol{M}^{-1}\boldsymbol{K} - \Lambda I) = 0 \tag{A.6}$$

The eigenvectors, $\vec{\phi}$, are solutions which satisfy Equation A.4 for a particular eigenvalue Λ. In the lowest frequency mode (mode 1) the two masses move in phase in the same direction while for mode 2 the masses move in phase in opposite directions. The eigenvectors describe the mode shapes of the vibratory mode while the eigenvalue or eigenfrequency describes the natural frequency. The system also has two characteristic frequencies other than the eigenfrequencies.

The "disk-alone" frequency is,

$$\omega_{Disk-Alone} \approx \sqrt{\frac{k_1}{m_1}} \tag{A.7}$$

The "blade-alone" is similarly,

$$\omega_{Blade-Alone} \approx \sqrt{\frac{k_2}{m_2}} \tag{A.8}$$

The ratio of the two characteristic frequencies is used to explore the interaction of blade dominant and backwall dominant modes of the centrifugal impeller. The ratio of the characteristic frequencies is varied by changing the stiffnesses, k_1 and k_2, of the two springs in the system in a study to reflect the resonant response of the splitter blade due to changes in the backwall and airfoil thickness. The mass of the disk, m_1 and blades, m_2, remains constant as the stiffnesses are varied. The forcing function amplitude is constant with displacement amplitude of the blade, and the forcing frequency is always equal to the blade-alone frequency. The absolute value of the mass and stiffness parameters are not chosen to be representative of impeller; however, the ratios of these parameters are representative of the impeller. It follows that that the absolute value of the computed response amplitude is not as important

as the trends given by the model for variations in stiffness.

A.2 Increasing "Backwall" Stiffness

To elicit a forced response similar to that of the impeller when the backwall thickness is changed, the stiffness of the disk, k_1, is varied. Figure A-2 shows a map of the system's two natural frequencies as a function of the disk-alone to blade-alone frequency ratio. The ratio of these characteristic frequencies changes as the disk-alone frequency increases with increasing k_1. The dashed lines represent the two natural frequencies of the system while the solid lines represent the characteristic frequencies. The veering behavior of the two system frequencies can be clearly seen as the two dashed lines approach and then diverge from one another without crossing at a disk-alone to blade-alone frequency ratio of 1. Note that when the ratio of the characteristic frequencies is well below or above 1, the system frequencies behave like the characteristic frequencies. For example, if the disk is very stiff compared to the blade, the disk-alone to blade-alone frequency will be greater than 1 and the lowest system mode will behave with the blade-alone frequency and the higher system mode will behave with the disk-alone frequency with little motion or influence from the adjacent mass.

As the frequencies of the two characteristic modes approach one another, the forced response of the blade and mass begin to change. Figure A-3 shows the response of the blade and disk as a function of the ratio of disk-alone to blade-alone frequency. When the ratio of characteristic frequencies is nearly 1, the blades experience a drop in response while the disk experiences an increase. Above a ratio of 1 between the characteristic frequencies, the response of the blade and disk nearly level out. Further stiffening of the disk does not improve the forced response of the blade. As a result, stiffening the disk is not an effective means to reduce the forced response of the blade.

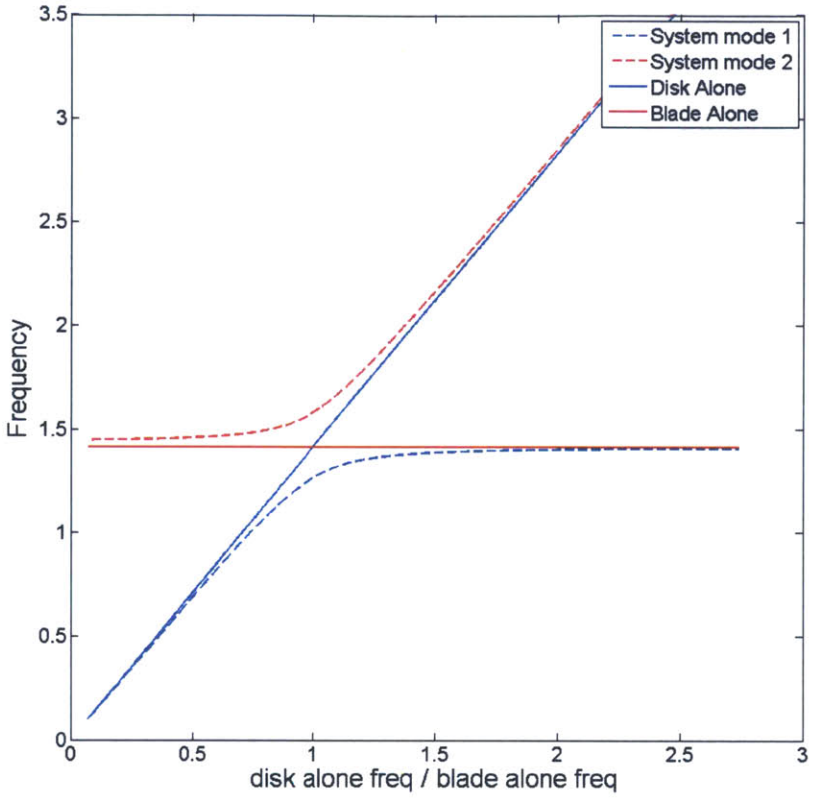

Figure A-2: Two mass-spring eigenfrequencies as a function of k_1, backwall stiffness.

A.3 Increasing "Airfoil" Stiffness

Similar to increasing k_1 to assess the variations in blade response to the backwall thickness, the stiffness k_2 is varied to elicit the forced response of the impeller blades to changes in the airfoil thickness. Figure A-4 shows a map of the system's two natural frequencies as a function of the disk-alone to blade-alone frequency ratio. As the airfoil stiffness, k_2, is increased, the ratio of the characteristic frequencies decreases. The dashed lines represent the two natural frequencies of the system while the solid lines represent the characteristic frequencies. The veering behavior of the two system frequencies is again clearly seen as the two dashed lines approach and then diverge from one another without crossing at a disk-alone to blade-alone frequency of 1. Similar to Figure A-2, when the ratio of the characteristic frequencies is well

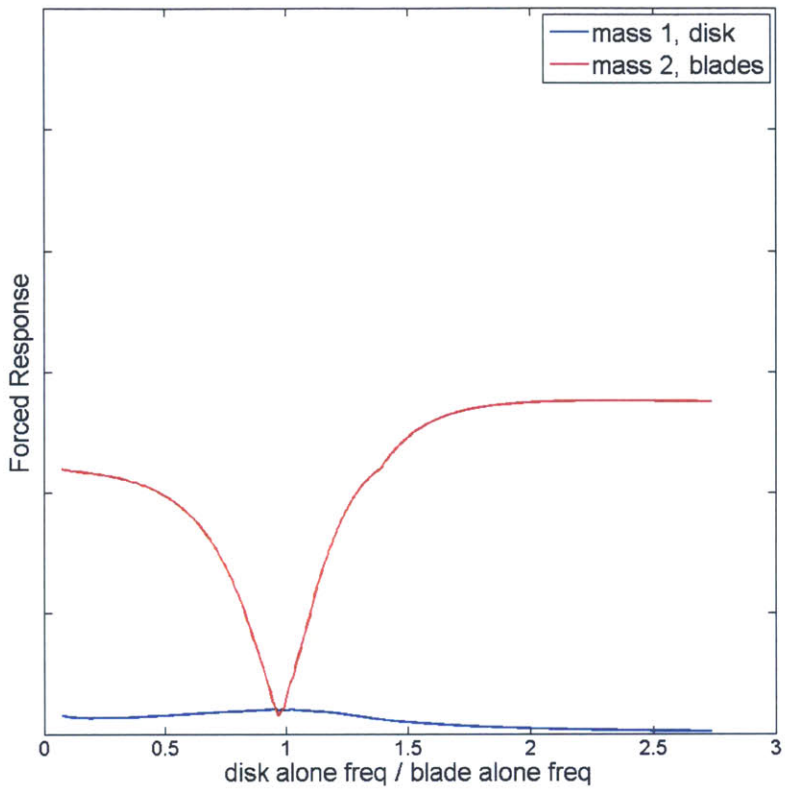

Figure A-3: Two mass-spring response as a function of the characteristic frequency ratio as the disk stiffness, k_1, is varied.

below or above 1, the system frequencies behave like the characteristic frequencies.

Figure A-5 shows the forced response of the blade and disk as a function of the ratio of disk-alone to blade-alone frequency. As the frequencies of the two characteristic modes become close, the forced response of the blade and mass begin to change; however, the response of the blade now appears to have a non-zero slope away from the veering point. The linear slope of the blade's response is in part caused by the increase in the blade-alone frequency (the chosen forcing frequency). Equation 3.1 for a SDOF response shows that the physical displacement is proportional to the reciprocal of the driving frequency squared, which results in a linear increase in response as the ratio of disk-alone to blade-alone frequency increases. Physically, this trend in the forced response with a stiffer (or thicker) blade implies that adding stiffness reduced the

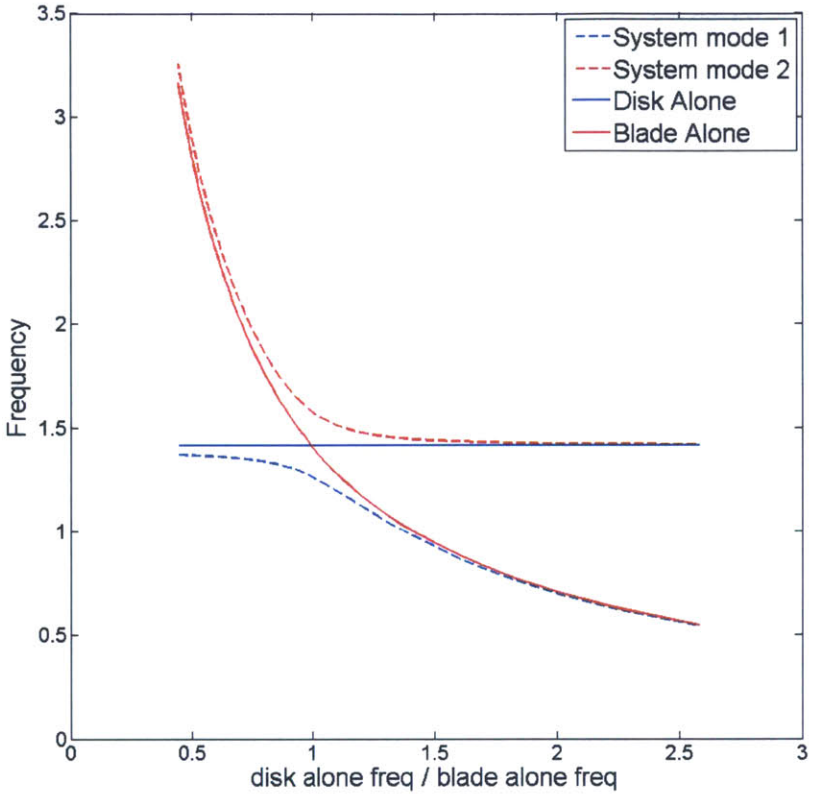

Figure A-4: Two mass-spring eigenfrequencies as a function of k_2, airfoil stiffness.

forced response of the blade. When the ratio of characteristic frequencies is nearly 1, the blades experience a drop in response while the disk experiences an increase. Away from the point of modal coupling, increasing the stiffness of the blades decreases the forced response as expected.

A.4 Modeling Results

The response of the centrifugal blade and the two mass-spring system blade are compared in Figure A-6. The study that involves changing the backwall thickness is shown on the left while the study that involves changing the airfoil thickness is shown on the right. Note the similarity in the response when the disk to airfoil frequency is nearly 1. The behavior of the centrifugal impeller's forced response is similar to

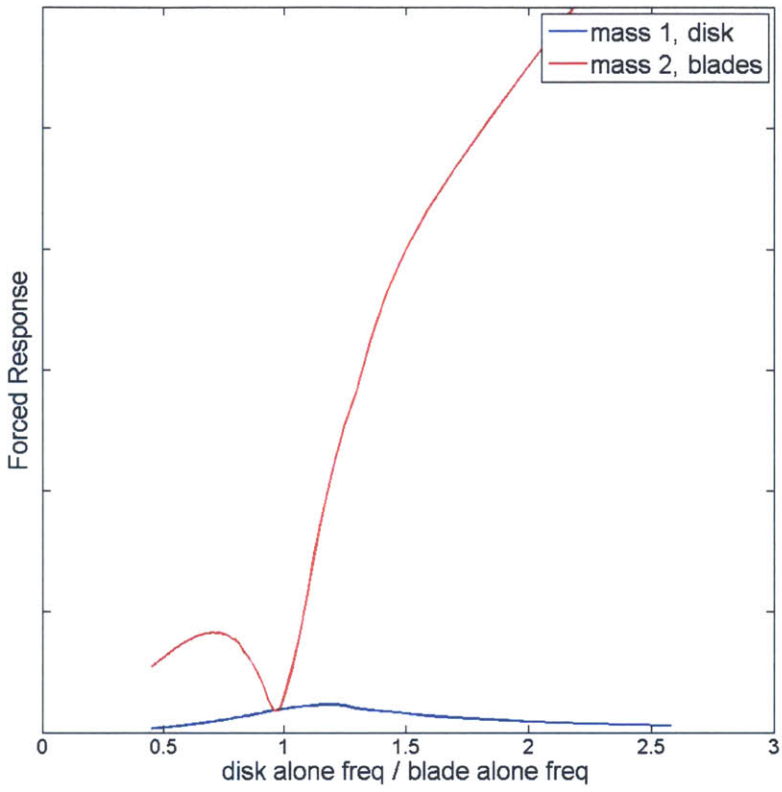

Figure A-5: Two mass-spring response as a function of the characteristic frequency ratio as the airfoil stiffness, k_2, is varied.

that of m_2, the blade mass, in the two mass-spring system. Also, the mode shape magnitude of the impeller and the two mass-spring system blade are both maximized at the veering point where the characteristic frequencies are equal.

For the two mass-spring system, the overall level of variation during the eigenvalue veering is controlled by the strength of the modal coupling. The strength of the modal coupling also sets the attenuation away from unity of the characteristic frequencies. Attempts to quantify the modal coupling in regions of mode veering have been performed by du Bois et al. [3]. Du Bois proposed several parameters that ultimately lead to the calculation of a "veering index" which seeks to quantify the strength of the modal coupling. The veering index is a function of the system's mass and stiffness matrices. Calculations of a veering index for this two mass-spring

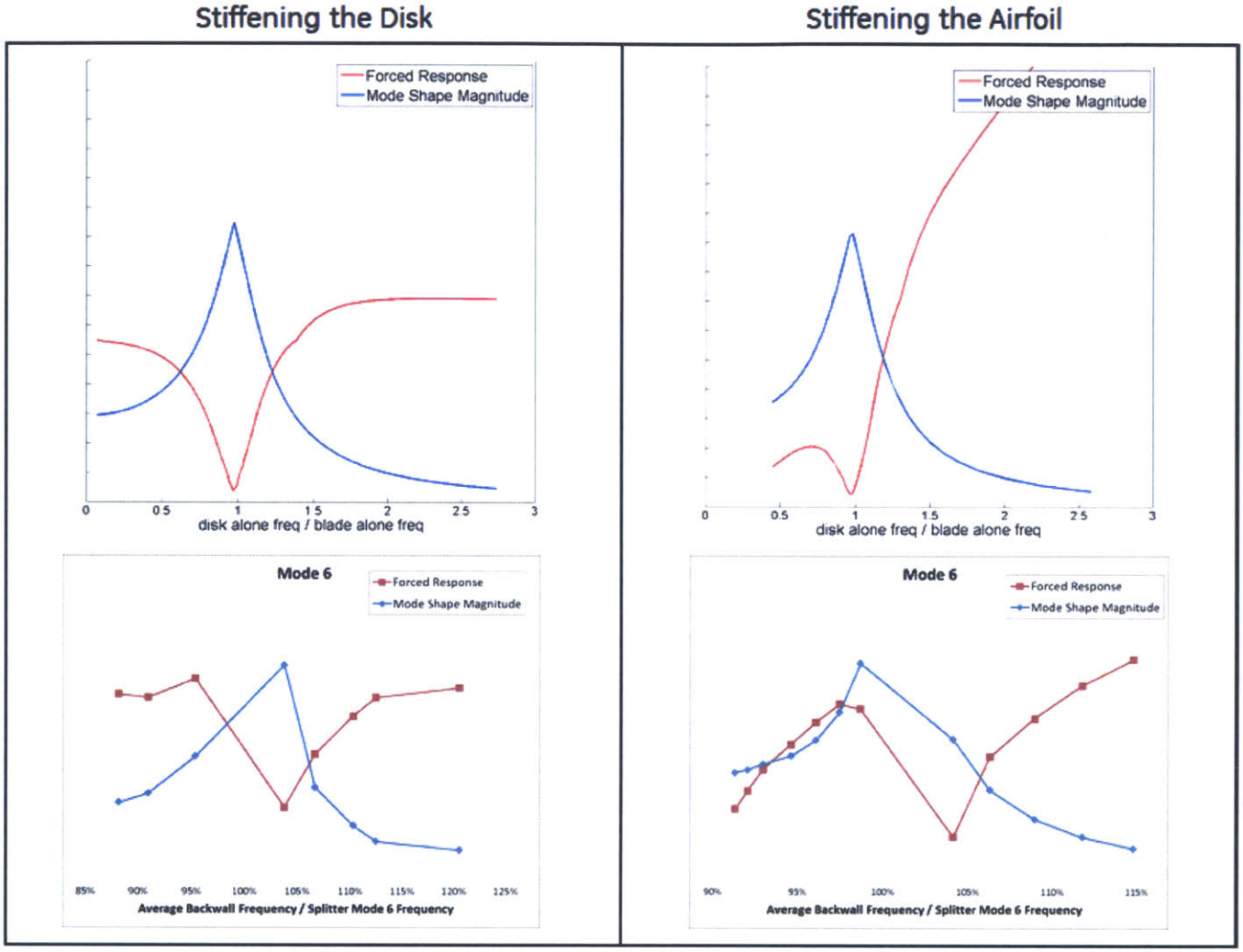

Figure A-6: Comparison of the response between the representative two mass-spring system and the actual centrifugal impeller.

system or impeller are not implemented here.

A.5 Summary

The complicated modal interactions of the airfoil and backwall dominant modes of the centrifugal impeller are modeled with a two mass-spring system. The forced response of this simplified system shows good agreement with the forced response of the centrifugal impeller splitter blade. Both systems exhibit a strong variation in

the forced response in the vicinity of modal coupling. The similarity of the forced responses of these two systems supports the hypothesis that the variation in modal force seen on the impeller is driven by the blade-backwall mode interaction.

Bibliography

[1] Jan Bladh. *Efficient Predictions of the vibratory response of mistuned bladed disks by reduced order modeling.* PhD thesis, University of Michigan, 2001.

[2] Robert D. Blevins. *Formulas for Natural Frequency and Mode Shape.* Krieger Publishing Company, Malabar, FL, 1979.

[3] J. L. du Bois et al. Localization and curve veering: A different perspective on modal interactions. Society for Experimental Mechanics, 2009.

[4] John Dugundji. Simple expressions for higher vibration modes of uniform Euler beams. *AIAA Journal*, 26(8), 1988.

[5] Blanchard et al. *Differential Equations, 2nd Edition.* Brooks/Cole, Pacific Grove, CA, 2002.

[6] Singh et al. Safe diagram - a design and reliability tool for turbine blading. In Jean C. Bailey, editor, *Proceedings of the Seventeenth Turbomachinery Symposium*, Dallas, Texas, 1988. Texas A and M University Press.

[7] Ziegler et al. A study on impeller-diffuser interaction: Part I-influence on the performance. ASME, June 2002.

[8] Ronald D. Flack. *Fundamentals of Jet Propulsion with Applications.* Cambridge University Press, New York, 2005.

[9] Kenneth Gould. Characterization of unsteady flow processes in a centrifugal compressor stage. Master's thesis, Massachusetts Institute of Technology, 2006.

[10] Daniel J. Inman. *Engineering Vibration.* Prentice Hall, New Jersey, 1994.

[11] Albert Kammerer. Experimental study of impeller blade vibration during resonance - Part II: Blade damping. *Journal of Engineering for Gas Turbines and Power*, 131(022509-1), 2009.

[12] Eduardo Kausel. *Advanced Structural Dynamics.* Massachusetts Institute of Technology, Cambridge, MA, 2009.

[13] A. W. Leissa. Closed form exact solutions for the steady state vibration of continuous systems subjected to distributed exciting forces. *Journal of Sound and Vibration*, 1989.

[14] Christopher Lusardi. Characterization of unsteady loading due to impeller-diffuser interaction in centrifugal compressors. Master's thesis, Massachusetts Institute of Technology, 2012.

[15] C. Pierre. Mode localization and eigenvalue loci veering phenomena in disorder structures. *Journal of Sound and Vibration*, 126(3)(485-502), 1988.

[16] Singiresu Rao. *Vibrations of Continuous Systems.* John Wiley and Sons, Inc., Hoboken, NJ, 2007.

[17] ANSYS Academic Research. *Help System, 5.3. Solving a Cyclic Symmetry Analysis.* ANSYS, Inc., release 14.0 edition.

[18] Caitlin Smythe. Forced response predictions in modern centrifugal compressor design. Master's thesis, Massachusetts Institute of Technology, 2005.

[19] Snyder and Burns. *Forced Vibration and Flutter Design Methodology.* AGARD Manual on Aeroelasticity in Axial-Flow Turbomachines, NATO, 1985.

[20] Alfanso Villanueva. Characterization of the flow field response to vaneless space reduction in centrifugal compressors. Master's thesis, Massachusetts Institute of Technology, 2006.

[21] Robert Walter. Provision and discussion of impeller FEM model. personal communication, 2011.

[22] Qian Wang. *A Practical Method to Identify the Potential Resonance of Centrifugal Compressor Impellers.* Conference: IMAC XVII - 17th International Modal Analysis Conference, Cambridge, Mass., 1999.